

# UC Santa Barbara

## UC Santa Barbara Electronic Theses and Dissertations

### Title

Design and Fabrication of Sub-100nm Base-Emitter Junctions of THz InP DHBTs

### Permalink

<https://escholarship.org/uc/item/2fx4h8jc>

### Author

Chiang, Han-Wei

### Publication Date

2014

Peer reviewed|Thesis/dissertation

UNIVERSITY of CALIFORNIA  
Santa Barbara

**Design and Fabrication of Sub-100 nm  
Base-Emitter Junctions of THz InP DHBTs**

A Dissertation submitted in partial satisfaction  
of the requirements for the degree

Doctor of Philosophy  
in  
Electrical and Computer Engineering

by

Han-Wei Chiang

Committee in Charge:

Professor Mark J. W. Rodwell, Chair  
Professor John E. Bowers  
Professor Umesh K. Mishra  
Professor Robert A. York

December 2014

The Dissertation of Han-Wei Chiang is approved.

---

Professor John E. Bowers

---

Professor Umesh K. Mishra

---

Professor Robert A. York

---

Professor Mark J. W. Rodwell, Committee Chair

October 2014

Design and Fabrication of Sub-100 nm Base-Emitter Junctions of THz InP  
DHBTs

Copyright © 2014

by

Han-Wei Chiang



*Dedicated to my parents  
for their love and support.*

謹獻給  
我的父母

## Acknowledgements

It has been five amazing years since I joined Professor Rodwell's research group at UCSB. I can still vaguely recall the very first day I arrived at Los Angeles International Airport, where the adventure to doctorate degree began. Now, as I am moving towards the end of the expedition, I would like to express my gratitude to everyone who has helped me in this fantastic journey.

Trained as a Materials scientist during my undergraduate program, I decided to take the career path into the semiconductor industry. I am very grateful to my advisor, Prof. Mark Rodwell, for granting me the opportunity to join his research group and participate the development of the state-of-the-art DHBTs. I am very thankful for the valuable discussions with Prof. Rodwell, which have broadened my insight on Device Physics and Microwave Circuits. With his guidance, I have not only survived the transition from Materials Science to Electrical Engineering, but, more importantly, influenced by his way of thinking, in which everything must follow a logical path. I believe the latter is the essence in the training of a Ph. D. regardless the field.

I would also like to thank my committee members: Prof. Umesh Mishra, Prof. John Bowers, and Prof. Robert York. It is through Prof. Mishra's lectures as well as our discussions that I acquire the fundamental knowledge on electronic devices. Even now, several years after taking his class, I am still impressed by the depth of his knowledge. The discussion with Prof. Bowers and Prof. York have also been proven to be very worthwhile. Their inputs during my qualifying exam have partially motivated the effort in TCAD simulation in this thesis.

I intend to give my gratitude towards Dr. Brian Thibeault, who have shared

with me his experience and brilliant insight on III-V processing. Because of his input, I have been able to develop/refine new process flow more efficiently. Dr. William Mitchell is the expert on e-beam lithography. Without his effort, the fabrication of nano-scaled device would not be possible. In addition, the accomplishments reported in this dissertation would not be realized if there had not been a fabrication facility managed by a dedicated staff.

The HBT team in Rodwell group deserves my sincere acknowledgement. I am grateful towards Dr. Vibhor Jain and Dr. Evan Lobissor, who taught me in detail the entire DHBT process flow. I owe my colleague Johann Rode many thanks for his credit in developing the base contact process flow and for his help in both processing and measurement. I have enjoyed the time working with Prateek Choudhary, who always cheered me up after numerous failure in the cleanroom. Through my interaction with both former and current Rodwell group members: Andy, Ashish, Cheng-Ying, Doron, Eli, Greg, Hyunchul Kim, Hyunchul Park, Jeremy, Rob, Saeid, Sanghoon, Seong-Kyun, and Thomas, I have learned a lot, be it the professional knowledge or the philosophy in life.

It has been a long way to Ph.D., and I could not have made it to the very end if without the support from all my friends in Santa Barbara and in Taiwan. I will cherish every moment I shared with you.

Finally, my utmost gratitude shall belong to my family, especially my parents, who encouraged me to study abroad. None of these would be possible if it were not for the unconditional love and support of my family.

# Curriculum Vitæ

## Han-Wei Chiang

### Personal

Jan. 1985                      Born in Taipei, Taiwan.

### Education

2014                      Ph.D. in Electrical and Computer Engineering, University of California, Santa Barbara.

2011                      M.S. in Electrical and Computer Engineering, University of California, Santa Barbara .

2007                      B.S. in Materials Science and Engineering, National Taiwan University.

### Publications

- [1] **H. W. Chiang**, J. C. Rode, P. Choudhary, and M. J. W. Rodwell, “*Interfacial transport and current gain in InGaAs/InP DHBTs for THz applications*,” 72nd IEEE Device Research Conference, 2014.
- [2] **H. W. Chiang**, J. C. Rode, P. Choudhary, and M. J. W. Rodwell, “*Lateral Carrier Diffusion and Current Gain in THz InGaAs/InP DHBTs*,” J. Appl. Phys., vol. 115, no. 3, pp. 034513, 2014.
- [3] D. C. Elias, A. Sivananthan, C. Zhang, S. Keller, **H. W. Chiang**, J. J. M. Law, B. J. Thibeault, W. J. Mitchell, S. Lee, A. D. Carter, C.-Y. Huang, V. Chobpattana, S. Stemmer, S. P. Denbaars, L. A. Coldren and M. J. W. Rodwell, “*Formation of InGaAs fins by atomic layer epitaxy on InP sidewalls*,” Jpn. J. Appl. Phys., vol. 53, no. 6, pp. 065503, 2014.
- [4] D. C. Elias, J. J. M. Law, **H. W. Chiang**, A. Sivananthan, C. Zhang, B. J. Thibeault, W. J. Mitchell, S. Lee, A. D. Carter, C.-Y. Huang, V. Chobpattana, S. Stemmer, S. Keller, and M. J. W. Rodwell, “*Formation of Sub-10 nm width InGaAs finFETs of 200 nm Height by Atomic Layer Epitaxy*,” 71st IEEE Device Research Conference, 2013.
- [5] M. J. W. Rodwell, M. Seo, J. Hacker, A. Young, Z. Griffith, R. Pierson, M. Urteaga, J. C. Rode, **H. W. Chiang**, V. Jain, E. Lobisser, T. Reed, A. Baraskar, J. J. M. Law, A. D. Carter, S. Lee, D. C. Elias, B. J. Thibeault, W. J. Mitchell, S. Stemmer, A. C. Gossard, S. Mehotra, M. Povolotskyi, G. Klimeck, “*Transistor and IC design for Sub-mm-wave and THz ICs*,” 2012 European Microwave IC Conference, 2012.

- [6] M. J. W. Rodwell, J. C. Rode, **H. W. Chiang**, P. Choudhary, T. Reed, E. Bloch, S. Danesgar, H-C Park, A. C. Gossard, B. J. Thibeault, W. J. Mitchell, M. Urteaga, Z. Griffith, J. Hacker, M. Seo, B. Brar, “*THz Indium Phosphide Bipolar Transistor Technology*,” 2012 IEEE Compound Semiconductor Integrated Circuit Symposium, 2012.
- [7] E. Lobisser, J. C. Rode, V. Jain, **H. W. Chiang**, A. Baraskar, W. J. Mitchell, B. J. Thibeault, Mark J. W. Rodwell, “*InGaAs/InP DHBTs with Emitter and Base Defined through Electron-Beam Lithography for Reduced Ccb and Increased RF Cut-off Frequency*,” 39th International Symposium on Compound Semiconductors, 2012.
- [8] V. Jain, J. C. Rode, **H. W. Chiang**, A. Baraskar, E. Lobisser, B. J. Thibeault, M. J. W. Rodwell, M. Urteaga, D. Loubychev, A. Snyder, Y. Wu, J. M. Fastenau, W. K. Liu, “*1.0 THz  $f_{\max}$  InP DHBTs in a refractory emitter and self-aligned base process for reduced base access resistance*,” 69th IEEE Device Research Conference, 2011.

## Abstract

Design and Fabrication of Sub-100 nm Base-Emitter Junctions of THz InP  
DHBTs

by

Han-Wei Chiang

Because of their wide RF bandwidth ( $\sim 1$  THz) and high breakdown voltages ( $BV_{CEO} > 3$  V), npn-In<sub>0.53</sub>Ga<sub>0.47</sub>As/InP double heterojunction bipolar transistors (DHBTs) have extensive applications in monolithic microwave integrated circuits (MMICs) such as high performance transceivers, near-terabit optical fiber link, and THz amplifiers in radar/imaging systems. The improvements in the performance of DHBTs were made possible because of device scaling. As the technology advances towards the next scaling generations, new challenges in the manufacturing techniques and the device designs are met. The purpose of this work is to provide solutions to the problems encountered in the fabrication and design of the base-emitter junction while scaling from 200 to sub-100 nm emitter width.

Two important issues regarding the base-emitter junction arises while scaling towards sub-100 nm emitter width. The process flow for the refractory emitter metal stack developed for 250-100 nm emitter width has already reached its limitation. In order to improve the transistor yield at a reduced linewidth without designing a new process flow, revisions have been made to the existing one. Employing the revised process flow, 75 nm-wide emitter is feasible. The overall transistor yield has also been improved. This increases the number of working

devices per sample, enabling thorough device analyses.

Experimentally, a reduction of current gain ( $\beta$ ) associated with device scaling has been observed. In order to assess the causes of the reduction, the electron transport in the base is emulated by a commercial simulator. A model for DC- $\beta$  at high injection current density ( $25 \text{ mA}/\mu\text{m}^2$ ) was constructed by the comparison between the experimental and the simulation results. The model allows the estimation of  $\beta$ , which benefits the design of the future scaling generations of DHBTs.

It has been deduced from the model that the current originated from Auger recombination and lateral electron diffusion (via the surface and the bulk base semiconductor) are the dominant components that limit DC- $\beta$ . To suppress the diffusion current via surface, a process flow is developed to form passivating sidewall onto the base surface. Such process flow has already been incorporated into DHBT fabrication. Moreover, new geometries for the base-emitter junction have been designed on the purpose of reducing the Auger recombination rate and lateral electron diffusion in the bulk base region. According to the simulation results, the new designs could potentially improve DC- $\beta$  beyond 50 if the corresponding process flow could be adequately integrated.

# Contents

<b>Acknowledgements</b>	<b>v</b>
<b>Curriculum Vitæ</b>	<b>vii</b>
.....	vii
<b>Abstract</b>	<b>ix</b>
<b>List of Tables</b>	<b>xiv</b>
<b>List of Figures</b>	<b>xv</b>
<b>1 Introduction</b>	<b>1</b>
References .....	6
<b>2 DHBT Theory</b>	<b>10</b>
2.1 Device Structure .....	11
2.2 RF Characteristics and DHBT Scaling Laws .....	14
2.2.1 Small-signal AC Equivalent Circuit .....	14
2.2.2 Base and Collector Transit Time .....	15
2.2.3 Emitter Charging Time .....	18
2.2.4 Collector Charging Time .....	19
2.2.5 Cutoff Frequencies .....	21
2.2.6 DHBT Scaling Law .....	24
2.3 DC Current Gain of DHBT .....	25
2.3.1 Bulk Base Current .....	28
2.3.2 Bulk Lateral Diffusion Current .....	33
2.3.3 Surface Recombination and Conduction Current .....	34
2.3.4 DC Current Gain and DHBT Scaling .....	36
References .....	38



<b>3</b>	<b>DHBT Process Improvement</b>	<b>42</b>
3.1	Refractory Emitter Metal Stack . . . . .	44
3.2	Composite Dielectric Sidewall . . . . .	52
3.3	Interconnects Between Metal Layers . . . . .	56
	References . . . . .	61
<b>4</b>	<b>Experimental Results</b>	<b>63</b>
4.1	Measurement set up and calibration . . . . .	64
4.2	DHBT63B . . . . .	67
4.2.1	Device structure and process feature . . . . .	67
4.2.2	TEM analysis . . . . .	71
4.2.3	TLM results . . . . .	73
4.2.4	Transistor DC characteristics . . . . .	75
4.2.5	RF performance . . . . .	77
4.3	DHBT58H . . . . .	87
4.3.1	Device structure and process feature . . . . .	87
4.3.2	TEM analysis . . . . .	90
4.3.3	TLM results . . . . .	91
4.3.4	Transistor DC characteristics . . . . .	92
4.3.5	RF performance . . . . .	94
4.4	Summary . . . . .	102
	References . . . . .	104
<b>5</b>	<b>DC Current Gain of DHBTs: TCAD Simulation</b>	<b>106</b>
5.1	Simulation Setup . . . . .	108
5.1.1	Carrier Mobility and Velocity Saturation . . . . .	110
5.1.2	Band Structure . . . . .	111
5.1.3	Carrier Recombination . . . . .	113
5.1.4	Surface Conduction and Recombination . . . . .	115
5.2	Simulation and Experimental Results . . . . .	117
5.2.1	Bulk Recombination and Lateral Diffusion Current . . . . .	117
5.2.2	Surface Recombination and Conduction Current . . . . .	121
5.2.3	Model Verification . . . . .	125
5.3	Novel Base-Emitter Junction Designs . . . . .	128
5.3.1	Epitaxy Design: Graded Base with a Pulse-doped Layer . . . . .	129
5.3.2	Supplement Process Flow: Trench in Extrinsic Base . . . . .	131
5.3.3	New Process Flow: Recessed B-E Junction and Emitter Re-growth . . . . .	133
	References . . . . .	136

<b>6</b>	<b>Conclusion</b>	<b>140</b>
6.1	Achievements . . . . .	141
6.1.1	Process Improvements . . . . .	141
6.1.2	Device Performance . . . . .	142
6.1.3	Simulation Results . . . . .	143
6.2	Future Work . . . . .	144
6.2.1	Refractory Base Contact . . . . .	144
6.2.2	Extrinsic Base Passivation . . . . .	144
6.2.3	Emitter Width Scaling and Emitter Regrowth . . . . .	145
	References . . . . .	147
<b>A</b>	<b>DHBT Process Flow</b>	<b>149</b>
A.1	Overview . . . . .	151
A.2	Emitter Process Flow . . . . .	151
A.2.1	Emitter Contact and Composite Metal Stack . . . . .	151
A.2.2	Sacrificial Dielectric Layer and Chromium Mask Deposition	153
A.2.3	Emitter Lithography . . . . .	153
A.2.4	Chromium Mask Dry Etch . . . . .	154
A.2.5	Emitter Composite Stack Dry Etch . . . . .	154
A.2.6	First SiN <sub>x</sub> Sidewall Formation . . . . .	155
A.2.7	InGaAs Emitter Cap Wet Etch . . . . .	156
A.2.8	Chromium Mask Removal . . . . .	156
A.2.9	Second SiN <sub>x</sub> Sidewall Formation . . . . .	157
A.2.10	InP Emitter Wet Etch (LO) . . . . .	157
A.2.11	Base Contact Lithography and Lift-off(LO) . . . . .	157
A.2.12	Third Sidewall Formation (LO/RB) . . . . .	158
A.2.13	Base Post Lithography and Lift-off (LO/RB) . . . . .	159
A.2.14	Base-collector Mesa Lithography (LO/RB) . . . . .	160
A.2.15	InP Emitter Wet Etch (RB) . . . . .	160
A.2.16	First Base Metalization (RB) . . . . .	161
A.2.17	Second Base Metal Lithography and Lift-off (RB) . . . . .	161
A.2.18	Refractory Metal Dry Etch (RB) . . . . .	162
A.2.19	Base-collector Mesa Wet Etch . . . . .	162
A.2.20	Collector Contact Lithography and Lift-off . . . . .	163
A.2.21	Device Isolation Lithography and Wet Etch . . . . .	164
A.2.22	Collector Post Lithography and Lift-off . . . . .	165
A.2.23	SiN <sub>x</sub> Anchor Layer Deposition . . . . .	166
A.2.24	BCB Planarization . . . . .	167
A.2.25	Dielectric Contact Via . . . . .	168
A.2.26	Metal 1 Lithography and Lift-off . . . . .	169

# List of Tables

2.1	Scaling laws of DHBTs: the required change for improving $f_\tau$ and $f_{\max}$ by a factor of $\gamma$ . . . . .	26
4.1	Epitaxial structure of DHBT63. . . . .	69
4.2	Parameters assumed in the cut-off frequencies calculation of DHBT63. . . . .	78
4.3	Epitaxial structure of DHBT58. . . . .	88
4.4	Parameters assumed in the cut-off frequencies calculation of DHBT63. . . . .	95
5.1	In <sub>0.53</sub> Ga <sub>0.47</sub> As parameter values used in simulation and corresponding references. The coefficients for Auger recombination are usually reported as a combined value. . . . .	116
6.1	A summary of device performance of DHBT63B and DHBT58H. . . . .	143
A.1	List of tools involved in DHBT fabrication. . . . .	150

# List of Figures

2.1	The structure of mesa-DHBTs. (a) The cross-section of a DHBT. (b) The top-down view of a DHBT. (c) The schematic showing the important dimensions in DHBTs. Only half of the device is shown due to symmetry. (d) The SEM of a experimental device after the front end process. . . . .	13
2.2	The small-signal equivalent circuit of a DHBT approximated by the hybrid- $\pi$ model. . . . .	15
2.3	The band diagram of a DHBT in the forward active mode. The band gap narrowing effect and the space charge region in the collector are neglected. . . . .	16
2.4	Experimental $C_{CB}$ vs. $J_E$ measured from a device with $W_E=210$ nm and $T_C=100$ nm (DHBT58H). . . . .	21
2.5	The schematic of the distributed R-C network in the base-collector mesa in a DHBT. . . . .	23
2.6	Inverse DC current gain ( $1/\beta$ ) vs. HBT emitter periphery to area ratio ( $P_{je}/A_{je} \approx 2/W_E$ ) of experimental DHBTs with distance between base and emitter contacts ( $W_{gap} \approx 10$ nm and different base designs. The values of $\beta$ are measured at emitter current density $J_E \approx 25\text{mA}/\mu\text{m}^2$ . . . . .	27
2.7	A schematic of the current components in the base of DHBTs. . .	28
2.8	Simulated conduction band energy ( $E_C$ ) at $V_{BE} \approx 1.2$ V vs. depth into the base semiconductor at the edge of the emitter and in the extrinsic base. The simulation assumes a 20 nm thick base with doping varying from $1.2 \times 10^{20} \text{cm}^{-3}$ at the emitter side to $8 \times 10^{19} \text{cm}^{-3}$ at the collector side [18]. The energy is relative to the base Fermi level. . . . .	29

2.9	Three Auger processes in III-V semiconductors. [20]. The solid circles represent the occupied states, and the empty circles represent the empty states. . . . .	30
2.10	Computed electron lifetimes (Auger, SRH, radiative, and total) vs. the depth into the base of a DHBT. A 20 nm thick base with doping varying from $1.2 \times 10^{20} \text{ cm}^{-3}$ at the emitter side to $8 \times 10^{19} \text{ cm}^{-3}$ at the collector side was assumed. The emitter current density is assumed to be $27 \text{ mA}/\mu\text{m}^2$ . . . . .	33
3.1	The schematics of UCSB DHBT emitter process flow. . . . .	47
3.2	The schematics of UCSB DHBT emitter process flow (continued). . . . .	48
3.3	The schematics of the self-aligned base contact lift-off process. . . . .	49
3.4	The schematics of a base contact lifted-off on a tapered emitter stack. A shunt path between the base and the emitter is formed and the extrinsic base is sealed by the base metal and the dielectric sidewall. . . . .	50
3.5	SEM of 1:1 W:TiW metal stack on an InP test sample after $\text{SF}_6/\text{Ar}$ ICP etch. (a) Cross-section of the stack with $W_E \approx 250 \text{ nm}$ . (b) A stack with $W_E \approx 75 \text{ nm}$ . . . . .	52
3.6	Schematics of 256, 128, and 64 nm wide emitter metal stacks after $\text{SF}_6/\text{Ar}$ ICP etch. Upper row: 1:1 W:TiW. Bottom row: 1:2.5 W:TiW. . . . .	53
3.7	SEM cross-sections of 1:2.5 W:TiW metal stack on an InP test sample after recalibrated $\text{SF}_6/\text{Ar}$ ICP etch. (a) $W_E=128 \text{ nm}$ . (b) $W_E=64 \text{ nm}$ . . . . .	54
3.8	Process flow for the composite $\text{Al}_2\text{O}_3/\text{SiN}_x$ sidewall. . . . .	55
3.9	(a) SEM cross-section of a InP test sample with the composite sidewall around the emitter stack and the base contact. The bilayer base metal process was also being tested on the sample. (b) TEM cross-section of a experimental device with a composite sidewall sealing the extrinsic base region. . . . .	56
3.10	Process flow for interconnects between metal layers. . . . .	59
3.11	SEM of interconnects between metal layers on a test sample. . . . .	60
4.1	Top-down schematics of (a) open and (b) short calibration structures, and (c) CPW interconnect with device under test (DUT). . . . .	65
4.2	RF measurement set up. The delay associated with semi-rigid waveguides were removed after calibration. Hence the waveguides are neglected in the diagram. . . . .	68

4.3	Computed band diagram of DHBT63 under $V_{BE}=1.2$ V and $V_{CB}=0.6$ V. The solid lines are the conduction and valance bands when $J_C = 0$ mA/ $\mu\text{m}^2$ , i.e. ignoring the space charge in the collector region. The dashed line represent the conduction and valance bands considering the space charge region in the collector at $J_C \approx 31$ mA/ $\mu\text{m}^2$ .	69
4.4	An SEM image of an HBT sample after base post lift-off. Residues of UV-6 were found around the base contact, possibly due to the damaged resist sidewall. . . . .	70
4.5	TEM cross-section normal to the emitter stripe of a device on DHBT63B with $W_{E,\text{design}}=100$ nm, $W_{BM,\text{design}}=500$ nm. (a) An overview of the device. (b) zoomed in at the vicinity of the base contact and emitter. . . . .	72
4.6	TEM cross-section parallel to the emitter stripe of a device on DHBT63B with $L_{E,\text{design}}=3$ $\mu\text{m}$ . The image is zoomed in at the vicinity of the base post. . . . .	73
4.7	(a) Pinched and (b) Unpinched base TLM data of DHBT63B. The width of TLM structure and the distances between metal pads (gap spacing) were measured with SEM. . . . .	74
4.8	Collector TLM result of DHBT63B. The width of TLM structure and the distances between metal pads (gap spacing) were measured with SEM. . . . .	74
4.9	DC characteristics of the device with $W_{E,\text{design}}=100$ nm, $W_{BM,\text{design}}=500$ nm, and $L_{E,\text{design}}=3$ $\mu\text{m}$ .(a) Common emitter output characteristics. The increment of the base current ( $I_{B,\text{step}}$ ) is 20 $\mu\text{A}$ . (b) I-V characteristics of B-E and B-C diodes (Gummel plot). . . . .	76
4.10	Inverse DC- $\beta$ vs. base-emitter junction periphery to area ratio ( $P_{je}/A_{je}$ ) of the devices on DHBT63B. . . . .	77
4.11	Peak $f_\tau$ and $f_{\text{max}}$ vs. base-emitter junction width of the devices with emitter length ( $L_E$ ) of 2.7 and 3.7 $\mu\text{m}$ on DHBT63B. . . . .	78
4.12	RF measurement results of a device DHBT63B with $W_{E,\text{design}}=150$ nm, $W_{BM,\text{design}}=750$ nm, and $L_{E,\text{design}}=3$ $\mu\text{m}$ : (a) unilateral Mason's gain and $H_{21}$ vs. frequency, (b) Two-port S-parameters vs. frequency, and (c) small-signal equivalent circuit. In both (a) and (b), the solid lines represent the experimental data, and the dashed lines are the ADS simulation results. . . . .	80
4.13	Current dependency of $C_{CB}$ and cut-off frequencies extracted from the device on DHBT63B with $W_{E,\text{design}}=150$ nm, $W_{BM,\text{design}}=750$ nm, and $L_{E,\text{design}}=3$ $\mu\text{m}$ at $V_{CE}=1.2, 1.4,$ and $1.5$ V.(a) $C_{CB}$ vs. $J_E$ . (b) $f_\tau$ and $f_{\text{max}}$ vs. $J_E$ . . . . .	81

4.14	RF measurement results of a device on DHBT63B with $W_{E,\text{design}} = 100 \text{ nm}$ , $W_{\text{BM},\text{design}} = 500 \text{ nm}$ , and $L_{E,\text{design}} = 3 \mu\text{m}$ : (a) unilateral Mason's gain and $H_{21}$ vs. frequency, (b) Two-port S-parameters vs. frequency, and (c) small-signal equivalent circuit. In both (a) and (b), the solid lines represent the experimental data, and the dashed lines are the ADS simulation results. . . . .	83
4.15	Current dependency of $C_{\text{CB}}$ and cut-off frequencies extracted from the device on DHBT63B with $W_{E,\text{design}} = 100 \text{ nm}$ , $W_{\text{BM},\text{design}} = 500 \text{ nm}$ , and $L_{E,\text{design}} = 3 \mu\text{m}$ at $V_{\text{CB}} = 0.2, 0.4, \text{ and } 0.6 \text{ V}$ . (a) $C_{\text{CB}}$ vs. $J_{\text{E}}$ . (b) $f_{\tau}$ and $f_{\text{max}}$ vs. $J_{\text{E}}$ . . . . .	84
4.16	Dimension dependence of (a) $C_{\text{CB}}$ (vs. $W_{\text{BM},\text{design}}$ ) and (b) $R_{\text{B,cont.}}$ (vs. $W_{\text{B,cont.}}$ ) from device with $L_{\text{E}} = 2.7$ and $3.7 \mu\text{m}$ biased at $V_{\text{CB}} = 0.5 \sim 0.6 \text{ V}$ and $J_{\text{E}} = 25 \sim 30 \text{ mA}/\mu\text{m}^2$ . . . . .	85
4.17	Computed band diagram of DHBT58 under $V_{\text{BE}} = 1.2 \text{ V}$ and $V_{\text{CB}} = 0.6 \text{ V}$ . The solid lines are the conduction and valance bands when $J_{\text{C}} = 0 \text{ mA}/\mu\text{m}^2$ . The dashed line represent the conduction and valance bands considering the space charge region in the collector at $J_{\text{C}} \approx 25 \text{ mA}/\mu\text{m}^2$ . . . . .	89
4.18	TEM cross-section normal to the emitter stripe of a device on DHBT58H with $W_{E,\text{design}} = 100 \text{ nm}$ , $W_{\text{BM},\text{design}} = 450 \text{ nm}$ . (a) An overview of the device. (b) zoomed in at the vicinity of the base contact and emitter. . . . .	91
4.19	(a) Pinched base TLM and (b) Collector TLM data of DHBT58H. The width of TLM structure and the distances between metal pads (gap spacing) were measured with SEM. . . . .	92
4.20	DC characteristics of the device with $W_{E,\text{design}} = 100 \text{ nm}$ , $W_{\text{BM},\text{design}} = 600 \text{ nm}$ , and $L_{E,\text{design}} = 3 \mu\text{m}$ . (a) Common emitter output characteristics. The increment of the base current ( $I_{\text{B,step}}$ ) is $24 \mu\text{A}$ . (b) I-V characteristics of B-E and B-C diodes (Gummel plot). . . . .	93
4.21	Inverse DC- $\beta$ vs. base-emitter junction periphery to area ratio ( $P_{\text{je}}/A_{\text{je}}$ ) of the devices on DHBT58H. . . . .	94
4.22	Peak $f_{\tau}$ and $f_{\text{max}}$ vs. base-emitter junction width of the devices with emitter length, $L_{\text{E}} = 2.7 \mu\text{m}$ on DHBT58H. . . . .	95
4.23	RF measurement results of a device on DHBT58H with $W_{E,\text{design}} = 200 \text{ nm}$ , $W_{\text{BM},\text{design}} = 700 \text{ nm}$ , and $L_{E,\text{design}} = 3 \mu\text{m}$ : (a) unilateral Mason's gain and $H_{21}$ vs. frequency, (b) Two-port S-parameters vs. frequency, and (c) small-signal equivalent circuit. In (a) and (b), the solid lines represent the experimental data, and the dashed lines are the ADS simulation results. . . . .	97

4.24	Current dependency of $C_{CB}$ and cut-off frequencies extracted from the device on DHBT58H with $W_{E,design}=200$ nm, $W_{BM,design}=700$ nm, and $L_{E,design}=3$ $\mu$ m at $V_{CE}=1.2, 1.4,$ and $1.7$ V. (a) $C_{CB}$ vs. $J_E$ . (b) $f_\tau$ and $f_{max}$ vs. $J_E$ . . . . .	98
4.25	RF measurement results of a device on DHBT58H with $W_{E,design} = 100$ nm, $W_{BM,design}=600$ nm, and $L_{E,design}=3$ $\mu$ m: (a) unilateral Mason's gain and $H_{21}$ vs. frequency, (b) Two-port S-parameters vs. frequency, and (c) small-signal equivalent circuit. In both (a) and (b), the solid lines represent the experimental data, and the dashed lines are the ADS simulation results. . . . .	100
4.26	Current dependency of $C_{CB}$ and cut-off frequencies extracted from the device on DHBT58H with $W_{E,design}=100$ nm, $W_{BM,design}=600$ nm, and $L_{E,design}=3$ $\mu$ m at $V_{CB}=1.2, 1.4,$ and $1.7$ V. (a) $C_{CB}$ vs. $J_E$ . (b) $f_\tau$ and $f_{max}$ vs. $J_E$ . . . . .	101
4.27	Dimension dependence of (a) $C_{CB}$ (vs. $W_{BM,design}$ ) and (b) $R_{B,cont.}$ (vs. $W_{B,cont.}$ ) from device on DHBT58H with $L_E=2.7$ $\mu$ m biased at $V_{CE}=1.7$ V and $J_E=25\sim 30$ mA/ $\mu$ m <sup>2</sup> . . . . .	102
5.1	The cross-section of the SHBT structure simulated by Sentaurus.	109
5.2	Inverse DC current gain ( $1/\beta$ ) vs. HBT emitter periphery to area ratio ( $P_{je}/A_{je}$ ) of DHBT58H and DHBT63B at $J_E \approx 25$ mA/ $\mu$ m <sup>2</sup> . DHBT58H employs a 20 nm base with doping concentration of $12\text{--}8 \times 10^{19}$ cm <sup>-3</sup> varying from the emitter side to the collector side. DHBT63B has a 25 nm base with lower doping concentration varying from 9 to $5 \times 10^{19}$ cm <sup>-3</sup> . For both samples $W_{gap} \approx 10$ nm according to TEM analysis. . . . .	118
5.3	Experimental and computed inverse DC current gain ( $1/\beta$ ) vs. HBT emitter periphery to area ratio ( $P_{je}/A_{je}$ ) of DHBT58H at $J_E \approx 25$ mA/ $\mu$ m <sup>2</sup> . The simulation assumed $\Delta E_C$ of (a) 0 (b) 26, and (c) 54 meV. . . . .	120
5.4	Experimental and computed inverse DC current gain ( $1/\beta$ ) vs. $P_{je}/A_{je}$ of DHBT58H at $J_E \approx 25$ mA/ $\mu$ m <sup>2</sup> . In (a), the simulation assumed zero $D_{it}$ and $v_{surf.rec.}$ . In the rest of the figures, The simulation assumed $v_{surf.rec.}=5000$ cm/s and $D_{it}$ of (b) $5 \times 10^{12}$ , (c) $1 \times 10^{13}$ , and (d) $5 \times 10^{13}$ cm <sup>-2</sup> eV <sup>-1</sup> . . . . .	123
5.5	The computed electron density near the dielectric/InGaAs interface vs. the depth into the base, at different distance to the edge of the B-E junction. The simulation is base on the base design of DHBT58H with $W_{gap}=30$ nm and assumed $D_{it}=5 \times 10^{13}$ cm <sup>-2</sup> eV <sup>-1</sup> . . . . .	126



5.6	Experimental and computed inverse DC current gain ( $1/\beta$ ) vs. $P_{je}/A_{je}$ of DHBT63B design at $J_E \approx 25\text{mA}/\mu\text{m}^2$ . The simulation assumed $v_{\text{surf.rec.}}=5000\text{ cm/s}$ , $D_{\text{it}}=5\times 10^{13}\text{ cm}^{-2}\text{eV}^{-1}$ , $C_{\text{Auger,p}} = 4\times 10^{-29}\text{ cm}^6/\text{s}$ , and ignored the BGN effect. . . . .	127
5.7	The conduction-band energy vs. the depth into the base at the extrinsic base of (a) a 20 nm base doping-graded from $12$ to $8\times 10^{19}\text{ cm}^{-3}$ , and (b) designs with a 5 nm pulse-doped ( $1.2\times 10^{20}\text{ cm}^{-3}$ ) layer followed by a doping-graded base. Layer structure A has a 15 nm InGaAs graded from $7$ to $4\times 10^{19}\text{ cm}^{-3}$ . Layer structure B has a 10 nm InGaAs graded from $5$ to $3\times 10^{19}\text{ cm}^{-3}$ . . . . .	130
5.8	(a) The Schematic of the simulated SHBTs with a pulse-doped layer. (b) Computed $1/\beta$ vs. $P_{je}/A_{je}$ of the designs at $J_E \approx 26\text{ mA}/\mu\text{m}^2$ . The simulation retained the parameters ( $v_{\text{surf.rec.}}$ , $D_{\text{it}}$ , $C_{\text{Auger,p}}$ , etc.) of DHBT58H and assumed $W_{\text{gap}}=10\text{ nm}$ . . . . .	130
5.9	(a) The Schematic of the simulated SHBTs with the pulse-doped layer removed from the extrinsic base region. (b) Computed $1/\beta$ vs. $P_{je}/A_{je}$ of the designs at $J_E \approx 26 \sim 29\text{ mA}/\mu\text{m}^2$ . The simulation retained the parameters ( $v_{\text{surf.rec.}}$ , $D_{\text{it}}$ , $C_{\text{Auger,p}}$ , etc.) of DHBT58H and assumed $W_{\text{gap}}=10\text{ nm}$ . . . . .	132
5.10	(a) The Schematic of the simulated SHBTs with the recessed B-E junction. (b) Computed $1/\beta$ vs. $P_{je}/A_{je}$ of the designs at $J_E \approx 24 \sim 25\text{ mA}/\mu\text{m}^2$ . The simulation retained the parameters ( $v_{\text{surf.rec.}}$ , $D_{\text{it}}$ , $C_{\text{Auger,p}}$ , etc.) of DHBT58H and assumed $W_{\text{gap}}=10\text{ nm}$ . . . . .	135
6.1	The TEM cross-section of a DHBT in bi-layer refractory base contact process flow; device courtesy of J. C. Rode. . . . .	145
A.1	Flow chart of mesa DHBT fabrication. . . . .	152

# Chapter 1

## Introduction

Because of the escalating need for high-speed and low-power wireless communication systems at the radio-frequency (RF), high-performance transistors has been in rising demand for the past few decades. Among various transistor technologies, double-heterojunction bipolar transistors (DHBTs) offers number of advantages over its competitors. Being a vertical device, the key dimensions which determine the transit times are defined by epitaxy, whereas in planar devices such as the field-effect transistors (FETs), the dimensions are defined by lithography, which is limited by the wavelength of the photons or electrons. As a result, the current gain cut-off frequency ( $f_\tau$ ) of DHBTs has been rapidly improved over the years [1,2]. Because the current in DHBTs is conducted in the bulk semiconductor rather than in the surface inversion layer of a FET, the carriers are less subjected to scattering due to surface traps. This reduces the trap-induced frequency dispersion and results in lower  $1/f$  noise [3].

Among the materials selections of DHBTs, npn-DHBTs based on  $\text{In}_{0.53}\text{Ga}_{0.47}\text{As}/\text{InP}$  has demonstrated a superior performance at the near-THz regime [2]. InP DHBTs with the record current/power gain cut-off frequencies ( $f_\tau/f_{\max}$ ) of  $\sim 0.5/1$  THz has been reported [4,5], which is higher than the value reported from competing material systems such as GaAs/AlGaAs ( $< 0.1$  THz [6]), and SiGe ( $\sim 0.3/0.4$  THz [7–10]). Comparing with the FET approaches, which is current led by the high electron mobility transistors (HEMTs), InP DHBT gives higher  $f_\tau/f_{\max}$  than GaN-based HEMT ( $\sim 0.2/0.4$  THz [11, 12]). InP-based HEMTs attains similar  $f_\tau/f_{\max}$  ( $\sim 0.6/1.0$  THz [13, 14]) as InP DHBTs, though InP DHBTs have demonstrated a higher open-circuit breakdown voltage,  $BV_{\text{CEO}}$  [4,5,15,16]. The superior temporal response of InP system can be attributed to the material properties.

Because of the high electron mobility and large  $\Gamma$ -L valley separation in the conduction band of the InP collector [17], the electron could traverse at high velocity, reducing the transit times. Due to the low effective masses in both n- and p-InGaAs [17], the tunnelling probability of carriers is high, which in return gives lower specific contact resistivity as the doping concentration increases [18], decreasing the parasitic RC delays [2,3]. In addition to high  $f_\tau/f_{\max}$ , the wide band gap (1.4 eV) InP collector enables high  $BV_{\text{CEO}}$ , which is crucial for microwave power amplifiers [2]. Moreover, since it is based on the  $\text{In}_{0.53}\text{Ga}_{0.47}\text{As}/\text{InP}$  system, DHBTs are compatible with the 1.3 to 1.55  $\mu\text{m}$  lightwave communication systems, which makes DHBTs favorable for optical fiber applications [19].

Because of the advantageous RF performance and the compatibility with other InP-base devices, several high performance MMICs utilizing InP DHBTs have been reported to demonstrate the potential of this technology [20,21]. For high-resolution radar/imaging systems, power amplifiers oscillating at  $\sim 220$  GHz with high output power has been reported [22, 23]. For applications in fiber optical communication, a 1-20 GHz phase lock loops (PLLs) has been reported [24] and photonic-electronic integration for wavelength division de-multiplexing (WDM) optical communication systems has been demonstrated [25]. Such architecture has the potential to be scaled beyond the capacity of 1 Tbps [26].

In order to achieve high  $f_\tau/f_{\max}$ , DHBTs must be scaled epitaxially and lithographically to reduce transit times and RC delays. In addition, because the dimensions of emitter and base contact are nano-scaled, both n- and p-InGaAs are heavily doped to retain low access resistance [2]. Prior to the work reported in this dissertation, the emitter width of InP DHBTs has been successfully scaled to

sub-200 nm [27–29]. Based on this technology, half of this dissertation is dedicated to a reliable device scaling to sub-100 nm emitter width. In response to scaling, the reduction of the DC-current gain ( $\beta = I_C/I_B$ ) has been observed experimentally among the devices at a smaller emitter width [4, 30, 31]. Low  $\beta$  would result in a higher noise figure at the transistor level, causing more noise in microwave amplifiers and high error rate in analog ICs. In order to improve DC- $\beta$  in the future scaling generations of DHBTs, another half of this dissertation is devoted to the modeling of DC- $\beta$  in scaled DHBTs.

In the first half of chapter 2, the theory regarding DHBT scaling will be described. The reduction of DC- $\beta$  accompanying with the scaling will be explained in the second half of chapter 2. Chapter 3 will cover the improvements in DHBT process flow which enable a reliable device scaling to 100 nm emitter width and an environments for enhanced accuracy in RF measurements. The experimental results of two samples, DHBT63B and DHBT58H, will be presented in chapter 4. TEM analysis verified the more controllable emitter process flow at the sub-100 nm emitter width node. DC characteristics of the devices show that  $\beta$  reduces from 20 to 15 as the emitter width scales from 200 nm to 100 nm. According to this trend, a  $\beta < 10$  can be extrapolated at 75 nm emitter width assuming the current DHBT design process flow is unchanged. The devices reported in this work exhibit  $f_\tau/f_{\max}$  of  $\sim 500/700$  GHz according to RF measurements, which is lower than expected. The parasitic resistance and capacitance will be analyzed to explain the discrepancy between the designed and experimental RF performance.

Using a commercial simulator, the 2-D electron transport in the base of a DHBT has been emulated, allowing the model for DC- $\beta$  in DHBTs to be con-

structed [31, 32]. In chapter 5, the details regarding the current gain model will be addressed. The assumptions and parameters used in the simulation will be justified base on experimental data obtained from DHBT samples. The model indicates that DC- $\beta$  in scaled DHBTs is limited by base current originated from bulk recombination and lateral electron diffusion. In order to suppress the base current and improve  $\beta$ , modifications to the design of base-emitter junction are proposed. The current gain in devices with the modified base-emitter junction has been computed using the established model, and will be presented at the end of chapter 5. If the modifications could be adequately integrated into DHBT fabrication, a device at sub-100 nm emitter node with simultaneously  $\beta$  of 50 [33] and  $f_{\max}$  of 1 THz should be plausible.

## References

- [1] M. J. W. Rodwell, M. Urteaga, T. Mathew, D. Scotts, D. Mensa, Q. Lee, J. Guthrie, Y. Betser, S. C. Martin, R. P. Simth, S. Jaganathan, S. Krishnan, S. I. Long, L. Pullela, B. Agarwal, U. Bhattacharya, L. Samoska, and M. Dahlström, “Submicron scaling of HBTs,” *IEEE Trans. Electron Devices*, vol. 48, p. 2606, Nov. 2001.
- [2] M. J. W. Rodwell, M. Le, and B. Brar, “InP Bipolar ICs: Scaling Roadmaps, Frequency Limits, Manufacturable Technologies,” *Proc. IEEE*, vol. 92, pp. 271–286, Feb. 2008.
- [3] J. S. Yuan, *SiGe, GaAs, and InP Heterojunction Bipolar Transistors*. Wiley, 1999.
- [4] V. Jain, J. C. Rode, H. W. Chiang, A. Baraskar, E. Lobisser, B. J. Thibeault, M. J. W. Rodwell, M. Urteaga, D. Loubychev, A. Snyder, Y. Wu, J. M. Fastenau, and W. Liu, “1.0 THz  $f_{\max}$  InP DHBTs in a refractory emitter and self-aligned base process for reduced base access resistance,” in *69th IEEE Device Research Conference*, Jun. 2011.
- [5] M. Urteaga, R. Pierson, P. Rowell, V. Jain, E. Lobissor, and M. J. W. Rodwell, “130 nm InP DHBTs with  $f_{\tau} > 0.52$  THz and  $f_{\max} > 1.1$  THz,” in *69th IEEE Device Research Conference*, Jun. 2011.
- [6] P. M. Asbeck, M. F. Chang, W. K. C., D. L. Miller, G. J. Sullivan, N. H. Sheng, E. Sovero, and J. A. Higgins, “Heterojunction Bipolar Transistors for Microwave and Millimeter-wave Integrated Circuits,” *IEEE Trans. Microw. Theory Techn.*, vol. 35, p. 1462, Dec. 1987.
- [7] J.-S. Rieh, B. Jagannathan, H. Chen, K. Schonenberg, S.-J. Jeng, M. Khater, D. Ahlgren, G. Freeman, and S. Subbanna, “Performance and design considerations for high speed SiGe HBTs of  $f_{\tau}/f_{\max}=375$  GHz/210 GHz,” in *15th International Conference on Indium Phosphide and Related Materials*, May. 2003.
- [8] P. Chevalier, F. Pourchon, T. Lacave, G. Avenier, Y. Campidelli, L. Depoyan, G. Troillard, M. Buczko, D. Gloria, D. Celi, C. Gaquiere, and A. Chantre, “A Conventional double-polysilicon FSA-SEG Si/SiGe:C HBT reaching 400 GHz  $f_{\max}$ ,” in *2009 Bipolar/BiCMOS Circuits and Technology Meeting*, Oct. 2009.
- [9] S. Van Huylenbroeck, A. Sibaja-Hernandez, R. Venegas, S. You, G. Winderickx, D. Radisic, W. Lee, P. Ong, T. Vandeweyer, N. Nguyen, K. De Meyer,

## REFERENCES

---

- and S. Decoutere, “A 400 GHz  $f_{\max}$  fully self-aligned SiGe:C HBT architecture,” in *2009 Bipolar/BiCMOS Circuits and Technology Meeting*, Oct. 2009.
- [10] R. A. Camillo-Castillo, Q. Z. Liu, J. W. Adkisson, M. H. Khater, P. B. Gray, V. Jain, R. K. Leidy, J. J. Pekarik, J. P. Gambino, B. Zetterlund, C. Willets, C. Parrish, S. U. Engelmann, A. M. Pyzyna, P. Cheng, and D. L. Harame, “SiGe HBTs in 90 nm BiCMOS Technology demonstrating 300 GHz/420 GHz  $f_{\tau}/f_{\max}$  through reduced  $R_b$  and  $C_{cb}$  parasitics,” in *2013 Bipolar/BiCMOS Circuits and Technology Meeting*, Oct. 2013.
- [11] K. Shinohara, A. Corrion, D. Regan, I. Milosavljevic, D. Brown, S. Burnham, P. Willadsen, C. Butler, A. Schmitz, D. Wheeler, A. Fung, and M. Micovic, “220 GHz  $f_{\tau}$  and 400 GHz  $f_{\max}$  in 40-nm GaN DH-HEMTs with regrown ohmic,” in *2010 International Electron Devices Meeting*, Dec. 2010.
- [12] D. Denninghoff, J. Lu, E. Ahmadi, S. Keller, and U. K. Mishra, “N-polar GaN/InAlN/AlGaIn MIS-HEMTs with 1.89 S/mm extrinsic transconductance, 4 A/mm drain current, 204 GHz  $f_{\tau}$  and 405 GHz  $f_{\max}$ ,” in *71th IEEE Device Research Conference*, Jun. 2013.
- [13] D.-H. Kim, J. del Alamo, P. Chen, W. Ha, M. Urteaga, and B. Brar, “50-nm E-mode In<sub>0.7</sub>Ga<sub>0.3</sub>As PHEMTs on 100-mm InP substrate with  $f_{\max} > 1$  THz,” in *2010 International Electron Devices Meeting*, Dec. 2010.
- [14] D.-H. Kim, B. Brar, and J. del Alamo, “ $f_{\tau} = 688$  GHz and  $f_{\max} = 800$  GHz in  $L_g = 40$  nm In<sub>0.7</sub>Ga<sub>0.3</sub>As MHEMTs with  $g_{m\max} > 2.7$  mS/ $\mu$ m,” in *2011 International Electron Devices Meeting*, Dec. 2011.
- [15] M. Feng and W. Snodgrass, “InP Pseudomorphic Heterojunction Bipolar Transistor (PHBT) With  $f_{\tau} > 750$  GHz,” in *19th International Conference on Indium Phosphide and Related Materials*, May. 2007.
- [16] W. Snodgrass and M. Feng, “Nano-scale Type-II InP/GaAsSb DHBTs to Reach THz Cutoff Frequencies,” in *2008 International Conference on Compound Semiconductor Manufacturing Technology*, Apr. 2008.
- [17] I. Vurgaftman, J. Meyer, and L. Ram-Mohan, “Band parameters for III V compound semiconductors and their alloys,” *J. Appl. Phys.*, vol. 89, p. 5815, Jun. 2001.
- [18] A. Baraskar, A. C. Gossard, and M. J. W. Rodwell, “Lower limits to metal-semiconductor contact resistance: Theoretical models and experimental data,” *J. Appl. Phys.*, vol. 114, p. 154516, Oct. 2013.



## REFERENCES

---

- [19] T. Enoki, E. Sano, and T. Ishibashi, *Prospects of InP-based IC technologies for 100-Gbit/s-class lightwave communications systems*. World Scientific, 2001.
- [20] J. Hacker, M. Seo, A. Young, Z. Griffith, M. Urteaga, T. B. Reed, M. J. W. Rodwell, and M. Field, “THz MMICs based on InP HBT Technology,” in *2010 MTT-S International Microwave Symposium Digest (MTT)*, May 2010.
- [21] L. A. Coldren, M. Lu, H.-C. Park, E. Bloch, J. S. Parker, L. A. Johansson, and M. J. W. Rodwell, “New Opportunities for Optical Phase-locked Loops in Coherent Photonics,” in *2013 Conference on Optical Fiber Communication*, Mar. 2013.
- [22] Z. Griffith, T. B. Reed, M. J. W. Rodwell, and M. Field, “A 220 GHz Solid-State Power Amplifier MMIC with 26.8 dB  $S_{21}$  Gain, and 55.5 mW  $P_{out}$  at 17.0 dB Compressed Gain ,” in *2013 International Microwave Symposium*, Jun. 2013.
- [23] T. B. Reed, Z. Griffith, P. Rowell, M. Field, and M. J. W. Rodwell, “A 180mW InP HBT Power Amplifier MMIC at 214 GHz,” in *IEEE Compound Semiconductor IC Symposium*, Oct. 2013.
- [24] E. Bloch, H.-C. Park, T. B. Lu, M. Reed, Z. Griffith, L. A. Johansson, L. A. Coldren, D. Ritter, and M. J. W. Rodwell, “A 120 GHz InP HBT phase-lock-loop IC for optical wavelength synthesis,” in *2012 MTT-S International Microwave Symposium Digest (MTT)*, Jun. 2012.
- [25] M. Lu, J. S. Park, H.-C. and Parker, E. Bloch, A. Sivananthan, Z. Griffith, L. A. Johansson, M. J. W. Rodwell, and L. A. Coldren, “A Heterodyne Optical Phase-locked Loop for Multiple Applications,” in *2013 Conference on Optical Fiber Communication*, Mar. 2013.
- [26] H.-C. Park, M. Piels, E. Bloch, M. Lu, A. Sivananthan, Z. Griffith, L. Johansson, J. E. Bowers, L. A. Coldren, and M. J. W. Rodwell, “Integrated Circuits for Wavelength Division De-multiplexing in the Electrical Domain,” in *European Conference on Optical Fiber Communication*, Sep. 2013.
- [27] V. Jain, E. Lobisser, A. Baraskar, B. J. , Thibeault, M. J. W. Rodwell, Z. Griffith, M. Urteaga, D. Loubychev, A. Snyder, Y. Wu, J. M. Fastenau, and W. K. Liu, “InGaAs/InP DHBTs in a Dry-Etched Refractory Metal Emitter Process Demonstrating Simultaneous  $f\tau/f_{max} \sim 430/800$  GHz,” *IEEE Electron Device Lett.*, vol. 32, pp. 24–26, Jan. 2011.

## REFERENCES

---

- [28] E. Lind, A. M. Crook, Z. Griffith, M. J. W. Rodwell, X.-M. Fang, D. Loubychev, Y. Wu, J. M. Fastenau, and W. Liu, "560 GHz  $f_\tau$ ,  $f_{\max}$  InGaAs/InP DHBT in a novel dry-etched emitter process," in *65th IEEE Device Research Conference*, Jun. 2007.
- [29] E. Lobisser, J. C. Rode, V. Jain, H. Chiang, A. Baraskar, W. J. Mitchell, B. J. Thibeault, and M. J. W. Rodwell, "InGaAs/InP DHBTs with Emitter and Base Defined through Electron-Beam Lithography for Reduced  $C_{cb}$  and Increased RF Cut-off Frequency," in *39th International Symposium on Compound Semiconductors*, Aug. 2012.
- [30] Z. Griffith, E. Lind, and M. J. W. Rodwell, "Sub-300nm InGaAs/InP Type-I DHBTs with a 150 nm collector, 30 nm base demonstrating 755 GHz  $f_{\max}$  and 416 GHz  $f_\tau$ ," in *19th International Conference on Indium Phosphide and Related Materials*, May. 2007.
- [31] H. W. Chiang, J. C. Rode, P. Choudhary, and M. J. W. Rodwell, "Lateral Carrier Diffusion and Current Gain in THz InGaAs/InP DHBTs," *J. Appl. Phys.*, vol. 115, p. 034513, Jan. 2014.
- [32] H. W. Chiang, J. C. Rode, P. Choudhary, and M. J. W. Rodwell, "Interfacial transport and current gain in InGaAs/InP DHBTs for THz applications," in *72nd IEEE Device Research Conference*, Jun. 2014.
- [33] H. W. Chiang, J. C. Rode, P. Choudhary, and M. J. W. Rodwell, "Optimization of DC performance in terahertz InGaAs/InP double-heterojunction bipolar transistors," *J. Appl. Phys.*, submitted.

## Chapter 2

# DHBT Theory

In this chapter, the theory and the designs of mesa-DHBTs for THz applications will be examined from two aspects: RF and DC characteristics. The structure of the state of the art mesa-DHBT will be briefly described. The transit times and RC delays associated with the parasitic resistance and capacitance will be discussed. The expressions of two important figures of merit, current gain ( $H_{21}$ ) cut-off frequency,  $f_\tau$ , and the power gain (unilateral Mason's gain, U) cut-off frequency,  $f_{\max}$ , will be given. From the expressions, the scaling law of DHBTs to achieve higher  $f_\tau$  and  $f_{\max}$  will be defined. As the transistors are scaled, the DC-current gain ( $\beta$ ) decreases. To investigate the decrease of  $\beta$ , various sources of the base current will be examined.

## 2.1 Device Structure

The cross-section of a mesa-DHBT is shown in fig. 2.1a. The refractory metal contact, which defines the base-emitter (B-E) junction, is formed on a heavily doped n-In<sub>0.53</sub>Ga<sub>0.47</sub>As emitter cap. The emitter cap and the n-InP emitter, encapsulated by SiN<sub>x</sub> sidewall, are formed by a wet etch stopped at the doping graded p-In<sub>x</sub>Ga<sub>1-x</sub>As base, after which a self-aligned base contact is deposited on top of the base. Starting from the bottom of the base, the lightly doped n-type collector region is composed of the In<sub>0.53</sub>Ga<sub>0.47</sub>As setback, the In<sub>0.53</sub>Ga<sub>0.47</sub>As/In<sub>0.52</sub>Al<sub>0.48</sub>As superlattice B-C grade, a  $\delta$ -doping, and the InP collector. The setback beneath the base region supplies enough kinetic energy to the electrons for them to cross the B-C grade. The base-collector (B-C) junction, whose area defined by the base

contact, is formed by a wet etch terminated at the heavily doped n-type sub-collector. Finally, the collector contact are deposited on the sub-collector.

Fig. 2.1b is the top-down view a mesa-DHBTs. To isolate the devices, the sub-collector and a portion of the semi-insulating substrate in the field are wet etched. To avoid oscillation modes due to the InP substrate, the base and the collector terminals are raised to the same plane as the emitter via metal posts on the contact pad, after which transmission line structures are built on top of the device. Fig. 2.1d is the SEM of a device after the front end process.

The important dimensions of a DHBT is shown in fig. 2.1c. Due to symmetry, only half of the cross-section is shown.  $W_E$  and  $L_E$  is the B-E junction width and length defined by the emitter metal stack. The self-aligned base metals with a width of  $(W_{B,cont.} + W_{UC})$  are deposited on both sides of the emitter. Because of the  $\text{SiN}_x$  sidewall, a gap (extrinsic base) is formed between the emitter and the self-aligned base contact. The distance between the emitter and the base contact is  $W_{gap}$ . The base contact penetrates the base semiconductor for a depth of  $T_{B,sink}$  due to the reaction between the base metal and InGaAs [1]. The width of the B-C mesa ( $W_{BM}$ ) is defined by the widths of the base metal and the emitter. Due to the wet etch undercut ( $W_{UC}$ ), the actual width of the base mesa is  $(W_{BM} - 2W_{UC})$ , and the base contact width is  $W_{B,cont.}$ .  $T_B$  and  $T_C$  are the thickness of base and collector semiconductors, respectively.

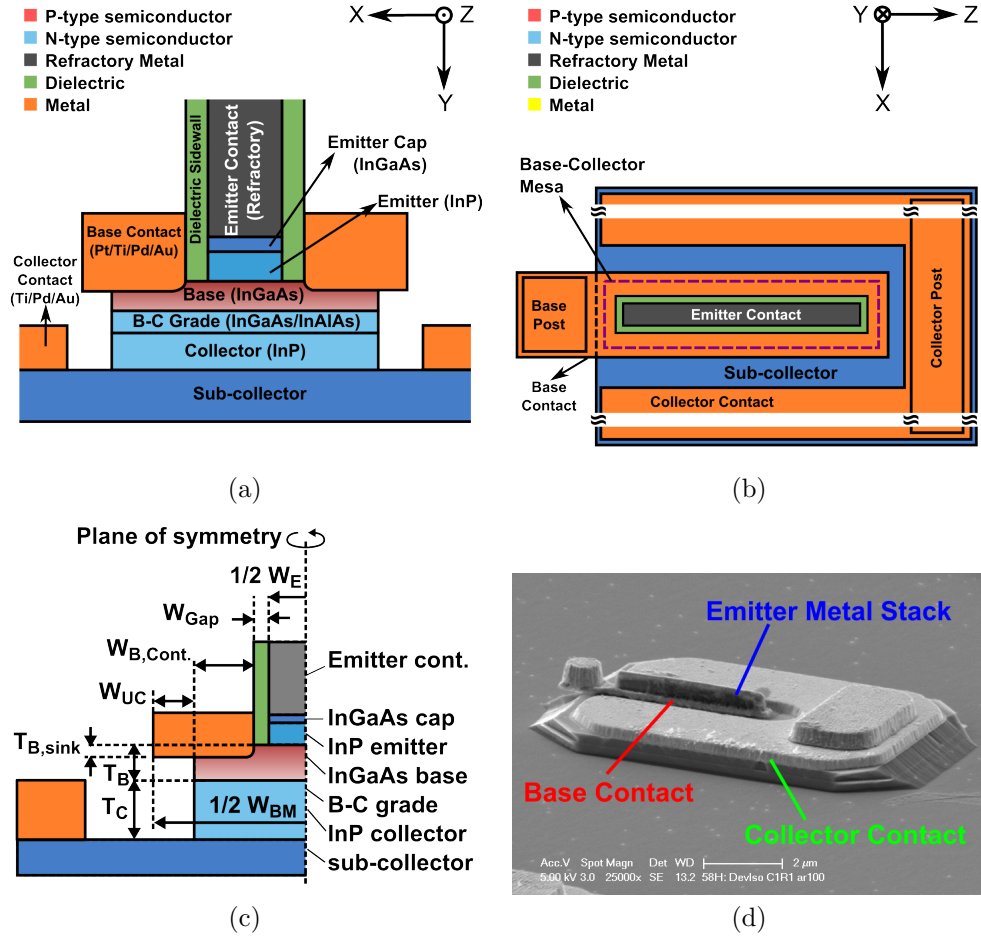


Figure 2.1: The structure of mesa-DHBTs. (a) The cross-section of a DHBT. (b) The top-down view of a DHBT. (c) The schematic showing the important dimensions in DHBTs. Only half of the device is shown due to symmetry. (d) The SEM of an experimental device after the front end process.

## 2.2 RF Characteristics and DHBT Scaling Laws

In this section, the design and scaling laws of THz DHBTs will be covered [2]. To understand the scaling laws, the RF characteristics of DHBTs must be addressed. The small-signal equivalent circuit of HBT based on the hybrid- $\pi$  model [3] will be presented. Each delay term will be described, and the expressions of  $f_\tau$  and  $f_{\max}$  will be derived using these terms. By reducing the delays through device scaling, the cut-off frequencies of the DHBTs can be increased.

### 2.2.1 Small-signal AC Equivalent Circuit

Fig. 2.2 is the small-signal equivalent circuit of a DHBT in the common emitter configuration approximated by hybrid- $\pi$  model.  $R_{EX}$ ,  $R_{BB}$ , and  $R_C$  are the access resistances of the emitter, base, and collector terminals.  $R_{BE}$  and  $C_{BE}$  are the input resistance and capacitance associated with the B-E junction. The feed back components,  $R_{CB}$  and  $C_{CB}$ , are the resistance and capacitance associated with the B-C junction.  $C_{CB}$  is separated into the intrinsic term ( $C_{CB,i}$ ), which is the component in the active region (beneath the B-E junction), and the extrinsic term ( $C_{CB,x}$ ), which accounts for the capacitance of the rest of the B-C mesa.  $g_m$  is the device transconductance.  $\tau_p$  is the sum of the base transit time ( $\tau_B$ ) and collector transit time ( $\tau_C$ ).  $C_{CG}$  is the parasitic capacitance of the low-k dielectric resin (BCB) between the ground plane and the collector contact. The aforementioned parasitic terms and the delay associated with them will be discussed in the rest of this section.

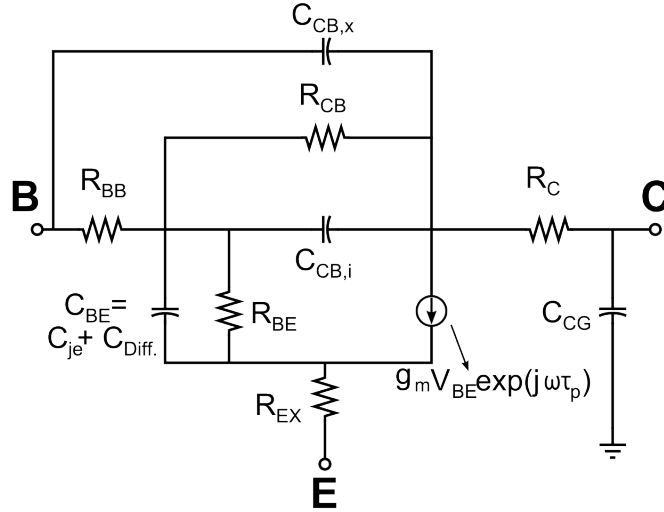


Figure 2.2: The small-signal equivalent circuit of a DHBT approximated by the hybrid- $\pi$  model.

### 2.2.2 Base and Collector Transit Time

The base transit time ( $\tau_B$ ) and collector transit time ( $\tau_C$ ) are critical terms in determining  $f_\tau$ . Because  $f_{\max}$  is determined by  $f_\tau$ , it is also affected. The transit times depend on the designs of base and collector region. In this section, the relation between the base/collector transit times and the base/collector designs will be discussed.

In DHBTs, the base is usually graded (either via doping or alloy composition), causing an potential difference in the conduction band ( $\Delta E_C$ ) between the emitter side and the collector sides of the base, as shown in the band diagram in fig. 2.3. Thus, a quasi-electric field is generated, accelerating the electrons towards the collector region. In the presence of such electric field, the electron transit time in



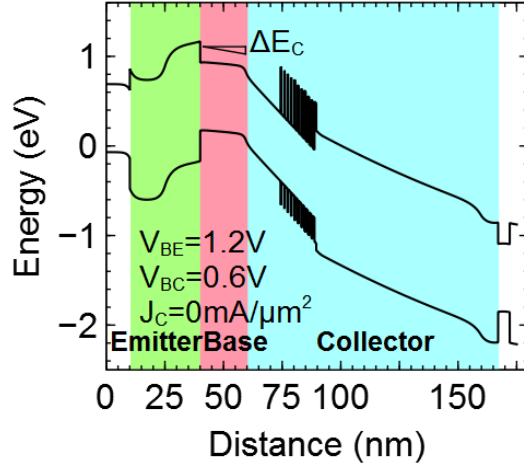


Figure 2.3: The band diagram of a DHBT in the forward active mode. The band gap narrowing effect and the space charge region in the collector are neglected.

the base region is given by [4]:

$$\tau_B = \frac{T_B^2}{D_n} \frac{kT}{\Delta E_C} \left[ 1 - \frac{kT}{\Delta E_C} (1 - \exp(-\frac{\Delta E_C}{kT})) \right] + \frac{T_B}{v_{\text{exit}}} \frac{kT}{\Delta E_C} (1 - \exp(\frac{\Delta E_C}{kT})), \quad (2.1)$$

where  $D_n$  is the electron diffusivity,  $k$  is the Boltzmann constant, and  $T$  is the temperature.  $v_{\text{exit}}$  is the velocity of the electrons leaving the base and entering the collector.

Increasing  $\Delta E_C$  reduces  $\tau_B$ , and hence improves  $f_\tau$  and  $f_{\text{max}}$ . The UCSB DHBT designs employ the doping graded base, which generates  $\Delta E_C \approx 60$  meV if the band gap narrowing effect at high doping concentration is ignored. In reality, the band gap narrowing (BGN) effect cannot be neglected [5], which decreases the  $\Delta E_C$  induced by the doping grade. As a result,  $\tau_B$  is underestimated. Therefore, for base designs with high doping concentration, band gap narrowing effect should be taken into the consideration when calculating  $\tau_B$ . Decreasing the base thick-

ness,  $T_B$ , also reduces  $\tau_B$ . However, the base metal penetrates the InGaAs base for certain depth ( $T_{B,\text{sink}}$ ) [1], as shown in fig. 2.1c. Thus, the B-C junction could be shorted if the base is too thin, i.e. when  $T_B \approx T_{B,\text{sink}}$ . According to the TEM analysis in chapter 4,  $T_{B,\text{sink}} > 5 \text{ nm}$  for Pt/Ti/Pd/Au base contact. In order to decrease  $T_B$  without forming a shunt path to the B-C junction, refractory metal should be used to replace Pt/Ti/Pd/Au for a shorter  $T_{B,\text{sink}}$ .

The collector transit time ( $\tau_C$ ) can be obtained using the charge control analysis. As more electrons are being injected into the collector due to an increase in the collector current ( $\Delta I_C$ ), a sheet of charge is induced at the collector side of the base ( $\Delta Q_C$ ).  $\tau_C$  is defined as the amount of time required for  $\Delta I_C$  to charge this induced  $\Delta Q_C$ , i.e.

$$\tau_C = \frac{\Delta Q_C}{\Delta I_C} = \int_0^{T_C} \frac{1 - x/T_C}{v(x)} dx = \frac{T_C}{2v_{\text{eff}}}, \quad (2.2)$$

where  $v(x)$  and  $v_{\text{eff}}$  are the position-dependent and effective velocities in the collector. If electrons accumulate enough kinetic energy as they traverse through the collector, they may scatter from the  $\Gamma$ -valley into the L-valley in the conduction band. Because the velocity in the L-valley is lower,  $v_{\text{eff}}$  decreases and  $\tau_C$  increases. For InGaAs and InP, the energy differences between the  $\Gamma$ - and the L-valleys, are 0.55 and 0.6 eV, respectively. Because of the large separations, the  $\Gamma$ -L scattering is less likely to occur in InP DHBTs [6].

### 2.2.3 Emitter Charging Time

The input capacitance,  $C_{BE}$ , in fig. 2.2 can be separated into two terms: the diffusion capacitance,  $C_{Diff.} = g\tau_p$ , and the depletion capacitance of the B-E junction,  $C_{je}$ . Because the base is heavily doped, the depletion region in the base can be neglected. The depletion term is given by:

$$C_{je} = \frac{\epsilon_0 \epsilon_r A_{je}}{T_{E,dep.}} , \quad (2.3)$$

where  $\epsilon_0$  and  $\epsilon_r$  are the vacuum permittivity and the relative permittivity of InP ( $\epsilon_r \approx 13$  [7]).  $T_{E,dep.}$  is the depletion region depth in the InP emitter.

The device transconductance,  $g_m$ , is defined as:

$$g_m = \frac{\partial I_C}{\partial V_{BE}} = \frac{qI_E}{\eta kT} , \quad (2.4)$$

where  $\eta$  is the ideality factor. The values of  $g_m$  and  $\eta$  are usually obtained from the real part of the network expression  $Y_{21}$ , measured at low frequency, which can be written as [8]:

$$\frac{1}{Re(Y_{21})} = R_{EX} + \frac{R_{BB}}{\beta} + \frac{\eta kT}{qI_E} , \quad (2.5)$$

where  $\beta$  is obtained from DC measurements. From the slope of inverse  $Re(Y_{21})$  vs. inverse  $I_E$ ,  $\eta$  can be extrapolated.

The charging delay associated with  $C_{je}$  and  $g_m$  is

$$\frac{C_{je}}{g_m} = \frac{\eta kT}{qI_E} C_{je} . \quad (2.6)$$

## 2.2.4 Collector Charging Time

There is also the delay  $(R_{EX} + R_C + 1/g_m)C_{CB}$ , in order to charge the feedback capacitance,  $C_{CB}$ . The value of  $C_{CB}$  is obtained from the imaginary part of  $Y_{12}$  in the network expression [9], i.e.

$$Im(Y_{21}) = \omega(C_{CB,i} + C_{CB,x}) . \quad (2.7)$$

$C_{CB}$  includes the terms associated with the static and the mobile (space) charge in the depletion region of the base-collector junction, which can be written as

$$\begin{aligned} C_{CB} &= \frac{dQ_C}{dV_{CB}} = \frac{\epsilon_0 \epsilon_r A_C}{T_{C,eff}} - \frac{\partial(I_C \tau_C)}{\partial V_{CB}} \\ &= \frac{\epsilon_0 \epsilon_r A_C}{T_{C,dep.}} - I_C \frac{\partial \tau_C}{\partial V_{CB}} - \tau_C \frac{\partial I_C}{\partial V_{CB}} \\ &\approx \frac{\epsilon_0 \epsilon_r A_C}{T_{C,dep.}} - I_C \frac{\partial \tau_C}{\partial V_{CB}}, \end{aligned} \quad (2.8)$$

where  $A_C$  and  $T_{C,dep.}$  are the area and the depletion region depth of the base-collector junction, respectively.  $I_C$  and  $\tau_C$  are the collector current and transit time, respectively. Again, since the base is heavily doped, only the depletion region in the InP collector is considered ( $\epsilon_r \approx 13$ ). The approximation holds when the output conductance ( $\partial I_C / \partial V_{CB}$ ) is negligible, i.e. when  $R_{CB}$  is very high, which is the case for the reversed biased base-collector junction.

The collector of DHBTs is usually designed to be doped at the concentration where the collector is fully depleted, i.e.  $T_{C,dep.} \approx T_C$ , at low  $I_C$  and certain  $V_{CB}$ . Thus, at low  $I_C$ , the static term in eq. 2.8 remains constant. When  $I_C > 0$ , the space charge due to injected electrons screens the positive charge in the depletion

region. Thus, as  $I_C$  increases, the electric field in the depletion region decreases in magnitude. Eventually, the field reverse its direction, inducing a barrier to electrons. This is known as the Kirk effect. The current density at the onset of the Kirk effect is given by

$$J_{C,Kirk} = \frac{2\epsilon_0\epsilon_r v_{eff.}}{T_C^2} (V_{bi} + V_{CB}) + qN_{D,C}v_{eff.} , \quad (2.9)$$

where  $V_{bi}$  is the built-in voltage of the B-C junction, and  $N_{D,C}$  is the collector doping concentration. As  $J_C$  (or  $J_E$ ) increases beyond  $J_{C,Kirk}$ , the effective depletion region depth in the collector reduces (base push-out), and the static term in eq. 2.8 starts to increase.

As  $V_{CB}$  increases, the electron velocity in the collector ( $v_{eff.}$ ) decreases and hence  $\tau_C$  increases, i.e.  $\partial\tau_C/\partial V_{CB} > 0$  [10]. Therefore, the second term in eq. 2.8 decreases as  $I_C$  increases. Fig. 2.4 shows  $C_{CB}$  vs.  $J_E$  measured from an experimental device. As a result of velocity modulation and base push-out, when  $I_C$  increases, the overall  $C_{CB}$  first decreases. Near the onset of the Kirk effect,  $C_{CB}$  reaches minimum, and then increases with  $I_C$ . Because  $C_{CB}$  is associated with multiple delay terms which determine  $f_\tau$  and  $f_{max}$ , the current density when  $C_{CB}$  reaches minimum is usually close to the bias condition for peak RF performance for a given  $V_{CB}$ .

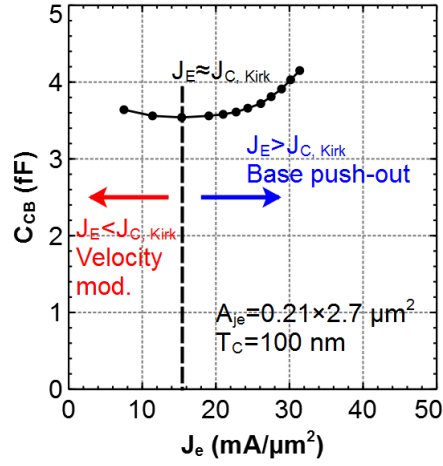


Figure 2.4: Experimental  $C_{CB}$  vs.  $J_E$  measured from a device with  $W_E=210$  nm and  $T_C=100$  nm (DHBT58H).

## 2.2.5 Cutoff Frequencies

The current gain cut-off frequency,  $f_\tau$ , and the power gain cut-off frequency,  $f_{max}$ , are two important figures of merit in evaluating the RF performance of a DHBT. The current gain cut-off frequency,  $f_\tau$ , is the frequency when  $H_{21}$  drops to unity. From the summation of the transit times and the charging delays,  $f_\tau$  is given by

$$\frac{1}{2\pi f_\tau} = \tau_{EC} = \tau_B + \tau_B + \frac{\eta k T}{q I_E} C_{je} + (R_{EX} + R_C + \frac{\eta k T}{q I_E}) C_{CB}, \quad (2.10)$$

where  $\tau_{EC}$  is the total delay between the emitter and collector contacts. If the transit times and the charging delays can be reduced,  $f_\tau$  can be improved.

The power gain cut-off frequency,  $f_{max}$ , is defined as the frequency when the unilateral Mason's gain becomes unity. Its value is determined by  $f_\tau$  and the charging delay due to the distributed resistance-capacitance (R-C) network in the

B-C mesa. The expression of  $f_{\max}$  is given by

$$f_{\max} = \sqrt{\frac{f_{\tau}}{8\pi(RC)_{\text{eff}}}} \quad (2.11)$$

where  $(RC)_{\text{eff}}$  is the charging delay associated with the distributed R-C network in the B-C mesa. Fig. 2.5 is the zoomed-in cross-section of the B-C mesa showing the R-C network.  $R_{\text{BE,spread}}$  is the spreading resistance beneath the B-E junction.  $R_{\text{gap}}$  is the resistance in the extrinsic base region between the B-E junction and the base contact.  $R_{\text{B,cont.}}$  is the term from the network of the vertical base contact resistance,  $R_{\text{B,cont. vert.}}$ , and horizontal spreading resistance under the base contact,  $R_{\text{B,cont. spread}}$ . There is also a base metal resistance  $R_{\text{B,metal}}$  along the direction of the emitter stripe, which is not shown in the schematic. Each resistance term is given by [8]

$$\begin{aligned} R_{\text{BE,spread}} &= \frac{R_{\text{sh,em}}W_{\text{E}}}{12L_{\text{E}}} & , R_{\text{gap}} &= \frac{R_{\text{sh,gap}}W_{\text{gap}}}{2L_{\text{E}}} \\ R_{\text{B,cont. vert.}} &= \rho_{\text{B,cont.}}W_{\text{B,cont.}}L_{\text{E}} & , R_{\text{B,cont. spread}} &= \frac{R_{\text{sh,B,cont.}}W_{\text{B,cont.}}}{6L_{\text{E}}} \\ R_{\text{B,metal}} &= \frac{R_{\text{sh,metal}}L_{\text{E}}}{6W_{\text{B,cont.}}}, \end{aligned} \quad (2.12)$$

where  $R_{\text{sh,em}}$ ,  $R_{\text{sh,gap}}$ , and  $R_{\text{sh,B,cont.}}$  are the sheet resistance of the base semiconductor beneath the B-E junction, within the extrinsic base, and beneath the base contact.  $R_{\text{sh,metal}}$  is the sheet resistance of the base metal, which is small when compared with other sheet resistance terms. As a result,  $R_{\text{B,metal}} < 1 \Omega$ , and hence it is usually neglected.  $\rho_{\text{B,cont.}}$  is the specific contact resistivity of the base contact. The transfer length of the base contact,  $L_{\text{T}}$ , is defined as  $\sqrt{\rho_{\text{B,cont.}}/R_{\text{sh,B,cont.}}}$ .

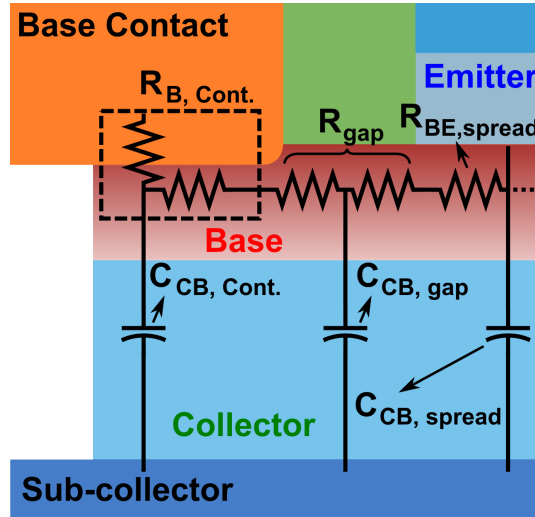


Figure 2.5: The schematic of the distributed R-C network in the base-collector mesa in a DHBT.

When  $W_{B,cont.} > 2L_T$ ,  $R_{B,cont.}$  can be written as

$$R_{B,cont.} = \frac{\sqrt{R_{sh,B,cont.}\rho_{B,cont.}}}{2L_E} \coth\left(\frac{W_{B,cont.}}{L_T}\right), \quad (2.13)$$

For  $\rho_{B,cont.} = 4 \Omega - \mu m^2$  and  $R_{sh,B,cont.} = 800 \Omega/\square$ ,  $L_T \approx 70$  nm. In scaled DHBTs,  $W_{B,cont.}$  is close to  $L_T$ , and hence  $R_{B,cont.}$  increases rapidly as  $W_{B,cont.}$  decreases. Thus,  $R_{B,cont.}$  is the dominant term of the base access resistance,  $R_{BB}$  [9].

$R_{BB}$  is the sum of the resistance terms:

$$\begin{aligned} R_{BB} &\approx R_{BE,spread} + R_{gap} + R_{B,cont.} \\ &= \frac{R_{sh,em}W_E}{12L_E} + \frac{R_{sh,gap}W_{gap}}{2L_E} + \frac{\sqrt{R_{sh,B,cont.}\rho_{B,cont.}}}{2L_E} \coth\left(\frac{W_{B,cont.}}{L_T}\right). \end{aligned} \quad (2.14)$$

As shown in fig. 2.5,  $C_{CB}$  is also separated into segments with a corresponding resistance associated with each of them. The total delay in the B-C mesa,



$(RC)_{\text{eff.}}$ , is given by

$$\begin{aligned}
(RC)_{\text{eff.}} &= C_{\text{CB,spread}}(R_{\text{BE,spread}} + R_{\text{gap}} + R_{\text{B,cont.}}) \\
&+ C_{\text{CB,gap}}(R_{\text{gap}}/2 + R_{\text{B,cont.}}) \\
&+ C_{\text{CB,cont.}}\left(\frac{1}{R_{\text{B,cont. vert.}}} + \frac{1}{R_{\text{B,cont. spread}}}\right)^{-1},
\end{aligned} \tag{2.15}$$

where the area for estimating  $C_{\text{CB,spread}}$ ,  $C_{\text{CB,gap}}$ , and  $C_{\text{CB,cont.}}$  scale with,  $W_{\text{E}}$ ,  $W_{\text{gap}}$ , and  $W_{\text{B,cont.}}$ , respectively.

## 2.2.6 DHBT Scaling Law

In order to increase  $f_{\tau}$  and  $f_{\text{max}}$  in a DHBT, the device has to be scaled in both lateral and epitaxial dimensions [11]. In this section, the scaling consideration in terms of cut-off frequencies will be discussed.

A  $\gamma:1$  increment in  $f_{\tau}$  requires a  $\gamma:1$  reduction in all transit times and charging delay in eq. 2.10. According to eq. 2.1, in order to reduce the base transit time,  $T_{\text{B}}$  need to be reduced approximately by  $\gamma^{1/2}:1$ . From eq. 2.2, a  $\gamma:1$  reduction in  $T_{\text{C}}$  is necessary for the collector transit time to decrease by a factor of  $\gamma$ . However, decreasing  $T_{\text{C}}$  by a factor of  $\gamma$  causes the static term of  $C_{\text{CB}}$  in eq. 2.8 to rise by a factor of  $\gamma$ , which increases the collector charging time in eq. 2.10 by a factor of  $\gamma$ . Thus, in order to decrease the collector charging time by a factor of  $\gamma$ , the area of the B-C junction ( $A_{\text{C}} = W_{\text{BM}}L_{\text{E}}$ ) must be reduced by a factor of  $\gamma^2$  while the resistance terms associated with  $C_{\text{CB}}$  remain constant. For thermal and power dissipation considerations, the B-E junction area ( $A_{\text{je}} = W_{\text{E}}L_{\text{E}}$ ) usually scales with  $A_{\text{C}}$ , and only  $W_{\text{BM}}$  and  $W_{\text{E}}$  are changed while  $L_{\text{E}}$  remains constant.

As a result, the emitter charging time in eq. 2.10 is also decreased by a factor of  $\gamma^2$  if  $I_E$  remains the same. For constant  $I_E$ , the emitter current density  $J_E$  increases by a factor of  $\gamma^2$  because  $A_{je}$  decreases by a factor of  $\gamma^2$ . Furthermore, since the emitter contact area and  $A_{je}$  are approximately the same, the specific emitter contact resistivity,  $\rho_{E,cont.}$ , must be decreased by a factor of  $\gamma^2$ .

According to eq. 2.11, in addition to the  $\gamma:1$  increment in  $f_\tau$ , the delay from the B-C mesa ( $(RC)_{eff.}$ ) needs to be reduced by a factor of  $\gamma$  in order to improve  $f_{max}$  by a factor of  $\gamma$ . Since  $C_{CB}$  already need to be decreased by a factor of  $\gamma$  to increase  $f_\tau$ , the reduction of  $(RC)_{eff.}$  is achieved by keeping  $R_{BB}$  constant. From eq. 2.14,  $R_{BB}$  dominated by the base sheet resistance and contact resistance. As  $T_B$  scales to reduce  $\tau_B$ , the base sheet resistance rises, increasing all terms in  $R_{BB}$ . To compensate the decrease of  $T_B$ , the doping concentration in the base must be increased. Moreover, as  $W_{BM}$  and  $W_E$  are scaled,  $W_{gap}$  and  $W_{B,cont.}$  also decrease. A  $\gamma^2:1$  reduction in  $W_{B,cont.}$  causes  $R_{B,cont.}$  to increase drastically. To prevent  $R_{B,cont.}$  from rising,  $\rho_{B,cont.}$  needs to be reduced (approximately  $\gamma^2:1$ ). This is also achieved by increasing the base doping concentration [12]. A summary of DHBT scaling laws for improving  $f_\tau$  and  $f_{max}$  by a factor of  $\gamma$  is listed in table. 2.1 [2]

## 2.3 DC Current Gain of DHBT

The DC current gain ( $\beta$ ) of a DHBT is defined as  $I_C/I_B$ . Although DC- $\beta$  does not directly affect the cut-off frequencies of a DHBT, when the device is

Parameters		Requirement
Base thickness	$T_B$	Decrease by a factor of $\gamma^{1/2}$
Collector thickness	$T_C$	Decrease by a factor of $\gamma$
B-C mesa width	$W_{BM}$	Decrease by a factor of $\gamma^2$
B-E junction width	$W_E$	Decrease by a factor of $\gamma^2$
Emitter current density	$J_E$	Increase by a factor of $\gamma^2$
Specific emitter contact resistivity	$\rho_{E,cont.}$	Decrease by a factor of $\gamma^2$
Specific base contact resistivity	$\rho_{B,cont.}$	Decrease by a factor $\approx \gamma^2$
Base sheet resistance	$R_{B,sh.}$	Decrease by a factor of $\gamma^{1/2}$

Table 2.1: Scaling laws of DHBTs: the required change for improving  $f_\tau$  and  $f_{max}$  by a factor of  $\gamma$ .

incorporated into circuitry, DC- $\beta$  affects the efficiency and noise figure of a microwave circuit. A low DC- $\beta$  would cause more noise in the RF amplifiers [13] and decreases DC-gain and precision in analog ICs [14, 15]. Therefore, high DC- $\beta$  is desirable for circuit applications.

As dimensions of the devices are scaled to improve the cut-off frequencies, DC- $\beta$  simultaneously reduces. The inverse DC- $\beta$  vs. the B-E junction periphery ( $P_{je} = 2(W_E + L_E)$ ) to area ( $A_{je}$ ) ratio measured from device with different base design is plotted in fig. 2.6. The base designs have doping graded where the highest and lowest doping concentration is at the emitter and collector side, respectively. Design I has a 25 nm thick base with doping varying from 9 to  $5 \times 10^{19} \text{ cm}^{-3}$ . Design II employs a 20 nm thick base with doping varying from 12 to  $8 \times 10^{19} \text{ cm}^{-3}$ . Design III includes a 18 nm thick base with doping varying from 14 to  $9 \times 10^{19} \text{ cm}^{-3}$ . At  $W_E \approx 200 \text{ nm}$ , where  $P_{je}/A_{je} \approx 10 \mu\text{m}^{-1}$ , the DC- $\beta$  is approximately 20. As the device scales to  $W_E = 100 \text{ nm}$ , the DC current gain drops to  $\sim 15$ . Eventually, when the device scales beyond 100 nm  $W_E$ , DC- $\beta$  decreases to less than 10. Thus, it is important to understand and improve DC- $\beta$  in scaled DHBTs.

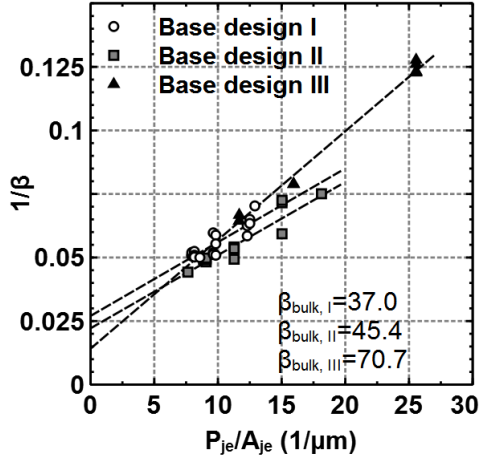


Figure 2.6: Inverse DC current gain ( $1/\beta$ ) vs. HBT emitter periphery to area ratio ( $P_{je}/A_{je} \approx 2/W_E$ ) of experimental DHBTs with distance between base and emitter contacts ( $W_{\text{gap}} \approx 10$  nm and different base designs. The values of  $\beta$  are measured at emitter current density  $J_E \approx 25 \text{ mA}/\mu\text{m}^2$ .

The low DC- $\beta$  is caused by the excessive base current,  $I_B$ . Fig. 2.7 shows the sources of  $I_B$ . Under bias, electrons are injected from the emitter into the base,  $I_E$ . Most injected electrons beneath the base-emitter junction traverse to the collector and become collector current,  $I_C$ . A fraction of the electrons recombine with holes, generating bulk base current,  $I_{B,\text{Bulk}}$ . At the vicinity of emitter edge, a portion of injected electrons diffuse through the bulk base region towards the base contact. They then recombine at the contact, which leads to  $I_{B,\text{diff}}$  (bulk lateral diffusion) [16].

At the p-InGaAs/dielectric interface within the extrinsic base, the surface Fermi level is pinned by donor-like interface trap states, resulting in a surface depletion region and generating the conduction band profile shown in fig. 2.8. After injected into the base, some fraction of electrons will diffuse towards this depletion region, where they will then be trapped by the high field. The trapped

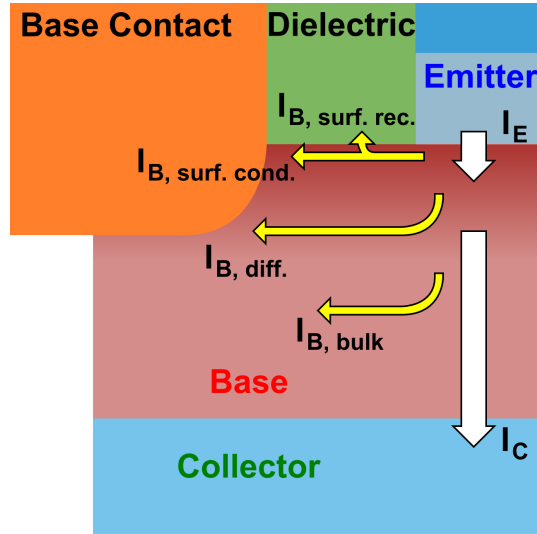


Figure 2.7: A schematic of the current components in the base of DHBTs.

electrons then diffuse laterally towards the base contact. The trapped electrons either recombine *en route* with interface trap states, leading to surface recombination current ( $I_{B,\text{surf. rec.}}$ ), or recombine after reaching the contact, contributing to the surface conduction current ( $I_{B,\text{surf. cond.}}$ ) [17, 18]. The  $I_{B,\text{surf. rec.}}$  and  $I_{B,\text{surf. cond.}}$  will be described in detail in the following context.

### 2.3.1 Bulk Base Current

The bulk base current,  $I_{B,\text{bulk}}$ , was generated as the electrons (injected as  $I_E$ ) recombines with a hole in the bulk base region. Hence,  $I_{B,\text{bulk}}$  scales in proportion to  $A_{je}$ , i.e.  $I_{B,\text{bulk}} = J_{B,\text{bulk}}A_{je}$ , where  $J_{B,\text{bulk}}$  is the current density of the bulk base current.

Several recombination mechanisms in the bulk base region leads to  $I_{B,\text{bulk}}$ . In this work, we considered three recombination mechanisms: Auger recombination, Shockley-Read-Hall (SRH) recombination, and radiative recombination. Accord-

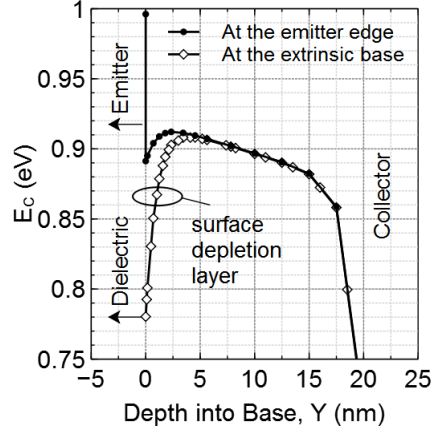


Figure 2.8: Simulated conduction band energy ( $E_C$ ) at  $V_{BE} \approx 1.2$  V vs. depth into the base semiconductor at the edge of the emitter and in the extrinsic base. The simulation assumes a 20 nm thick base with doping varying from  $1.2 \times 10^{20} \text{ cm}^{-3}$  at the emitter side to  $8 \times 10^{19} \text{ cm}^{-3}$  at the collector side [18]. The energy is relative to the base Fermi level.

ing to the Matthiessen's rule, the total electron lifetime ( $\tau_n$ ) due to this three mechanisms can be written as

$$\tau_{n,\text{total}} = \left( \frac{1}{\tau_{\text{Auger}}} + \frac{1}{\tau_{\text{SRH}}} + \frac{1}{\tau_{\text{rad.}}} \right)^{-1}, \quad (2.16)$$

where  $\tau_{\text{Auger}}$ ,  $\tau_{\text{SRH}}$ , and  $\tau_{\text{rad.}}$  are the lifetime of the Auger, SRH, and radiative recombination, respectively. The current gain associated with  $I_{B,\text{bulk}}$ ,  $\beta_{\text{bulk}}$ , is the ratio of the electron lifetime to the base transit time [19], i.e.  $\beta_{\text{bulk}} = \frac{\tau_{n,\text{total}}}{\tau_B}$

The (direct) Auger recombination is a collision process involving four states in the conduction band (CB) and the valance band (VB). There are several variants of Auger recombination. For III-V semiconductors with direct band gap, the process is depicted in Fig. 2.9 [20]. In the CCCH process, two electrons in CB collide, knocking one of them into the valance band and the other one to a

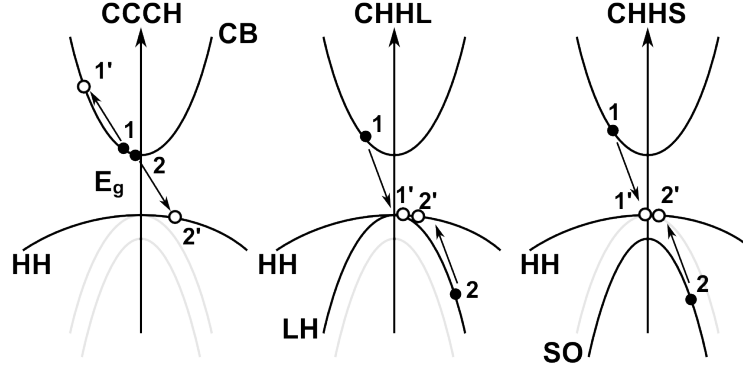


Figure 2.9: Three Auger processes in III-V semiconductors. [20]. The solid circles represent the occupied states, and the empty circles represent the empty states.

more energetic state in CB. The CHHL process involves one hole in the light hole band (LH) and one electron in CB. The CHHS, an analogy to CHHL, involves one hole in the split-off band (SO) and one electron in CB. In addition to the direct Auger processes, a phonon (phonon assisted Auger recombination) or a shallow trap (Auger recombination via shallow traps) could be involved in an indirect Auger process [20]. Nonetheless, the Auger recombination rate estimated from our experimental data includes the contributions from all processes, and isolating the components would be difficult. Hence, in this work, the contribution from the direct and indirect processes were incorporated into the same coefficients.

According to fig. 2.9, the Auger recombination rate depends on the probability of finding the occupied and empty states involved in the transition. The transition probabilities of the three processes are given by [21]

$$\begin{aligned}
 P_{CCCH} &\approx \frac{n^2 p}{N_C^2 N_V} \exp\left(-\frac{\Delta E_1 + \Delta E_2 + \Delta E_{2'}}{kT}\right), \quad (\text{CCCH}) \\
 P_{CCCH} &\approx \frac{n^2 p}{N_C^2 N_V} \exp\left(-\frac{\Delta E_1 + \Delta E_{1'} + \Delta E_{2'}}{kT}\right), \quad (\text{CHHL and CHHS})
 \end{aligned} \tag{2.17}$$

where  $n$  and  $p$  are the electron and hole densities.  $N_C$  and  $N_V$  are the effective densities of states in the conduction band and the valence band.  $\Delta E_i = E_i - E_C$  for states in the conduction band, and  $\Delta E_i = E_V - E_i$  for states in the valence band.

Because of the dependency on the carrier density shown in eq. 2.17, the Auger recombination rate is usually written in the the empirical form:

$$R_{\text{Auger}} = C_{\text{Auger},n}n^2p + C_{\text{Auger},p}np^2, \quad (2.18)$$

where  $C_{\text{Auger},n}$  is the Auger coefficient of the CCCH process and  $C_{\text{Auger},p}$  is the combination of Auger coefficient of the CHHL and the CHHS processes. In the case of DHBTs, the base is heavily doped and only the electrons are injected as minority carriers, i.e.  $p \gg n$ . Therefore, the dominating processes are CHHL and CHHS, and the term involving  $C_{\text{Auger},n}$  can be neglected.

The lifetime associated with the Auger recombination can be written as

$$\tau_{\text{Auger}} = \frac{\delta n}{R_{\text{Auger}}} \approx \frac{1}{C_{\text{Auger},p}p^2}. \quad (2.19)$$

To estimate  $\tau_{\text{Auger}}$ , it is important to obtain an accurate value of  $C_{\text{Auger},p}$ . Various values of  $C_{\text{Auger},n}$  and  $C_{\text{Auger},p}$  have been reported in the literature for InGaAs [22–24]. However, some of the results were measured from p-i-n laser diodes (LDs), in which the electron and hole densities are the same, i.e.  $p = n$ . Hence, the coefficient obtained is in fact  $(C_{\text{Auger},n} + C_{\text{Auger},p})$ , and it is difficult to extract  $C_{\text{Auger},p}$  from it. Combined coefficient  $(C_{\text{Auger},n} + C_{\text{Auger},p})$  of  $9 \times 10^{-29} \text{ cm}^6/\text{s}$  has been reported [24]. Separated coefficients of  $C_{\text{Auger},n} = 5 \times 10^{-30} \text{ cm}^6/\text{s}$  and



$C_{\text{Auger,p}} = 3.6 \times 10^{-29} \text{ cm}^6/\text{s}$  have been measured from n- and p- typed InGaAs, respectively [23].

According to the Shockley-Read-Hall (SRH) statistics [25], the net rate of recombination involving a single state follows the expression of

$$R_{\text{SRH}} = C_{\text{SRH}}(np - n_i^2), \quad (2.20)$$

where  $n_i$  is the intrinsic carrier density.  $C_{\text{SRH}}$  is the SRH recombination coefficient, which is related to the capture cross-sections for electrons ( $\sigma_n$ ) and holes ( $\sigma_p$ ). Because  $\sigma_n$  and  $\sigma_p$  also depends on doping concentration [26], an empirical form is used to approximate the doping-dependent lifetime of SRH recombination. Using Scharfetter relation, with a reference lifetime ( $\tau_{\text{ref}}$ ) drawn from experimental data measured at the doping concentration ( $N_{\text{ref},\tau}$ ), the SRH lifetime can be written as [22, 27]

$$\tau_{\text{SRH}}(N_A + N_D) = \frac{\tau_{\text{ref}}}{1 + \left(\frac{N_A + N_D}{N_{\text{ref},\tau}}\right)^\kappa}, \quad (2.21)$$

where  $N_A$  and  $N_D$  are the acceptor and donor concentrations. The factor  $\kappa$  is obtained from fitting multiple data points at various reference doping concentrations.

The radiative recombination rate follows an expression similar to eq. 2.20, except the coefficient  $C_{\text{SRH}}$  is substituted by  $C_{\text{rad}}$ . Value of  $9.6 \times 10^{-11} \text{ cm}^3/\text{s}$  has been reported for  $C_{\text{rad}}$  in InGaAs [28].

Fig. 2.10 is the computed electron lifetime of different recombination processes in the base of a DHBT. The Auger recombination has the shortest lifetime, and hence is the dominant recombination mechanism in the base of DHBTs. Ac-

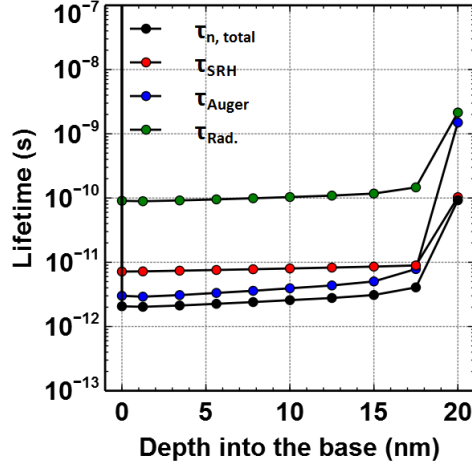


Figure 2.10: Computed electron lifetimes (Auger, SRH, radiative, and total) vs. the depth into the base of a DHBT. A 20 nm thick base with doping varying from  $1.2 \times 10^{20} \text{ cm}^{-3}$  at the emitter side to  $8 \times 10^{19} \text{ cm}^{-3}$  at the collector side was assumed. The emitter current density is assumed to be  $27 \text{ mA}/\mu\text{m}^2$ .

According to the DHBT scaling laws in section 2.6, the doping concentration in the base region must be increased as the devices are being scaled, causing a quadratic decrease in  $\tau_{Auger}$  according to eq. 2.19. Hence, in the future scaling generation DHBTs, a significant portion of base current will be contributed by Auger recombination.

### 2.3.2 Bulk Lateral Diffusion Current

In addition to the quasi-electric field towards the collector, the injected electrons near the edge of the B-E junction experience a lateral driving force towards the base contact induced by the density gradient. As a result, the electrons diffuse in the lateral direction, and a portion of them eventually reach the base contact. They then recombine at the contact, leading to the bulk lateral diffusion

current,  $I_{B,diff}$ . Because the lateral component of the gradient is the strongest in between the B-E junction and the base contact, and is negligible elsewhere (beneath the B-E junction and the base contact),  $I_{B,diff}$  originates near the edge of the B-E junction and terminates at the base contact. Therefore,  $I_{B,diff}$  scales with the junction periphery,  $P_{je}$ , i.e.  $I_{B,diff} = K_{B,diff}P_{je}$ , where  $K_{B,diff}$  is the sheet current density of the bulk lateral diffusion current [16].

Since  $I_{B,diff}$  is competing with the vertical drift-diffusion ( $I_C$ ) for electrons, the magnitude of  $I_{B,diff}$  depends on the gradients in both lateral and vertical directions. As the distance from the B-E junction to the base contact ( $W_{gap}$ ) decreases for DHBT scaling, the lateral component of the density gradient becomes higher; hence  $I_{B,diff}$  increases, reducing DC- $\beta$ .

### 2.3.3 Surface Recombination and Conduction Current

At the interface between p-InGaAs and the dielectric (sidewall or native oxide), donor-like trap states exist. When occupied (capturing a hole), each trap state carries the charge of one hole. The positive charge at the interface pins the surface Fermi level and induces a depletion region [29], resulting in the conduction band profile depicted in fig. 2.8. As the electrons injected from the emitter diffuse laterally into the surface depletion region, they are trapped in the region due to the high field towards the surface. The density of the trapped electron,  $n_s$  depends on  $J_E$  and the field in the surface depletion region. The latter is determined by doping concentration near the base surface, the interface trap states density ( $D_{it}$ ), and the energy of the trap states with respect to the valence band. For InGaAs, the

majority of the traps are located  $\sim 0.5$  eV above the valance band edge [29]. The trap states density,  $D_{it}$ , is affected by bonding configuration at the interface, which depends on the surface treatment and the oxide/nitride formed on the surface [30]. For InGaAs terminated by  $\text{Al}_2\text{O}_3$  deposited by the atomic layer deposition (ALD),  $D_{it}$  ranges from 2.5 to  $5 \times 10^{12}$   $\text{cm}^{-2}\text{eV}^{-1}$  when an adequate surface treatment is performed before ALD [31, 32]. Nonetheless,  $D_{it}$  on the InGaAs base surface of a DHBT could be an order higher than these values because of the process damage to the surface and/or the contamination such as photoresist residues.

After being trapped, the electrons continue to diffuse towards the base contact because of the lateral driving force. A portion of them recombine *en route* with the trap states (surface SRH recombination), generating surface recombination current,  $I_{B,\text{surf.rec.}}$ . Like other recombination current, the magnitude of  $I_{B,\text{surf.rec.}}$  depends on the surface recombination rate of electrons, which is given by

$$R_{\text{surf.SRH}} = n_s(x)v_{\text{surf.rec.}}, \quad (2.22)$$

where  $v_{\text{surf.rec.}}$  is the surface recombination velocity (SRV) of electrons. The value of SRV depends on the interface trap state density,  $D_{it}$ . For the InGaAs surface terminated by native oxide, SRV ranges from  $10^3$  to  $10^4$  cm/s [33].

Because only the electrons near the edge of the B-E junction are trapped and participate in surface recombination [34],  $I_{B,\text{surf.rec.}}$  scales in proportion to  $P_{je}$ , i.e.  $I_{B,\text{surf.rec.}} = K_{B,\text{surf.rec.}}P_{je}$ , where  $K_{B,\text{surf.rec.}}$  is the sheet current density of the surface recombination current.  $K_{B,\text{surf.rec.}}$  can be written as  $K_{B,\text{surf.rec.}} = 2qW_{\text{gap}}R_{\text{surf.SRH}}$ . The factor of 2 accounts for InGaAs surface on both sides of

the emitter stripe. According to the expression,  $I_{B,\text{surf.rec.}}$  decreases when  $W_{\text{gap}}$  reduces as devices are scaled.

The rest of the trapped electrons, if not recombined with surface traps while diffusing towards the base contact, can reach the destination and recombine there, resulting in the surface conduction current [17]. Similar to  $I_{B,\text{surf.rec.}}$ ,  $I_{B,\text{surf.cond.}}$  also scales in proportion to  $P_{\text{je}}$ , i.e.  $I_{B,\text{surf.cond.}} = K_{B,\text{surf.cond.}} P_{\text{je}}$ , where  $K_{B,\text{surf.cond.}}$  is the sheet current density of the surface conduction current. Analogous to the relationship between  $I_{B,\text{bulk}}$  and  $I_C$ ,  $I_{B,\text{surf.rec.}}$  draws trapped electrons from  $I_{B,\text{surf.cond.}}$ . Hence, the ratio of  $I_{B,\text{surf.rec.}}$  to  $I_{B,\text{surf.cond.}}$  depends on the magnitude of the lateral driving force and the SRV.

Both  $K_{B,\text{surf.rec.}}$  and  $K_{B,\text{surf.cond.}}$  are related to  $n_s(x)$ . With a higher  $D_{\text{it}}$ , the surface depletion region becomes wider and more injected electron can be trapped by the surface depletion region. Thus,  $n_s(x)$  becomes larger, and both  $K_{B,\text{surf.rec.}}$  and  $K_{B,\text{surf.cond.}}$  increase, reducing  $\beta$ .

### 2.3.4 DC Current Gain and DHBT Scaling

The total base current in a DHBT is the sum of the four components:

$$\begin{aligned}
 I_B &= I_{B,\text{bulk}} + I_{B,\text{diff.}} + I_{B,\text{surf.rec.}} + I_{B,\text{surf.cond.}} \\
 &= I_{B,\text{bulk}} + I_{B,\text{edge.}} \\
 &= J_{B,\text{bulk}} A_{\text{je}} + (K_{B,\text{diff.}} + K_{B,\text{surf.rec.}} + K_{B,\text{surf.cond.}}) P_{\text{je}} \\
 &= J_{B,\text{bulk}} A_{\text{je}} + K_{B,\text{edge.}} P_{\text{je}} ,
 \end{aligned} \tag{2.23}$$

where  $I_{B,edge.}$  is the total current component originated from the edge of the B-E junction.  $K_{B,edge.}$  is the sheet current density of  $I_{B,edge.}$ . By the definition of  $\beta$  the inverse current gain,  $1/\beta$ , can be written as

$$\begin{aligned}\frac{1}{\beta} &= \frac{1}{\beta_{bulk}} + \frac{K_{B,edge.}P_{je}}{J_C A_{je}} \\ &\approx \frac{1}{\beta_{bulk}} + \frac{K_{B,edge.}}{2J_C W_E},\end{aligned}\tag{2.24}$$

where  $J_C$  here is the collector current density at the base side of the collector. Because most of the current spreading occurs in the bulk collector region,  $J_C$  is associated with  $A_{je}$ . In scaled DHBT  $L_E:W_E > 10$ , and hence the approximation holds.

In the plot of  $1/\beta$  vs.  $P_{je}/A_{je}$  measured from DHBTs, a linear relationship should be observed. The interception is the inverse  $\beta$  of a device with a very wide emitter, from which  $\beta_{bulk}$  can be extrapolated because the edge current component is negligible. The edge sheet current density,  $K_{B,edge.}$ , is obtained from the product of the slope and  $J_C$ . As shown in fig. 2.6, design I, II, and III exhibits  $\beta_{bulk}$  of 37, 45.4, and 70.7, respectively. Assuming  $J_C \approx J_E = 25 \text{ mA}/\mu\text{m}^2$ ,  $K_{B,edge.}$  are 72.5, 71.9, and  $106.9 \mu\text{A}/\mu\text{m}$  for designs I, II, and III.

Two reasons causes the drop of  $\beta$  in a scaled DHBT. First, the increased base doping concentration results in higher Auger recombination rate and hence shorter  $\tau_{Auger}$ . For base designs with the same  $T_B$  and similar  $\tau_B$ ,  $\beta_{bulk}$  decreases as doping concentration increases. Second, the edge current does not vary in proportion with  $W_E$ . For devices with narrow emitters,  $I_{B,edge.}$  will be more dominant with respect to  $I_{B,bulk}$ . Thus, when devices are scaled, the magnitude of edge current

## REFERENCES

---

components remain the same, and  $\beta$  reduces.

In order to improve DC- $\beta$  in the future scaling generations of DHBTs, a model incorporating the contribution from all four base current components would be a valuable design tool in addition to the RF scaling laws of DHBTs. Using a commercial TCAD simulation software, such model can be constructed [16, 18]. The model would enable an estimation of DC- $\beta$  of devices for a given B-E junction design and geometry. Moreover, DC- $\beta$  of device utilizing novel B-E junction geometries such as a recessed B-E junction in a emitter regrowth process can be evaluated as well. The details of TCAD simulation will be covered in chapter 5.

## References

- [1] E. F. Chor, W. K. Chong, and C. H. Heng, "Alternative (Pd,Ti,Au) contacts to (Pt,Ti,Au) contacts for  $\text{In}_{0.53}\text{Ga}_{0.47}\text{As}$ ," *J. Appl. Phys.*, vol. 84, pp. 2977–2979, Sep. 1998.
- [2] M. J. W. Rodwell, M. Le, and B. Brar, "InP Bipolar ICs: Scaling Roadmaps, Frequency Limits, Manufacturable Technologies," *Proc. IEEE*, vol. 92, pp. 271–286, Feb. 2008.
- [3] L. J. Giacoletto, "Diode and Transistor Equivalent Circuits for Transient Operation," *J. Solid-State Circuits*, vol. 4, pp. 80–83, Apr. 1969.
- [4] H. Kroemer, "Two integral relations pertaining to the electron transport through a bipolar transistor with a nonuniform energy gap in the base region," *Solid-state Electron.*, vol. 28, pp. 1101–1103, Nov. 1985.
- [5] S. C. Jain, J. M. McGregor, and D. J. Roulston, "Band-gap narrowing in novel III-V semiconductors," *J. Appl. Phys.*, vol. 68, p. 3747, Oct. 1990.
- [6] T. Ishibash, "Influence of electron velocity overshoot on collector transit times of HBTs," *IEEE Trans. Electron Devices*, vol. 37, pp. 2103–2105, Sep. 1990.

## REFERENCES

---

- [7] “New Semiconductor Materials. Characteristics and Properties,” <http://www.ioffe.ru/SVA/NSM/>.
- [8] Z. Griffith, *Ultra High Speed InGaAs / InP DHBT Devices and Circuits*. Ph.D. Thesis, University of California, Santa Barbara, Santa Barbara, Ca, U.S.A., 2005.
- [9] V. Jain, *InP DHBTs in a Refractory Emitter Process for THz Electronics*. Ph.D. Thesis, University of California, Santa Barbara, Santa Barbara, Ca, U.S.A., 2011.
- [10] Y. Betser and D. Ritter, “Reduction of the base collector capacitance in InP/GaInAs heterojunction bipolar transistors due to electron velocity modulation,” *IEEE Trans. Electron Devices*, vol. 46, pp. 628–633, Apr. 1999.
- [11] M. J. W. Rodwell, M. Urteaga, T. Mathew, D. Scotts, D. Mensa, Q. Lee, J. Guthrie, Y. Betser, S. C. Martin, R. P. Simth, S. Jaganathan, S. Krishnan, S. I. Long, L. Pallela, B. Agarwal, U. Bhattacharya, L. Samoska, and M. Dahlström, “Submicron scaling of HBTs,” *IEEE Trans. Electron Devices*, vol. 48, p. 2606, Nov. 2001.
- [12] A. Baraskar, A. C. Gossard, and M. J. W. Rodwell, “Lower limits to metal-semiconductor contact resistance: Theoretical models and experimental data,” *J. Appl. Phys.*, vol. 114, p. 154516, Oct. 2013.
- [13] M. Rudolph, R. Doerner, L. Klapproth, and P. Heymann, “An HBT noise model valid up to transit frequency,” *IEEE Electron Device Lett.*, vol. 20, pp. 24–26, Jan. 1999.
- [14] S. Tiwari, “Heterostructure bipolar transistors and circuits,” in *IEEE Compound Semiconductor IC Symposium*, Jun. 1988.
- [15] B. Oyama and B. Wong, “GaAs HBT’s for analog circuits,” *Proc. IEEE*, vol. 81, pp. 1744–1761, Dec. 1993.
- [16] H. W. Chiang, J. C. Rode, P. Choudhary, and M. J. W. Rodwell, “Lateral Carrier Diffusion and Current Gain in THz InGaAs/InP DHBTs,” *J. Appl. Phys.*, vol. 115, p. 034513, Jan. 2014.
- [17] C. H. Henry, R. A. Logan, and F. R. Merritt, “The effect of surface recombination on current in  $\text{Al}_x\text{Ga}_{1-x}\text{As}$  heterojunctions,” *J. Appl. Phys.*, vol. 49, pp. 3530–3542, Jan. 1978.



## REFERENCES

---

- [18] H. W. Chiang, J. C. Rode, P. Choudhary, and M. J. W. Rodwell, "Interfacial transport and current gain in InGaAs/InP DHBTs for THz applications," in *72nd IEEE Device Research Conference*, Jun. 2014.
- [19] R. E. Welser, N. Pan, D.-P. Vu, P. J. Zampardi, and B. T. McDermott, "Role of Neutral Base Recombination in High Gain AlGaAs/GaAs HBTs," *IEEE Trans. Electron Devices*, vol. 46, pp. 1599–1607, Aug. 1999.
- [20] N. K. Dutta and R. J. Nelson, "The case for Auger recombination in  $\text{In}_{1-x}\text{Ga}_x\text{As}_y\text{P}_{1-y}$ ," *J. Appl. Phys.*, vol. 53, pp. 74–92, Jan. 1982.
- [21] L. A. Coldren and S. W. Corzine, *Diode Lasers and Photonic Integrated Circuits*. Wiley Series in Microwave and Optical Engineering, 1995.
- [22] V. Palankovski and Q. Rüdiger, *Analysis and Simulation of Heterostructure Devices*. Computational Microelectronics, Wien, New York, Springer, 2004.
- [23] C. H. Henry, R. A. Logan, F. R. Merritt, and C. G. Bethea, "Radiative and nonradiative lifetimes in n-type and p-type  $1.6\ \mu\text{m}$  InGaAs," *Electron. Lett.*, vol. 20, pp. 358–359, Apr. 1984.
- [24] S. Hausser, G. Fuchs, A. Hangleiter, K. Streube, and W. T. Tsang, "Auger recombination in bulk and quantum well InGaAs," *Appl. Phys. Lett.*, vol. 56, pp. 913–915, Mar. 1990.
- [25] W. Shockley and W. T. Read, Jr., "Statistics of the Recombinations of Holes and Electrons," *Physical Review*, vol. 87, pp. 835–841, Sep. 1952.
- [26] R. K. Ahrenkiel, R. Ellingson, S. Johnston, and M. Wanlass, "Recombination lifetime of  $\text{In}_{0.53}\text{Ga}_{0.47}\text{As}$  as a function of doping density," *Appl. Phys. Lett.*, vol. 72, pp. 3470–3472, Jun. 1998.
- [27] S. Datta, K. P. Roenkera, M. M. Cahaya, and W. E. Stanchina, "Implications of hole vs electron transport properties for high speed Pnp heterojunction bipolar transistors," *Solid-state Electron.*, vol. 43, pp. 73–79, Jan. 1999.
- [28] E. Zielinski, H. Schweizer, K. Streubel, H. Eisele, and G. Weimann, "Excitonic transitions and exciton damping processes in InGaAs/InP," *J. Appl. Phys.*, vol. 59, pp. 2196–2204, Mar. 1986.
- [29] H. Hasegawa, "Fermi Level Pinning and Schottky Barrier Height Control at Metal-Semiconductor Interfaces of InP and Related Materials," *Jpn. J. Appl. Phys.*, vol. 38, p. 10981102, Feb. 1999.

## REFERENCES

---

- [30] C. L. Hinkle, M. Milojevic, B. Brennan, A. M. Sonnet, F. S. Aguirre-Tostado, G. J. Hughes, E. M. Vogel, and R. M. Wallace, “Detection of Ga suboxides and their impact on III-V passivation and Fermi-level pinning,” *Appl. Phys. Lett.*, vol. 94, p. 162101, Apr. 2009.
- [31] A. D. Carter, W. J. Mitchell, B. J. Thibeault, J. J. M. Law, and M. J. W. Rodwell, “Al<sub>2</sub>O<sub>3</sub> Growth on (100) In<sub>0.53</sub>Ga<sub>0.47</sub>As Initiated by Cyclic Trimethylaluminum and Hydrogen Plasma Exposures,” *Appl. Phys. Express*, vol. 4, p. 091102, Aug. 2011.
- [32] V. Chobpattana, J. Son, J. J. M. Law, R. Engel-Herbert, C. Y. Huang, and S. Stemmer, “Nitrogen-passivated dielectric/InGaAs interfaces with sub-nm equivalent oxide thickness and low interface trap densities,” *Appl. Phys. Lett.*, vol. 102, pp. 022907–1–022907–3, Jan. 2013.
- [33] E. Yablonovitch and T. J. Gmitter, “A contactless minority lifetime probe of heterostructures, surfaces, interfaces and bulk wafers,” *Solid-state Electron.*, vol. 35, pp. 261–267, Mar. 1992.
- [34] Z. Jin, S. Neumann, W. Prost, and F.-J. Tegude, “Surface Recombination Mechanism in Graded-Base InGaAsInP HBTs,” *IEEE Trans. Electron Devices*, vol. 51, pp. 1044–1045, Jun. 2004.

## Chapter 3

# DHBT Process Improvement

A feasible and reliable process flow is the key to the realization of any semiconductor device. The development of the process flow involves extensive calibrations, testing, and sometimes even the re-definition of the existing process flow. The last one is usually the case when the device dimensions approach the limitation of the existing process flow. As mentioned in chapter 2, device scaling in both epitaxial and lateral directions is necessary in order to attain higher cut-off frequencies. Therefore, developing a DHBT process flow which can be reliably scaled to sub-100 nm emitter width is one of the main goals of this dissertation. In this chapter, the development of both front end and back end process flows will be reported. Three improvements, discussed in designated sections, are ready to be incorporated into the fabrication of DHBTs.

The first improvement involves the recalibration of the process flow for the refractory emitter metal stack. With the new process flow, the emitter width has been successfully and reliably reduced to 75 nm. In the second section, the integration of a new process flow for a composite dielectric sidewall deposited by atomic layer deposition (ALD) and plasma enhanced chemical vapor deposition (PECVD) will be presented. The composite dielectric sidewall deposited immediately after the base metalization protects the extrinsic base from subsequent process damage. With adequate surface pretreatment technique before ALD, the sidewall could decrease the trap states density ( $D_{it}$ ) on InGaAs surface [1, 2], reducing the density of the electrons trapped in the surface depletion region. Thus, the surface conduction via the surface depletion layer decreases and the DC- $\beta$  will be improved [3]. Finally, a new process flow for the interconnects between metal layers at the back end process will be discussed. With the new intercon-

nects, metal to metal spacing has been increased to  $\sim 3\ \mu\text{m}$ . Therefore, low-loss microstrip lines can be built on top of the devices, enabling more accurate RF measurements and device de-embedding.

### 3.1 Refractory Emitter Metal Stack

According to the DHBT scaling law in chapter 2, the emitter current ( $I_E$ ) at the bias point for peak  $f_\tau$  and  $f_{\text{max}}$  must remain constant when the scaled base-emitter (B-E) junction width ( $W_E$ ) decreases in order to reduce the RC delays. As a result, the emitter current density ( $J_E$ ) at such bias point increases when DHBTs are scaled [4]. For DHBTs with 100 nm wide B-E junction and 70 nm thick collector,  $J_E$  for peak  $f_\tau$  and  $f_{\text{max}}$  is approximately  $30\sim 40\ \text{mA}/\mu\text{m}^2$ . At such current density, electron migration would degrade the conventional Ti/Pd/Au contact [5], causing reliability issues in the devices. Therefore, the emitter contact of scaled DHBTs is composed of refractory metal to mitigate the damage due to electron migration [6].

Furthermore, to reduce the base access resistance ( $R_{\text{BB}}$  and RC delay, the base contact of DHBTs needs to be very close to the B-E junction, i.e.  $W_{\text{gap}} \approx 10\text{-}20\ \text{nm}$  in DHBTs with  $\sim 100\ \text{nm}$  emitter width [7]. In addition, the base contact of DHBTs is  $\sim 100\ \text{nm}$ -thick in order to have negligible base metal sheet resistance. To lift-off the base contact, resist must be few hundreds nanometers thick to achieve the required aspect ratio. With such resist thickness, lithography with  $< 10\ \text{nm}$  accuracy in alignment is challenging even with the direct write from a commercial e-beam lithography system [8]. Therefore, the base contact lift-off

has to be a self-aligned process. This is usually achieved by having a tall and narrow emitter metal surrounded by dielectric sidewall. The base metal is then deposited on the emitter metal and the base semiconductor. Because of the high aspect ratio. The emitter and base remain electrically separated, avoiding the shunt path to the B-E junction. For the self-aligned lift-off to work, the sidewall profile of the emitter metal must be nearly vertical [9].

A refractory metal stack with such shape would be difficult to be fabricated using a lift-off process. Moreover, refractory metal need to be evaporated at high power because of its high melting point, increasing the intensity of the bombardment due to X-ray and stray electrons. The e-beam resist could be damaged and the lift-off would fail. Therefore, a process involving blanket metal deposition and dry etch is more suitable for this purpose than the lift-off process. The emitter process flow of UCSB DHBTs has thus been developed based on this process flow [6, 10].

The composite emitter metal stack of UCSB DHBT is composed of three layers: molybdenum, tungsten, and titanium tungsten alloy (TiW). The Mo/W/TiW stack is  $\sim 520$  nm tall and is dry etched by SF<sub>6</sub>/Ar plasma using a chromium hard mask. The Cr reacts in the dry etch chemistry and forms a resistive layer (chromium oxynitride/chromium nitride) which cannot be removed by wet or dry etch techniques without damaging the emitter metal or the substrate. Therefore, a layer of sacrificial dielectric (SiO<sub>2</sub>/SiN<sub>x</sub>) is inserted between Cr and TiW so the Cr mask can be lifted-off by undercutting the oxide with buffered HF (BHF).

Fig. 3.1 and 3.2 are the schematics of UCSB emitter process flow [10]. The fabrication starts with blanket Mo evaporation which forms emitter contact. A

layer of W and a layer of TiW are sputtered on top of Mo. The sacrificial dielectric is then deposited by PECVD. Cr mask is deposited via blanket evaporation, after which the emitter pattern is defined by e-beam lithography and transferred to Cr by  $\text{Cl}_2/\text{O}_2$  inductively coupled plasma (ICP) etch. The dielectric and refractory metal are etched by two consecutive  $\text{SF}_6/\text{Ar}$  inductively coupled plasma (ICP) etch steps. The first etch recipe has high bias power (200 W) in order to remove the dielectric, TiW, W, and Mo. Because the plasma loses its kinetic energy as it travels deeper along the stack, the bottom of the stack is tapered after the first high power etch. To obtain a vertical sidewall profile, a  $\text{SF}_6/\text{Ar}$  etch with low bias power (15 W) is done to undercut the tapered stack, resulting in a metal stack shown in the upper left corner of fig. 3.2.

PECVD  $\text{SiN}_x$  encapsulating the emitter stack is deposited and then etched by  $\text{CF}_4/\text{O}_2$  ICP to form sidewall. The InGaAs emitter cap is wet etched afterwards. Cr mask is lifted-off by undercutting the sacrificial dielectric in BHF, by which the first sidewall is also partially removed. A second layer of  $\text{SiN}_x$  sidewall is thus deposited to provide the electrical separation between the emitter and the self-aligned base contact. Finally, the InP emitter is wet etched prior to the base contact process, as shown in fig. 3.3, in order to have a pristine InGaAs surface for metalization. The details of UCSB DHBT process flow are listed in appendix A.

Since the base contact is self-aligned, base metal is evaporated not only on the base, but also the emitter stack and the sidewall, as illustrated in the right side of fig. 3.3. It is imperative to attain a nearly vertical sidewall profile, i.e. identical width at the top and at the bottom of the metal stack after the metal dry etch.

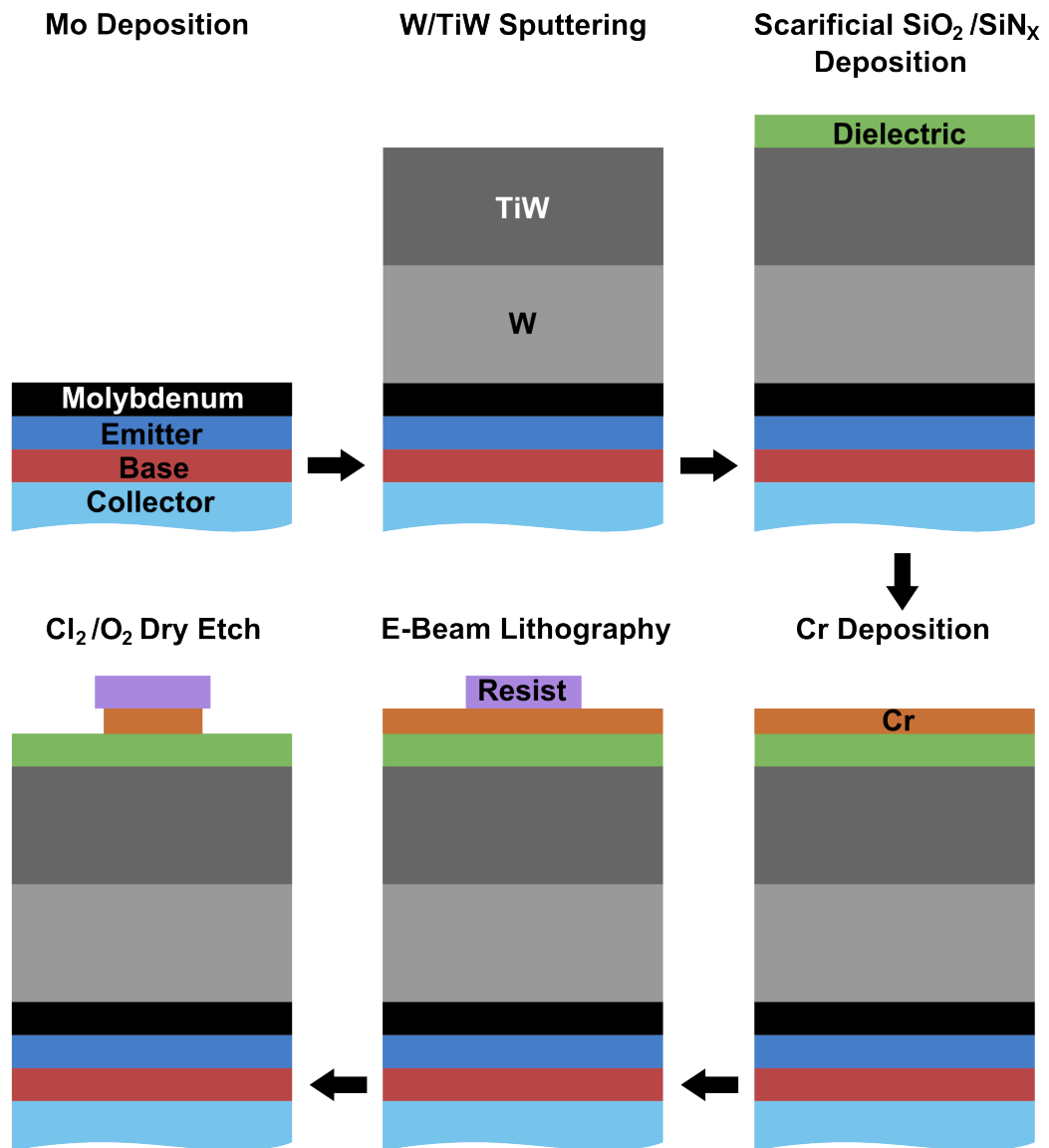


Figure 3.1: The schematics of UCSB DHBT emitter process flow.



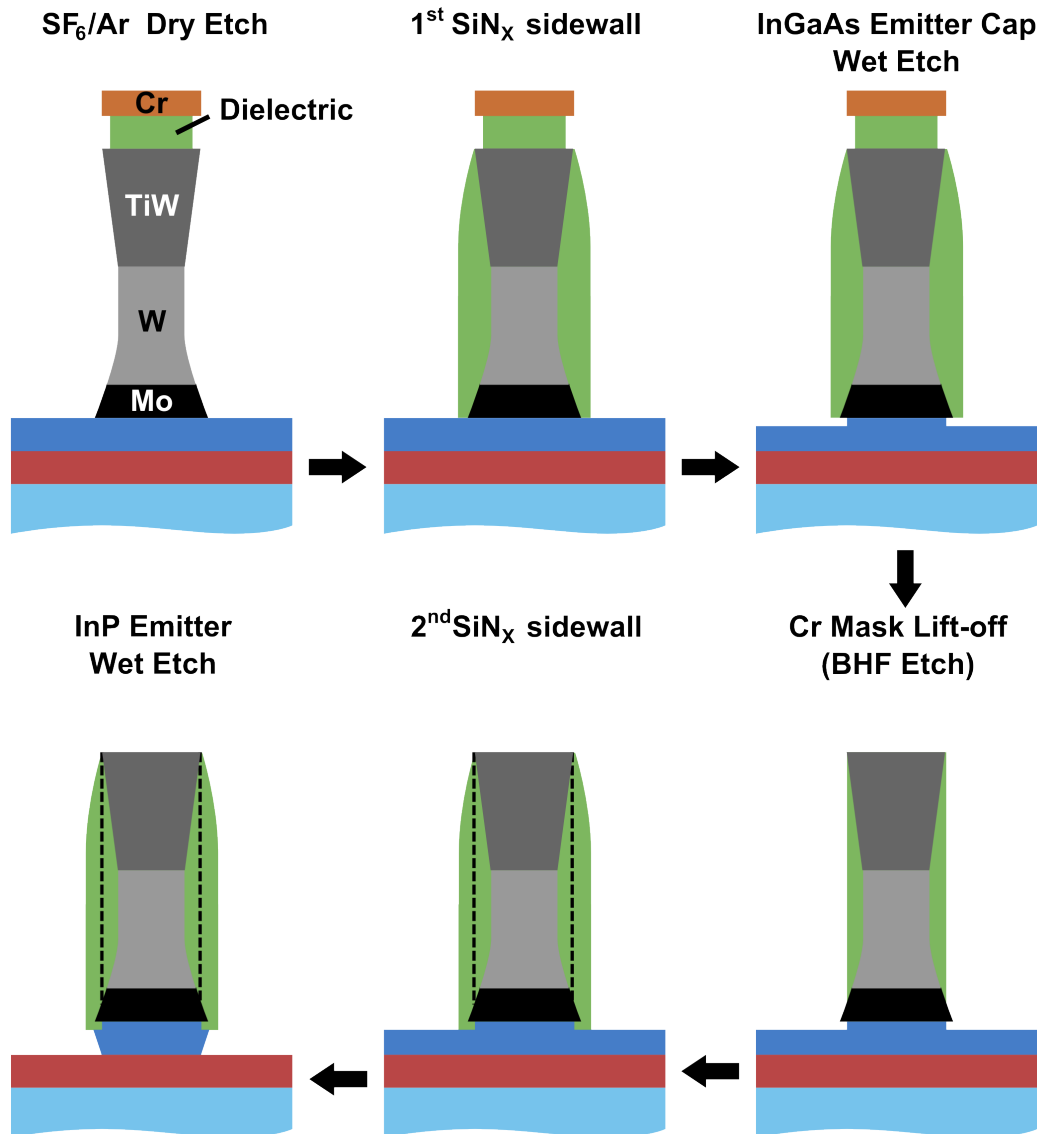


Figure 3.2: The schematics of UCSB DHBT emitter process flow (continued).

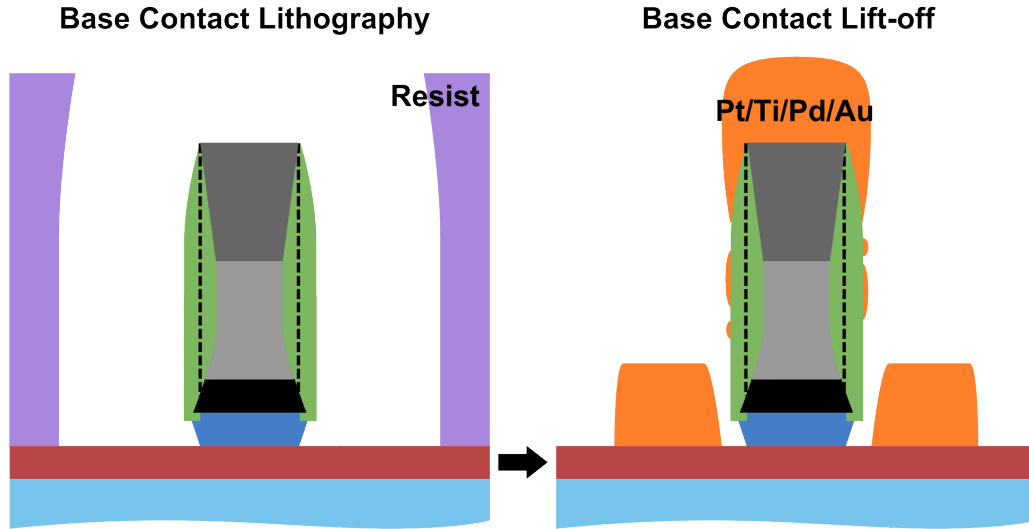


Figure 3.3: The schematics of the self-aligned base contact lift-off process.

As shown in fig. 3.4, if the sidewall profile of the emitter stack is tapered, more metal is evaporated onto the sidewall, potentially forming a shunt path between the base and emitter contacts. At the bottom of the emitter stack, as metal is being deposited on the sidewall, the InGaAs surface within the extrinsic base is sealed, and hence the surface can not be accessed for passivation. On the bare InGaAs surface, Fermi level is pinned by the defect states ( $D_{it}$ ), causing more surface depletion. Therefore, surface conduction base current increases and DC- $\beta$  drops. In an even worse scenario, residues from the resist for the base contact lift-off could be trapped on the extrinsic base surface, further increasing  $D_{it}$  and surface conduction.

Due to its high aspect ratio, the emitter metal stack is sensitive to its internal stress. If the W/TiW film is deposited with high internal compressive or tensile stress, the tall and narrow metal stacks would be mechanically unstable

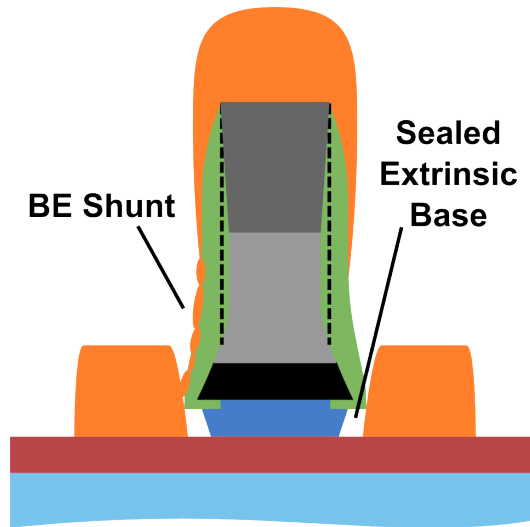


Figure 3.4: The schematics of a base contact lifted-off on a tapered emitter stack. A shunt path between the base and the emitter is formed and the extrinsic base is sealed by the base metal and the dielectric sidewall.

after metal dry etch. If the film is deposited with extremely high internal stress, stress relaxation could occur during the deposition, forming columnar grains [11] which increases the emitter metal resistivity. Thus, prior to the sputtering, the recipe for W/TiW stack must be calibrated to obtain a film with very low internal stress.

The internal stress of W/TiW film depend on the chamber pressure and the temperature on the sample surface. Because of the chamber configuration of the UCSB sputtering system (Sputter 4), the sample temperature is modulated by a radiation heat source located at the back side of the sample holder. Since the sample is heated from behind, temperature gradient exists between the back and front of the sample, and the temperature on the top surface depends on the thickness and the thermal conductance of the sample. Hence, the low stress sputtering recipe was calibrated using InP wafers, whose thickness and thermal properties

are similar to that of the DHBT samples.

As mentioned before, the emitter stack is tapered after the high power SF<sub>6</sub>/Ar ICP etch, and the vertical sidewall profile is achieved by undercutting the stack with a low power SF<sub>6</sub>/Ar ICP etch. The undercut to W is faster than that of TiW because W reacts faster with SF<sub>6</sub>. Therefore, W has a more concave profile than TiW after the dry etch. The process flow developed for DHBTs with 250~200 nm emitter width employs a metal stack with identical W and TiW thickness. Fig. 3.5a is the SEM cross-section of such emitter metal stack. In order to achieve the vertical stack profile, i.e. identical width at the top and the bottom of the stack, the undercut to W ( $W_{UC,W}$ ) is approximately 30 nm on both sides. The bottleneck formed near the W/TiW interface is thus ~60 nm narrower than  $W_E$ , as shown in the top row of fig. 3.6. As shown in the SEM image in fig. 3.5b, the process flow for 1:1 W:TiW can produce a <128 nm wide emitter junction, but at the price of the narrow bottleneck and increased emitter metal resistance. For the DHBT scaling generations beyond 64 nm, the process would fail because of the excessive undercut.

In order to scale the dry etch refractory metal process beyond 128 nm emitter width,  $W_{UC,W}$  must be controlled. As shown in the schematics in bottom row of fig. 3.6, by increasing the TiW to W thickness ratio to 2.5 and recalibrate the low power SF<sub>6</sub>/Ar ICP etch,  $W_{UC,W}$  required for a vertical stack has been reduced to ~10 nm. Fig. 3.7 shows the SEM cross-sections of the 1:2.5 W:TiW stacks at  $W_E=128$  and 64 nm.

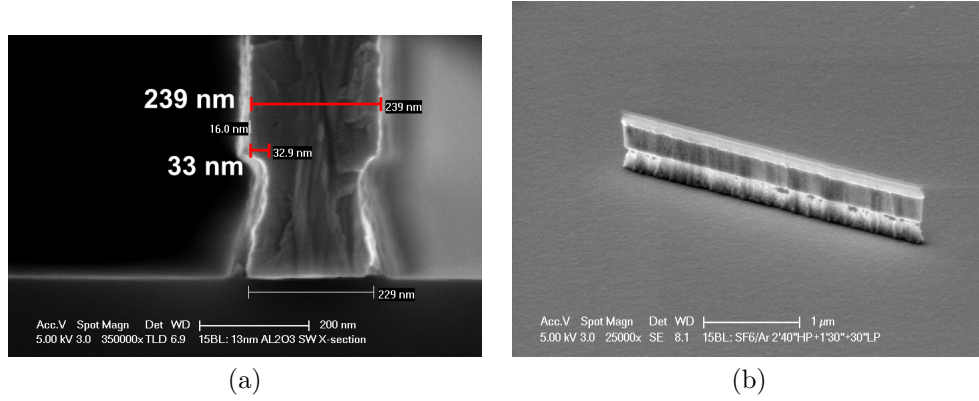


Figure 3.5: SEM of 1:1 W:TiW metal stack on an InP test sample after  $\text{SF}_6/\text{Ar}$  ICP etch. (a) Cross-section of the stack with  $W_E \approx 250$  nm. (b) A stack with  $W_E \approx 75$  nm.

## 3.2 Composite Dielectric Sidewall

The InGaAs surface within the extrinsic base, once exposed after the InP emitter wet etch, is subject to process damage, if not properly sealed after base metalization. Additional surface trap states will be formed if the surface is contaminated by resist residues or damaged by plasma. The increased surface trap density ( $D_{it}$ ) pins the surface Fermi level and induces a wider surface depletion region [12]. Thus, the sheet resistance increases, causing higher  $R_{BB}$ , and hence reduces  $f_{max}$ . Moreover, with higher  $D_{it}$  and wider surface depletion region, more electrons injected from the emitter will be trapped in the surface depletion region. Hence, surface conduction current ( $I_{B,edge}$ ) increases and DC- $\beta$  reduces [3].

For passivating the nano-scaled extrinsic base, a sidewall process is desirable because the field next to the base contact must remain accessible for the subsequent process steps. However, the  $\text{SiN}_x$  sidewall process in the formation of the emitter metal stack is not suitable here due to the plasma damage from PECVD. Furthermore, the PECVD deposition tends to form lips at the top of a step. A

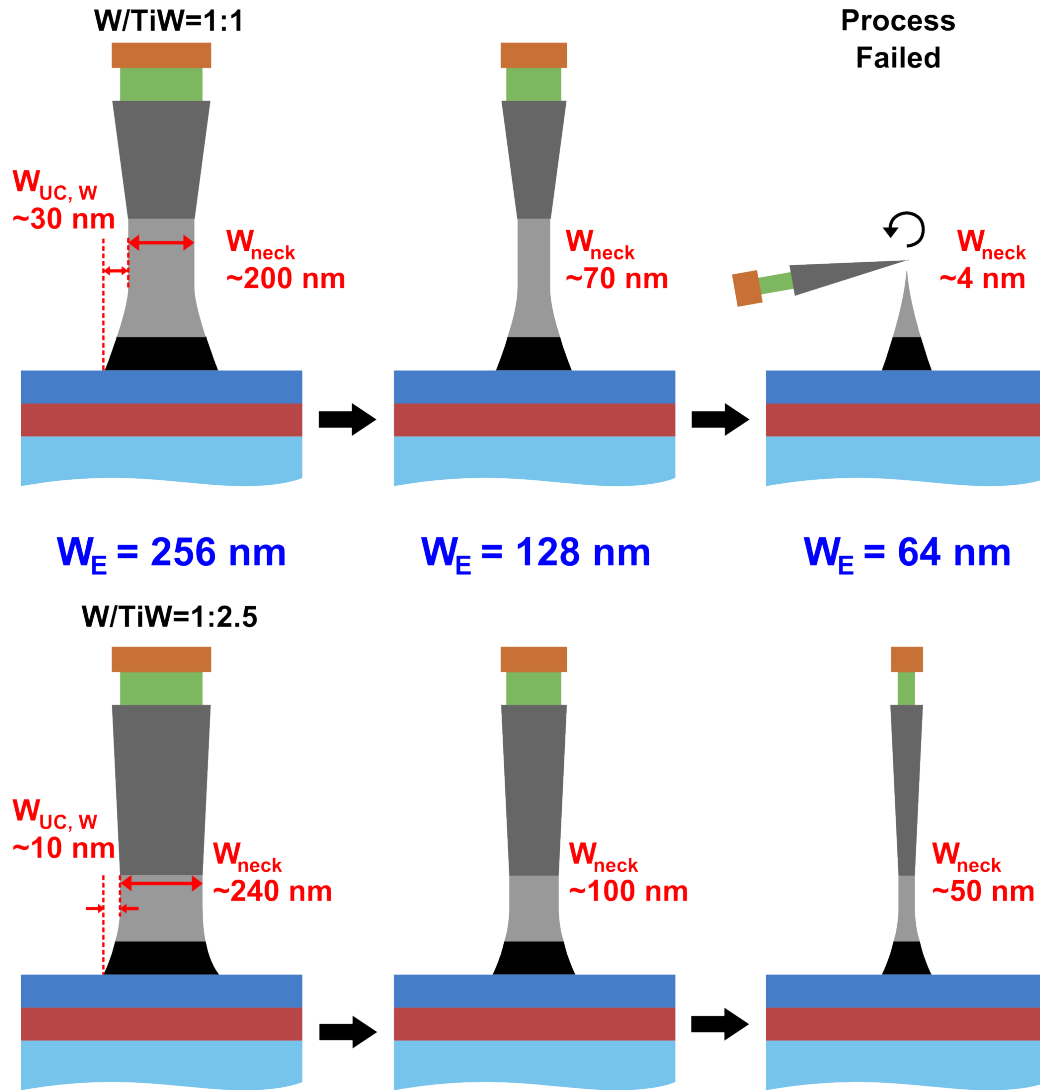


Figure 3.6: Schematics of 256, 128, and 64 nm wide emitter metal stacks after SF<sub>6</sub>/Ar ICP etch. Upper row: 1:1 W:TiW. Bottom row: 1:2.5 W:TiW.

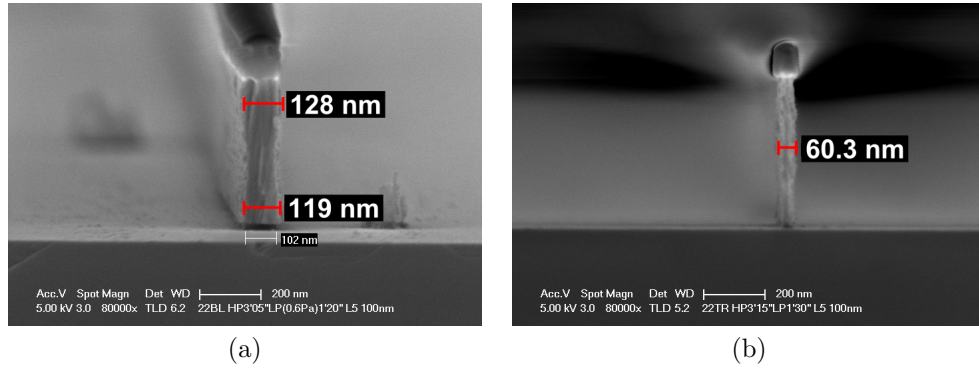


Figure 3.7: SEM cross-sections of 1:2.5 W:TiW metal stack on an InP test sample after recalibrated  $\text{SF}_6/\text{Ar}$  ICP etch. (a)  $W_E=128$  nm. (b)  $W_E=64$  nm.

void could form in a narrow gap because the gap is sealed before it is filled. Because the gap between the base contact and the emitter stack is  $\sim 10$  nm, the gap would be quickly sealed off in  $\text{SiN}_x$  deposition. As a result, the InGaAs surface would not be terminate adequately and  $D_{it}$  will remain high.

On the other hand, ALD, being a self-limiting deposition technique, is capable of filling narrow gaps.  $\text{Al}_2\text{O}_3$  can be deposited without plasma by a thermal ALD at a moderate temperature ( $200^\circ\text{C}$ ) without inducing further base metal penetration/diffusion due to the thermal cycling [13]. However, there is no dry etch process for  $\text{Al}_2\text{O}_3$  compatible with UCSB DHBT process flow.

A hybrid of PECVD  $\text{SiN}_x$  sidewall process and ALD  $\text{Al}_2\text{O}_3$  was thus developed to meet the requirements for the sidewall formation on the extrinsic base. Fig. 3.8 shows the process flow for a composite  $\text{Al}_2\text{O}_3/\text{SiN}_x$  sidewall. After base metalization,  $\text{Al}_2\text{O}_3$  is blanket deposited by thermal ALD.  $\text{SiN}_x$  is deposited by PECVD on top of  $\text{Al}_2\text{O}_3$ , and then dry etched to form sidewall, which is the same sidewall process flow for the emitter stack. Finally,  $\text{Al}_2\text{O}_3$  is wet etched using AZ300MIF developer with the  $\text{SiN}_x$  sidewall being the hardmask. Fig. 3.9a is the

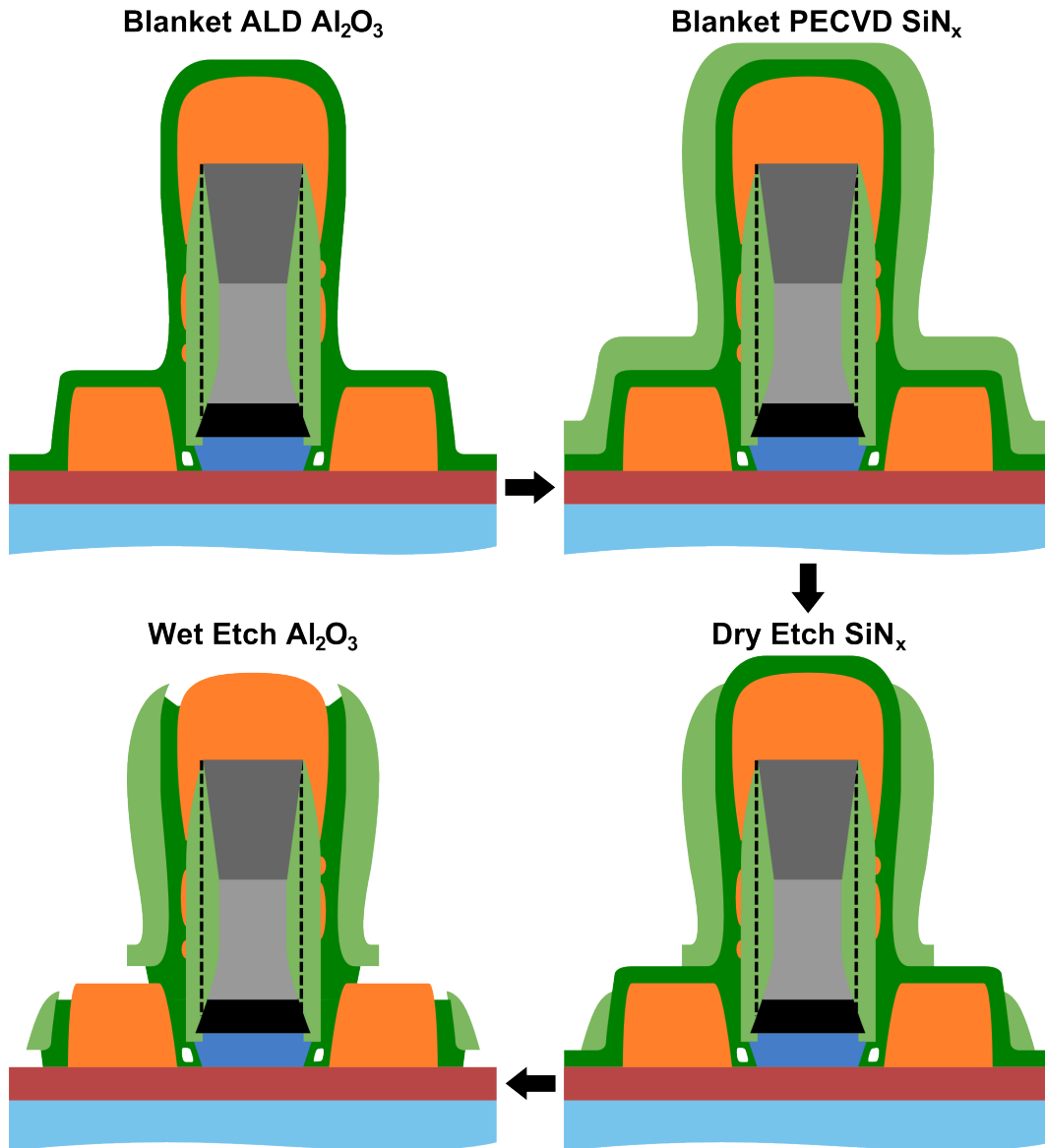


Figure 3.8: Process flow for the composite  $\text{Al}_2\text{O}_3/\text{SiN}_x$  sidewall.



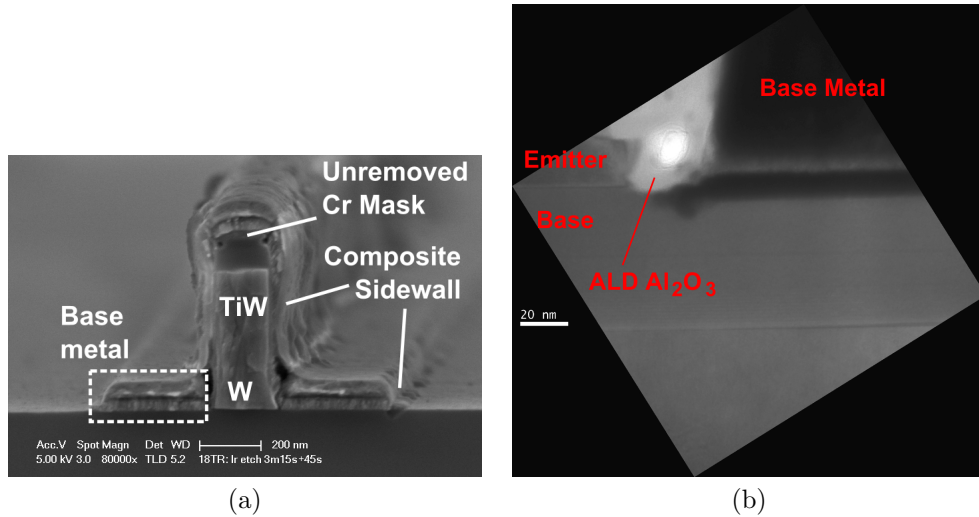


Figure 3.9: (a) SEM cross-section of a InP test sample with the composite sidewall around the emitter stack and the base contact. The bilayer base metal process was also being tested on the sample. (b) TEM cross-section of a experimental device with a composite sidewall sealing the extrinsic base region.

SEM cross-section of a test sample with composite  $\text{Al}_2\text{O}_3/\text{SiN}_x$  sidewall around the emitter and base contact, sealing the extrinsic base surface. The composite sidewall process has been incorporated into the fabrication of DHBT58H and 56K. Fig. 3.9b is the TEM cross-section of the extrinsic base of DHBT70A. The TEM image indicates that ALD  $\text{Al}_2\text{O}_3$  has been deposited onto the extrinsic base.

### 3.3 Interconnects Between Metal Layers

As the cut-off frequencies of the DHBT increase, the frequency range of the measurement should also increase in order to perform a proper extrapolation to estimate the accurate cut-off frequencies. Moreover, in order to improve the accuracy in the RF measurement, it is imperative to not only perform adequate

calibrations prior to the measurements, but also have a clean transmission line environment to probe the device. Several calibration techniques exist for two-port measurements with a network analyzer (PNA). The techniques will be discussed in chapter 4. Coplanar waveguides (CPWs) and microstrip lines are two popular choices for interconnects for RF measurements [14].

CPW is a structure which is relatively easy to fabricate since it is built on a single metal layer. The CPW structure of UCSB DHBT sample are built on the first metal layer (Metal 1) which is  $\sim 1 \mu\text{m}$  above the substrate. A  $50 \Omega$  CPW structure is designed according to the metal thickness ( $1 \mu\text{m}$ ). The length of the CPW line must be negligible when compared to the wavelength of the probing frequencies for device de-embedding purpose. However, the probes should be kept at certain distance to reduce the cross-talk and ensure proper wave propagation [14]. The length of the CPW line on UCSB DHBT samples is thus  $\sim 200 \mu\text{m}$ . As the frequency of a two-port measurement increases, the wavelength decreases and the device de-embedding using the CPW with a fixed length becomes less accurate.

Microstrip line is an alternative structure for RF measurements and is more popular for high frequency measurements. It enables the multilayer thru-reflect-line (ML-TRL) calibration for the vector network analyzers to reduce random errors in the calibrations [15]. However, unlike CPW, since the ground plane and the signal line are at different level, microstrip line requires at least one ground via, which causes excessive inductance at high frequency. Microstrip lines had been incorporated into previous DHBT samples at UCSB by utilizing the sub-collector and Metal 1 as the ground plane and the signal line, respectively. The thickness of the low-k dielectric (BCB) between the sub-collector and Metal 1 is  $< 1 \mu\text{m}$ ,

which is determined by the height of the emitter stack ( $\sim 650$  nm) and the total thickness of the active device ( $\sim 200$  nm). As a result, the width of the microstrip line is few  $\mu\text{m}$ , and a long line may become lossy. In addition, the variation of the BCB thickness across the microstrip line changes the characteristic impedance randomly, causing reflection which decrease the accuracy in device de-embedding.

Increasing the BCB thickness is one solution to this problem. Nevertheless, increasing the distance between the substrate and Metal 1 would be counter productive as it causes unnecessary complexity in the already challenging process flow for the emitter stack. An alternative is to add another BCB ( $\sim 3 \mu\text{m}$ ) and metal layer (Metal 2), and then build the microstrip line using Metal 1 and Metal 2. In order to build such structure, a process flow involving multiple sets of metal lift-off and BCB planarization was developed. However, not only is the process flow time consuming, but it also requires several thermal cycles due to multiple BCB planarization, causing more metal penetration at the contacts.

Therefore, a process flow with one lift-off and BCB process is desirable and has been developed at UCSB. Fig. 3.10 shows the process flow of interconnects between metal layers. On top of the bottom metal layer (Metal 1), a  $\text{SiN}_x$  adhesion layer is sputtered at room temperature instead of PECVD at  $250^\circ\text{C}$  to avoid thermal cycling. Photo-BCB (cyclotene 4024-40), a negative-tone photosensitive BCB resin, is applied on the sample instead of normal BCB resin. After exposure, the photosensitive compound inhibits the dissolution of the BCB resin in the solvent developer so it remains intact. By over exposing the Photo-BCB, a tapered sidewall shape could be created, which is preferable for the subsequent lift-off process. The patterned Photo-BCB resin can then be cured (cross-linked)

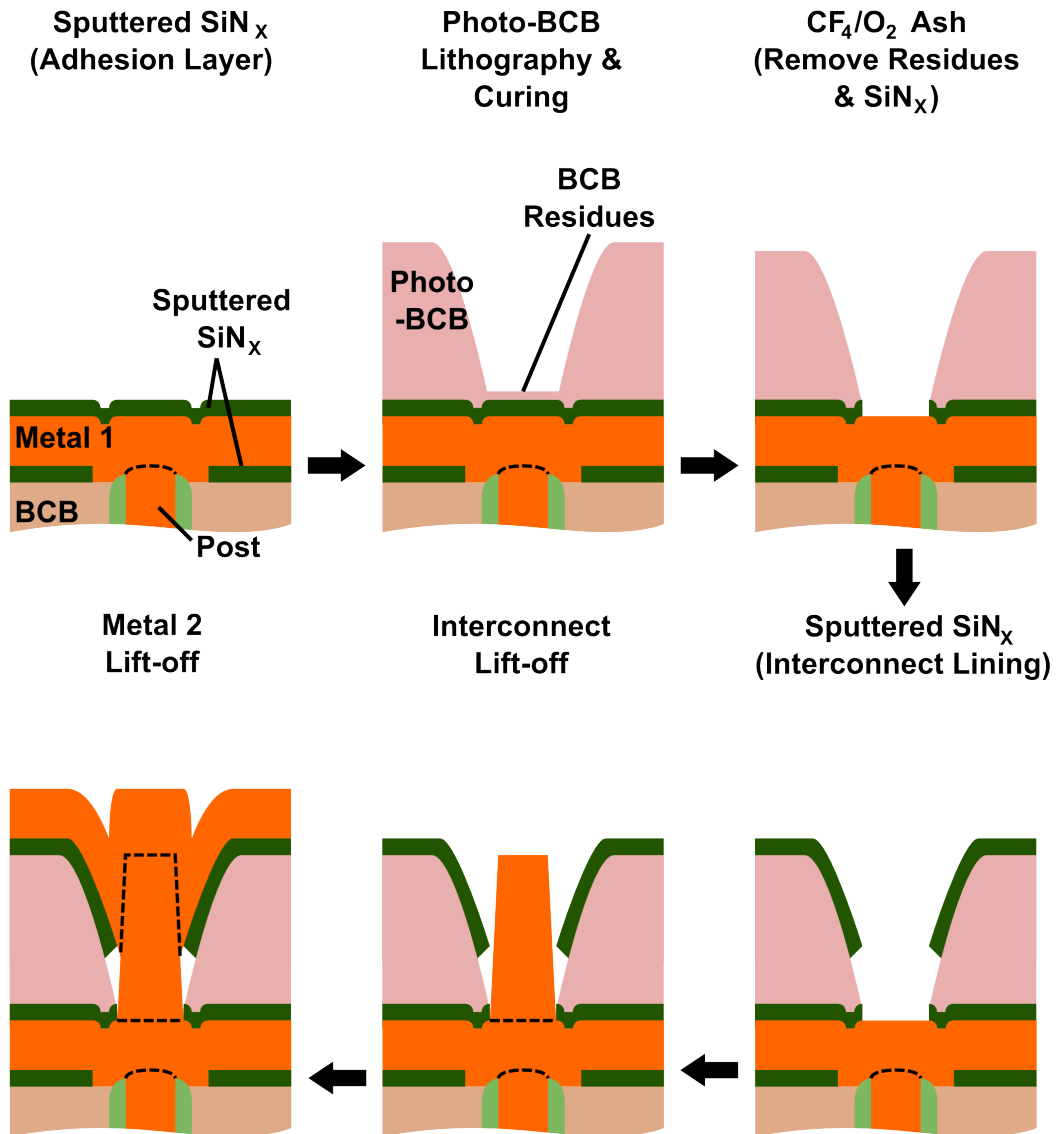


Figure 3.10: Process flow for interconnects between metal layers.

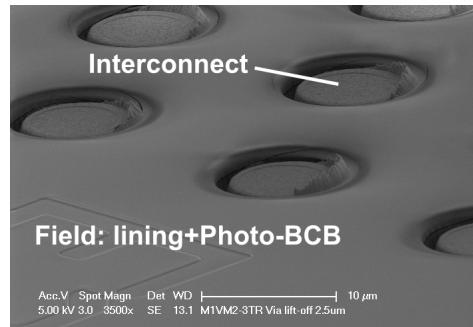


Figure 3.11: SEM of interconnects between metal layers on a test sample.

using the same recipe for normal BCB resin. Because the solvent development leaves residues, the sample is ashed by  $\text{CF}_4/\text{O}_2$  plasma, which will also remove the  $\text{SiN}_x$  adhesion layer within the via. Another layer of  $\text{SiN}_x$  is sputtered, patterned and then etched to form a lining layer to promote the adhesion between metal and Photo-BCB resin. Because of the tapered resin profile, the interconnect metal can be directly lifted-off into the via. Finally, the upper metal layer is lifted-off on the top of the via. The process flow has been demonstrated on test samples, as shown in fig. 3.11, and ready to be integrated into DHBT fabrication.

## References

- [1] A. D. Carter, W. J. Mitchell, B. J. Thibeault, J. J. M. Law, and M. J. W. Rodwell, "Al<sub>2</sub>O<sub>3</sub> Growth on (100) In<sub>0.53</sub>Ga<sub>0.47</sub>As Initiated by Cyclic Trimethylaluminum and Hydrogen Plasma Exposures," *Appl. Phys. Express*, vol. 4, p. 091102, Aug. 2011.
- [2] V. Chobpattana, J. Son, J. J. M. Law, R. Engel-Herbert, C. Y. Huang, and S. Stemmer, "Nitrogen-passivated dielectric/InGaAs interfaces with sub-nm equivalent oxide thickness and low interface trap densities," *Appl. Phys. Lett.*, vol. 102, pp. 022907–1–022907–3, Jan. 2013.
- [3] H. W. Chiang, J. C. Rode, P. Choudhary, and M. J. W. Rodwell, "Interfacial transport and current gain in InGaAs/InP DHBTs for THz applications," in *72nd IEEE Device Research Conference*, Jun. 2014.
- [4] M. J. W. Rodwell, M. Le, and B. Brar, "InP Bipolar ICs: Scaling Roadmaps, Frequency Limits, Manufacturable Technologies," *Proc. IEEE*, vol. 92, pp. 271–286, Feb. 2008.
- [5] S. Krumbein, "Metallic electromigration phenomena," *IEEE Trans. Compon., Hybrids, Manuf. Technol.*, vol. 11, pp. 5–15, Mar. 1988.
- [6] E. Lind, A. M. Crook, Z. Griffith, M. J. W. Rodwell, X.-M. Fang, D. Loubychev, Y. Wu, J. M. Fastenau, and W. Liu, "560 GHz  $f_{\tau}$ ,  $f_{\max}$  InGaAs/InP DHBT in a novel dry-etched emitter process," in *65th IEEE Device Research Conference*, Jun. 2007.
- [7] V. Jain, J. C. Rode, H. W. Chiang, A. Baraskar, E. Lobisser, B. J. Thibeault, M. J. W. Rodwell, M. Urteaga, D. Loubychev, A. Snyder, Y. Wu, J. M. Fastenau, and W. Liu, "1.0 THz  $f_{\max}$  InP DHBTs in a refractory emitter and self-aligned base process for reduced base access resistance," in *69th IEEE Device Research Conference*, Jun. 2011.
- [8] E. Lobisser, J. C. Rode, V. Jain, H. Chiang, A. Baraskar, W. J. Mitchell, B. J. Thibeault, and M. J. W. Rodwell, "InGaAs/InP DHBTs with Emitter and Base Defined through Electron-Beam Lithography for Reduced  $C_{cb}$  and Increased RF Cut-off Frequency," in *39th International Symposium on Compound Semiconductors*, Aug. 2012.
- [9] V. Jain, (*InP DHBTs in a Refractory Emitter Process for THz Electronics*. PhD thesis.

## REFERENCES

---

- [10] V. Jain, E. Lobisser, A. Baraskar, B. J. , Thibeault, M. J. W. Rodwell, Z. Griffith, M. Urteaga, D. Loubychev, A. Snyder, Y. Wu, J. M. Fastenau, and W. K. Liu, “InGaAs/InP DHBTs in a Dry-Etched Refractory Metal Emitter Process Demonstrating Simultaneous  $f\tau/f_{\max} \sim 430/800$  GHz,” *IEEE Electron Device Lett.*, vol. 32, pp. 24–26, Jan. 2011.
- [11] J. Singh and D. E. Wolfe, “Review Nano and macro-structured component fabrication by electron beam-physical vapor deposition (EB-PVD),” *J. Mater. Sci.*, vol. 40, pp. 1–26, Jan. 2005.
- [12] H. Hasegawa, “Fermi Level Pinning and Schottky Barrier Height Control at Metal-Semiconductor Interfaces of InP and Related Materials,” *Jpn. J. Appl. Phys.*, vol. 38, p. 10981102, Feb. 1999.
- [13] E. F. Chor, W. K. Chong, and C. H. Heng, “Alternative (Pd,Ti,Au) contacts to (Pt,Ti,Au) contacts for  $\text{In}_{0.53}\text{Ga}_{0.47}\text{As}$ ,” *J. Appl. Phys.*, vol. 84, pp. 2977–2979, Sep. 1998.
- [14] S. A. Wartenberg, *RF Measurements of Die and Packages*. Artech House, 2002.
- [15] R. B. Marks, “A multiline method of network analyzer calibration,” *IEEE Trans. Microw. Theory Techn.*, vol. 39, no. 7, 1991.

# Chapter 4

## Experimental Results



In this chapter, the DC and RF output characteristic of the DHBT samples, fabricated using the process flow in Appendix A, on two different epitaxial designs and with different process features will be reported. To achieve the highest possible cut-off frequencies ( $f_\tau, f_{\max}$ ), the parasitic RC delays, which are determined by the physical dimensions of the devices as well as the specific contact resistivity ( $\rho_{\text{Cont.}}$ ) at each terminals, need to be as low as possible. Since the device dimensions and  $\rho_{\text{Cont.}}$  are process-dependent, the optimal dimensions remain unknown until the sample is probed. To ensure the presence of the device with the optimized dimension, an array of devices with different combinations of  $W_E$ ,  $W_{\text{BM}}$ , and  $L_E$  were fabricated simultaneously on every DHBT sample.

DC characteristics were measured using Agilent 4155C semiconductor parameter analyzer. For RF measurements, the transistors were DC-biased using 4155C, and the two-port S-parameters were measured by Agilent E8361A network analyzer (PNA) at frequencies between 0.5 and 67 GHz. Using Agilent Advance Design System (ADS), the data were de-embedded. The results were then fitted with an hybrid- $\pi$  equivalent circuit model, and thereby the parasitic resistance and capacitance of the devices were extracted.

## 4.1 Measurement set up and calibration

The  $f_\tau$  and  $f_{\max}$  of scaled DHBTs are few hundreds GHz, which exceeds the frequency span of most commercially available vector network analyzers (VNAs). Therefore RF measurements were performed at K or W band, and the cut-off

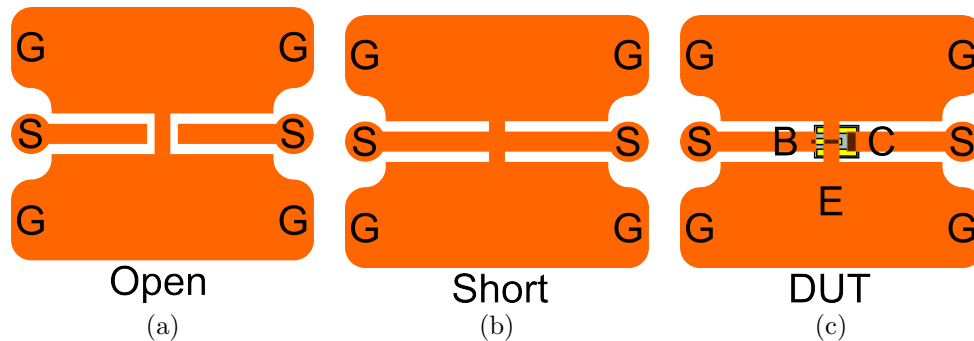


Figure 4.1: Top-down schematics of (a) open and (b) short calibration structures, and (c) CPW interconnect with device under test (DUT).

frequencies were then extrapolated from data measured at these bands. Accurate extrapolation requires clean RF data, and hence adequate microwave environment is crucial. CPW structures with  $50\ \Omega$  characteristic impedance were constructed on Metal 1 for each device. Moreover, measurement performed with on-wafer probes is necessary for both precision and repeatability purposes. Metal pads capable of accommodating a  $75\ \mu\text{m}$ -pitch ground-signal-ground (GSG) on-wafer probe were incorporated into the CPW structures. To remove the parasitics associated with the CPW interconnect and de-embed the device, on-wafer open and short CPW standards were also fabricated simultaneously [1]. Fig.4.1 shows the schematics of the CPW interconnects for open and short calibration and device under test (DUT).

The on-wafer probes and the PNA terminals were connected by semi-rigid waveguides, which has a delay term associated with it. To compensate this delay and shift the reference plane from the PNA terminals to the on-wafer probe tips, calibration using either an on-wafer or an off-wafer impedance standard was performed before device measurement. There are several calibration techniques: Short-Open-Line-Thru (SOLT), Line-Reflect-Reflect-Match (LRRM), and Thru-

Reflect-Line (TRL), etc [1]. For the SOLT technique, the accuracy of the calibration depends on whether the connection to the standards is in consistency with the connection when the equivalent circuit of the standards are determined by the manufacturer [2]. Therefore, SOLT is generally suitable for coaxial measurements but undesirable for probe measurements, where the variation induced by probe positioning exists. The LRRM technique, on the other hand, requires a fully known thru standard which defines the probe tips as the reference planes, two non-deal reflection standards with different reflection coefficients (short and open of SOLT), and finally a match standard, where only the DC resistance needs to be known [3]. Thus, compared with SOLT, LRRM is less prone to the error due to probing variation [1]. For the work in this thesis, LRRM calibration was performed prior to the RF measurements using a commercially available impedance standard for 75  $\mu\text{m}$ -pitch GSG probes.

The parasitic associated with the CPW interconnect must be de-embedded so the temporal response of the transistor can be obtained. After the LRRM calibration, the two-port S-parameters of open and short structures shown in Fig. 4.1 were measured and translated into Y-parameters ( $Y_{\text{open}}$  and  $Y_{\text{short}}$ ). The raw S-parameters of the DUT were then measured and translated to Y-parameter as well ( $Y_{\text{DUT}}$ ). The actual Y-parameters of the transistor ( $Y_{\text{HBT}}$ ) can be obtained from the following expression

$$Y_{\text{HBT}} = ((Y_{\text{DUT}} - Y_{\text{open}})^{-1} - (Y_{\text{DUT}} - Y_{\text{short}})^{-1})^{-1}. \quad (4.1)$$

The above equation is valid when the physical dimensions of the CPW is much smaller than the propagation wavelength at the probing frequency (few mm

at 0.5 67 GHz) [4]. However, if the distance between two on-wafer probe is too small, crosstalk or coupling between the probes can reduce the accuracy of the measurements. Therefore, the physical dimensions of the CPW cannot be scaled infinitely. The length of the CPW structures on UCSB HBT samples is  $\sim 200 \mu\text{m}$ .

Fig. 4.2 is the circuit diagram of the measurement set up. The semi-rigid waveguides connecting the on-wafer probes and PNA are omitted because the delay associated with them has been removed after LRRM calibration. DUTs were DC-biased using 4155C via the internal bias tees of the PNA. Due to the small physical dimensions of THz HBTs, the base-emitter junction is extremely sensitive to the amount of base current and can easily breakdown at  $I_B$  of few mA. Since  $I_B$  varies exponentially with  $V_{BE}$ , an abrupt change in  $V_{BE}$  will induce high  $I_B$ , and could possibly lead to device failure. In order to avoid device failure, a resistor ( $R_{\text{Bias}}$ ) was added as a voltage divider between the base terminal and 4155C. The actual  $V_{BE}$  at DUT is then  $V_{BE} = V_{BB} - I_B R_{\text{Bias}}$ . With  $R_{\text{Bias}} = 10 \text{ k}\Omega$ , the  $I_B R_{\text{Bias}}$  drop is 1 V every  $100 \mu\text{A}$ , which mitigate the change in  $V_{BE}$  as we adjust  $V_{BE}$  for desired  $I_B$  and  $I_E$ .

## 4.2 DHBT63B

### 4.2.1 Device structure and process feature

The DHBT63 design utilizes a 30 nm thick InP emitter doped at  $5 \times 10^{19} \text{ cm}^{-3}$  for the top 15 nm and  $3 \times 10^{18} \text{ cm}^{-3}$  for the bottom 15 nm. The p-type base is composed of 25 nm of InGaAs with a doping-grade from  $9 \times 10^{19} \text{ cm}^{-3}$  at

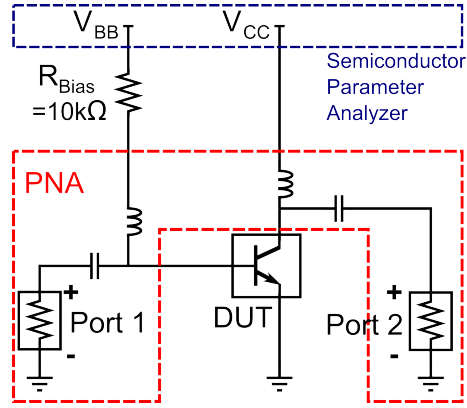


Figure 4.2: RF measurement set up. The delay associated with semi-rigid waveguides were removed after calibration. Hence the waveguides are neglected in the diagram.

the emitter side to  $5 \times 10^{19} \text{ cm}^{-3}$  at the collector side. The design employs the 70 nm thick collector structure (setback, superlattice, InP collector) with doping concentration of  $1 \times 10^{17} \text{ cm}^{-3}$ . The detailed epitaxial structure is listed in table 4.1. The band diagram of the device under  $V_{BE}=1.2 \text{ V}$  and  $V_{CB}=0.6 \text{ V}$  is shown in fig. 4.3. The solid lines are the conduction band and the valance band if the space charge associated with the collector current in the collector region is neglected, whereas the dashed lines are the bands considering the space charge in the collector at  $J_C \approx 31 \text{ mA}/\mu\text{m}^2$ .

The base metalization of DHBT63B was a lift-off process using UV-6 as the resist. According to the HBT samples fabricated prior to DHBT63B, UV-6, being both an UV and e-beam resists, is sensitive to bombardment from X-ray and stray electrons during e-beam evaporation. When damaged, the resist may form residues at the vicinity of the base contact define by lithography, as shown in Fig. 4.4. The residues alter the surface reconstruction on p-InGaAs, increasing the specific contact resistivity [5]. In a worse case, it could results in a failed lift-off

Layer	Semiconductor	Thickness (Å)	Doping ( $\text{cm}^{-3}$ )
Emitter cap	$\text{In}_{0.53}\text{Ga}_{0.47}\text{As}$	100	$8 \times 10^{19}:\text{Si}$
Emitter	InP	150	$5 \times 10^{19}:\text{Si}$
Emitter	InP	150	$3 \times 10^{18}:\text{Si}$
Base	$\text{In}_{0.53}\text{Ga}_{0.47}\text{As}$	250	$9 - 5 \times 10^{19}:\text{C}$
Setback	$\text{In}_{0.53}\text{Ga}_{0.47}\text{As}$	95	$1 \times 10^{17}:\text{Si}$
B-C grade	-	120	$1 \times 10^{17}:\text{Si}$
$\delta$ -doping	InP	30	$5 \times 10^{18}:\text{Si}$
Collector	InP	455	$1 \times 10^{17}:\text{Si}$
Sub-collector	InP	75	$2 \times 10^{19}:\text{Si}$
Sub-collector	$\text{In}_{0.53}\text{Ga}_{0.47}\text{As}$	75	$4 \times 10^{19}:\text{Si}$
Sub-collector	InP	3000	$1 \times 10^{19}:\text{Si}$
Etch stop	$\text{In}_{0.53}\text{Ga}_{0.47}\text{As}$	35	undoped
Substrate	InP	-	undoped

Table 4.1: Epitaxial structure of DHBT63.

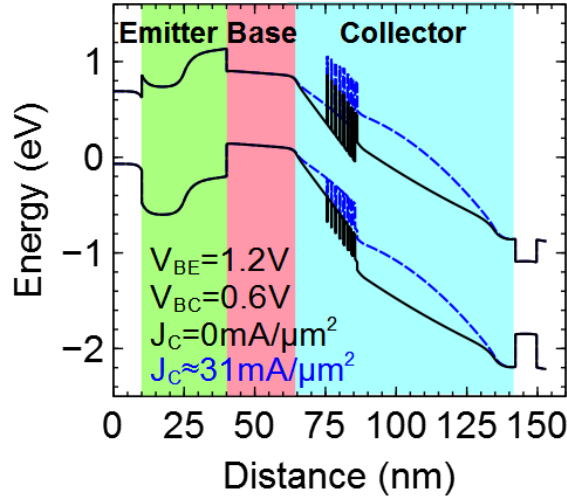


Figure 4.3: Computed band diagram of DHBT63 under  $V_{BE}=1.2 \text{ V}$  and  $V_{CB} = 0.6 \text{ V}$ . The solid lines are the conduction and valance bands when  $J_C = 0 \text{ mA}/\mu\text{m}^2$ , i.e. ignoring the space charge in the collector region. The dashed line represent the conduction and valance bands considering the space charge region in the collector at  $J_C \approx 31 \text{ mA}/\mu\text{m}^2$ .

process. The metalization process involving UCSB e-beam evaporation system (E-Beam 4) had been suffered from this damage due to excessive X-ray irradiation and electrons bombardment. The cause of this was later identified as a Nickel

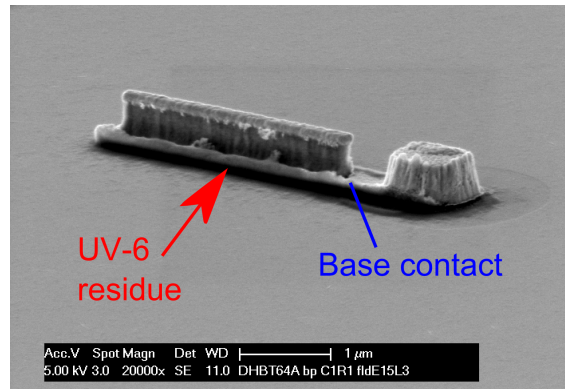


Figure 4.4: An SEM image of an HBT sample after base post lift-off. Residues of UV-6 were found around the base contact, possibly due to the damaged resist sidewall.

metal source in the evaporator, which would disrupt the magnetic field near the electron filament, generating the excessive X-ray and stray electrons. By removing the Ni source from the chamber, the damage to UV-6 has been alleviated. However, this discovery was made after the fabrication of DHBT63B is completed. To avoid the lift-off failure as well as high specific contact resistivity, a portion of the base metallization of DHBT63B was done using the e-beam evaporation system in the cleanroom at Teledyne Scientific Corporation (TSC).

The base contact of DHBT63B is composed of 3.5/17/17/70 nm of Pt/Ti/Pd/Au. After e-beam lithography, 3.5 nm of Pt was deposited using E-Beam 4. The sample was then sealed in a nitrogen ambient environment and transferred to the e-beam evaporation system at TSC, where the subsequent Ti/Pd/Au deposition was done. The sample was then transferred back to UCSB in a nitrogen ambient environment for the lift-off process.

### 4.2.2 TEM analysis

In order to analyze the electrical data, it is imperative to know the physical dimensions of the device. Transmission electron microscopy (TEM) cross-section of the devices is a suitable mean of obtaining the exact dimensions because of its magnification power and resolution. TEM *lamellae* were sliced from DHBT samples and polished using dual beam focused ion-beam/SEM (FEI Helios Nanolab 600i). The bright-field TEM images of the *lamellae* were obtained using FEI Tecnai G2 TEM.

Fig.4.5a is the TEM cross-section normal to the emitter stripe of the device with  $W_{E,\text{design}}=100$  nm,  $W_{BM,\text{design}}=500$  nm defined by e-beam lithography. The composite refractory metal stack above the Mo emitter contact consists of  $\sim 250$  nm of W and  $\sim 250$  nm of TiW. Due to the dry etch profile of W/TiW stack and the thickness of dual dielectric sidewalls (20 nm each), the base-emitter junction is 70 nm wider than the design, i.e.  $W_{E,\text{actual}}=170$  nm for  $W_{E,\text{design}}=100$  nm. According to TEM,  $W_{\text{gap}}=10\sim 20$  nm, and the undercut to the base-collector mesa ( $W_{\text{undercut}}$ ) is  $50\sim 75$  nm on both sides of the mesa. The average width of the base contact on each side of the emitter for the device with  $W_{E,\text{design}}=100$  nm and  $W_{BM,\text{design}}=500$  nm is then:

$$\begin{aligned} W_{B,\text{Cont.}} &= (W_{BM,\text{design}} - W_{E,\text{actual}} - 2 \times (W_{\text{gap}} + W_{\text{undercut}}))/2 \\ &= (500 - 170 - 2 \times (15 + 62.5))/2 = 87.5 \text{ nm.} \end{aligned}$$

Fig. 4.5b is the TEM cross-section of the same device as Fig. 4.5a under higher magnification power zoomed in at the vicinity of the emitter and the base contact. As shown in the TEM cross-section, 1.2 nm of InGaAs was removed from the surface of the base semiconductor, presumably due to the diluted HCl etch



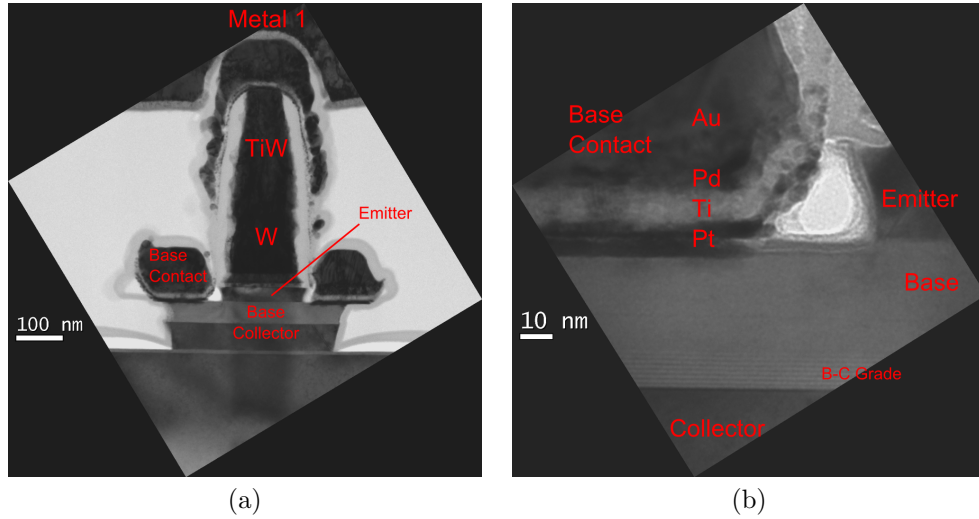


Figure 4.5: TEM cross-section normal to the emitter stripe of a device on DHBT63B with  $W_{E,\text{design}}=100$  nm,  $W_{\text{BM},\text{design}}=500$  nm. (a) An overview of the device. (b) zoomed in at the vicinity of the base contact and emitter.

prior to the Pt deposition. Also shown in the TEM, the base metal penetrates the InGaAs base for 4 nm, which is caused by the reaction between Pt and As atoms [6]. As a result, the base contact is located at  $\sim 5$  nm below the base-emitter junction.

Fig. 4.6 is the TEM cross-section parallel to the emitter stripe of another device with  $L_{E,\text{design}}=3$   $\mu\text{m}$  zoomed in at the vicinity of the base post. The undercut to both sides of the InP emitter semiconductor stripe is  $\sim 150$  nm. Thus, the actual length of the emitter stripe ( $L_{E,\text{actual}}$ ) is 300 nm shorter than the design length ( $L_{E,\text{design}}$ ). The base-collector mesa beneath the base post pedestal was intentionally exposed and undercut ( $\sim 200$  nm) during the device isolation wet etch to reduce  $C_{\text{CB}}$  and increase  $f_{\text{max}}$ .

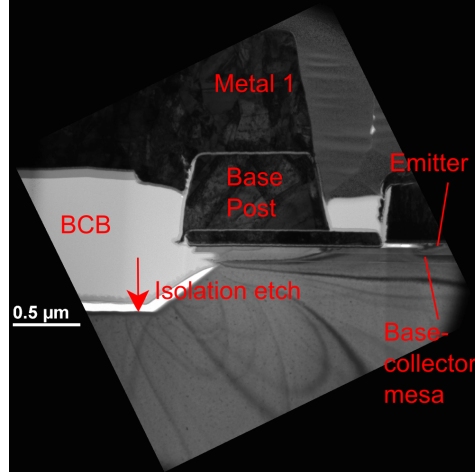


Figure 4.6: TEM cross-section parallel to the emitter stripe of a device on DHBT63B with  $L_{E,\text{design}}=3\ \mu\text{m}$ . The image is zoomed in at the vicinity of the base post.

### 4.2.3 TLM results

The pinched and unpinched base TLM results of DHBT63B are shown in fig. 4.7a and fig. 4.7b. The values of the base sheet resistance obtained from the pinched TLM and the unpinched TLM are  $811\ \Omega/\square$  and  $1211\ \Omega/\square$ , respectively. The pinched TLM result agrees with the TLM result measured by IQE ( $768\sim 792\ \Omega/\square$ ) on the DHBT63 wafer with the InGaAs surface terminated by the InP emitter layer. The specific base contact resistivity extrapolated from the pinched TLM results is  $10.5\ \Omega-\mu\text{m}^2$ , which is more than twice the value required ( $4\ \Omega-\mu\text{m}^2$ ) to achieve  $1\ \text{THz}\ f_{\text{max}}$  at  $W_E=100\ \text{nm}$ . The high specific contact resistivity could be the result of UV-6 residues during the Pt deposition and/or contamination during sample transportation between TSC and UCSB. A more thorough analysis on the base contact resistivity will be addressed in the later section along with the base contact resistance extracted from the RF measurements. Fig. 4.8 is the collector TLM result of DHBT63B. The collector sheet resistance and specific

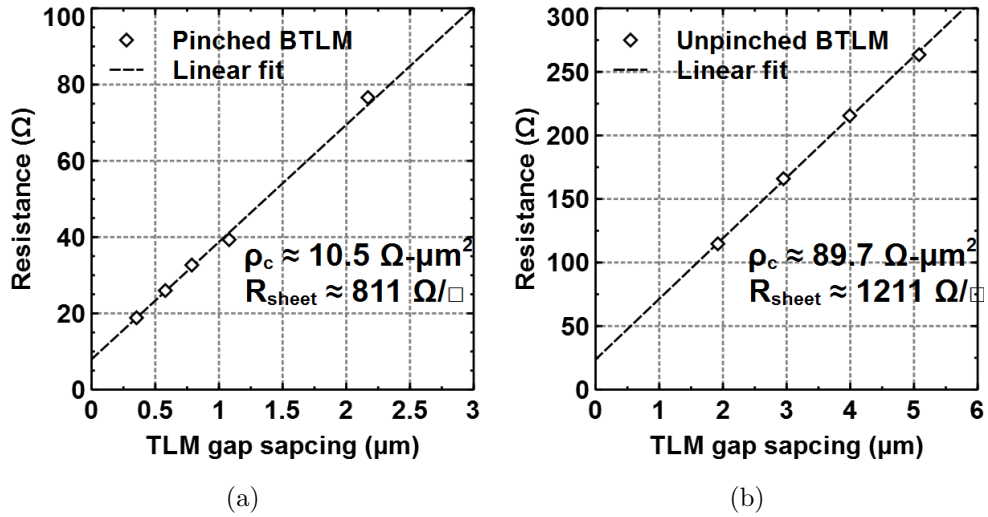


Figure 4.7: (a) Pinched and (b) Unpinched base TLM data of DHBT63B. The width of TLM structure and the distances between metal pads (gap spacing) were measured with SEM.

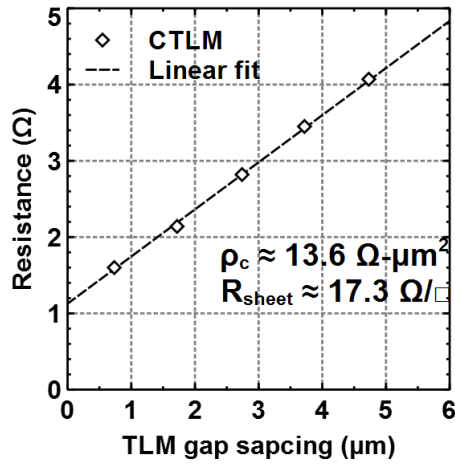


Figure 4.8: Collector TLM result of DHBT63B. The width of TLM structure and the distances between metal pads (gap spacing) were measured with SEM.

contact resistivity are  $17.3 \Omega/\square$  and  $13.6 \Omega - \mu\text{m}^2$ , respectively.

#### 4.2.4 Transistor DC characteristics

For the epitaxial design of DHBT63, the maximum emitter current density limited by the Kirk effect ( $J_{C,Kirk}$ ) at  $v_{CB}=0.6$  V is approximately  $34\text{-mA}/\mu\text{m}^2$ . The actual limit could be  $\sim 20\%$  higher if the current spreading effect in the collector region is included. However, most of the devices on DHBT63B could not reach this limit and the base-emitter junction failed at  $J_E=30\sim 35\text{ mA}/\mu\text{m}^2$ . Therefore, no Kirk effect was observed from both DC and RF measurement. According to the TEM in fig. 4.5b, the distance the base metal and the sharp corner on the top of the emitter semiconductor is less than 10 nm. Hence, the failure mode of the B-E junction is possibly caused by the dielectric breakdown through the  $\text{SiN}_x$  sidewall between the base metal and the sharp corner on the top of the emitter. The DC measurements preceded the RF measurements. To avoid the failure of the B-E junction before the subsequent RF measurement, current and power compliance was set for the emitter terminal according to the emitter width of the DUT during every DC measurement. In addition, the sweeping range for  $V_{BE}$  was limited from 0 to 1 V in the measurement for diode I-V characteristics (Gummel plots).

Fig. 4.9a is the common emitter output characteristic of a device with  $W_{E,design}=100$  nm,  $W_{BM,design}=500$  nm, and  $L_{E,design}=3\ \mu\text{m}$ , i.e.  $W_{E,actual}=170$  nm,  $W_{B,Cont.}=87.5$  nm, and  $L_{E,actual}=2.7\ \mu\text{m}$ . The base current varies from 0 to  $200\ \mu\text{A}$  with a step of  $20\ \mu\text{A}$ . The Gummel plot of the same device at  $V_{CB}=0$  V is shown in fig. 4.9b. At  $V_{BE}=1$  V, the emitter current density and the DC current gain ( $\beta$ ) are approximately  $32.5\text{ mA}/\mu\text{m}^2$  and 22, respectively. The base-emitter (B-E) and the base-collector (B-C) diode ideality factors,  $\eta_B$  and  $\eta_C$ , extrapolated from the data within  $V_{BE}=0.7$  to  $0.9$  V are 2.49 and 1.66, respectively. Because the B-E

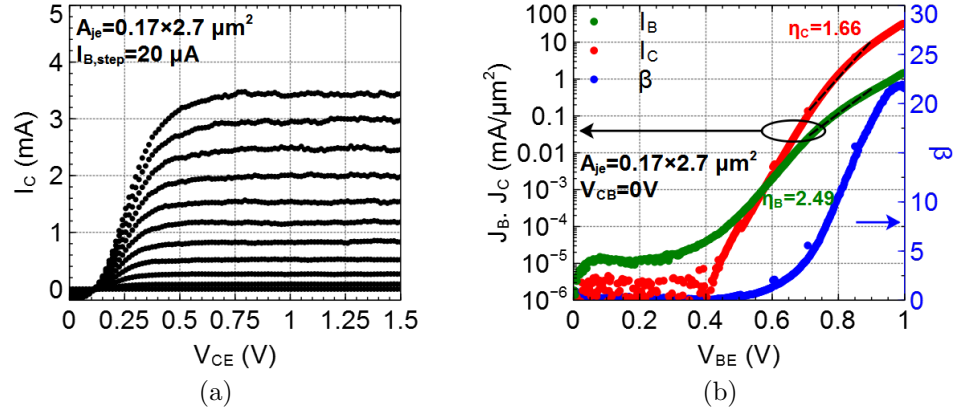


Figure 4.9: DC characteristics of the device with  $W_{E,design} = 100$  nm,  $W_{BM,design} = 500$  nm, and  $L_{E,design} = 3 \mu m$ . (a) Common emitter output characteristics. The increment of the base current ( $I_{B,step}$ ) is  $20 \mu A$ . (b) I-V characteristics of B-E and B-C diodes (Gummel plot).

diode is an abrupt junction, when increasing  $V_{BE}$  by an amount of  $\delta V_{BE}$  the barrier height for electron injection into the base is changed by  $\delta V_{BE} - \delta V_{BE,p}$ , where the drop  $\delta V_{BE,p}$  is due to the modulation of the electrostatic potential in the base region [7]. Therefore, more  $\delta V_{BE}$  is required to increase  $I_E$  to a given magnitude, and hence the ideality factor becomes higher.

Because of the improvement in both the composite emitter stack and the back end process flow, the transistor yield on DHBT63B has been greatly improved. Approximately 80 to 90% of the devices probed demonstrated DC characteristics previously shown. With the sufficient transistor yield, the dependence of DC- $\beta$  on device dimensions could be analyzed. For a proper comparison, the DC- $\beta$  of the devices are sampled at  $V_{CB} = 0V$  and  $J_E \approx 25$  mA/ $\mu m^2$ , which is below  $J_{C,Kirk}$  and close to  $J_E$  for peak  $f_\tau$  and  $f_{max}$ . Inverse DC- $\beta$  vs. base-emitter junction periphery to area ratio ( $P_{je}/A_{je}$ ) of the devices on DHBT63B is plotted in fig. 4.10. According to the extrapolation, the DC- $\beta$  ( $\beta_{Bulk}$ ) of a device with a very

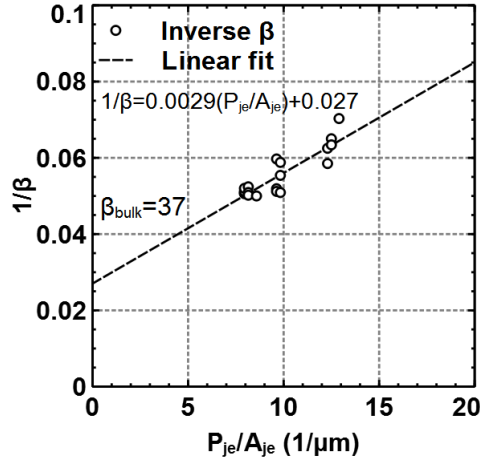


Figure 4.10: Inverse DC- $\beta$  vs. base-emitter junction periphery to area ratio ( $P_{je}/A_{je}$ ) of the devices on DHBT63B.

wide emitter, i.e.  $P_{je}/A_{je} \rightarrow 0$ , is  $\sim 37$ , and the sheet current density of the base edge current ( $K_{B,edge}$ ) is  $72.5 \text{ mA}/\mu\text{m}$ . At  $W_E=150 \text{ nm}$ , DC- $\beta \approx 15$ , which implies that approximately 29% of  $I_B$  is due to the edge current.

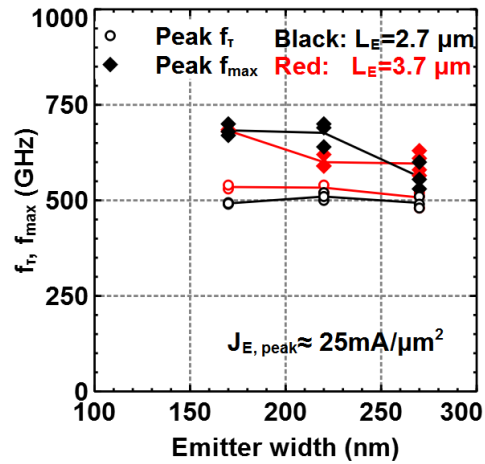
#### 4.2.5 RF performance

For a device on DHBT63 with the assumed parameters listed in table. 4.2, the calculated  $f_\tau$  and  $f_{max}$  are approximately 600 and 1100 GHz, respectively. However, the highest  $f_\tau/f_{max}$  measured on DHBT63B is approximately 500/700 GHz, obtained from a device with  $W_{E,actual}=220 \text{ nm}$ ,  $W_{B,Cont.}=187.5 \text{ nm}$ ,  $L_{E,actual}=2.7 \mu\text{m}$ . Fig. 4.11 is a summary of the peak cut-off frequencies measured on DHBT63B. The peak current gain cut-off frequency varies from 490 to 550 GHz, and the peak power gain cut-off frequency lies within 530 and 700 GHz.

A possible reason for the discrepancies between the calculated and measured

Parameters		Value	Unit
Emitter width	$W_E$	100	nm
Emitter length	$L_E$	3	$\mu\text{m}$
B-E spacing	$W_{\text{gap}}$	15	nm
Base contact width (single side)	$W_{\text{B,Cont.}}$	100	nm
Excessive base post area	$A_{\text{BP}}$	0.8	$\mu\text{m}^2$
Emitter contact resistivity	$\rho_{\text{E,cont.}}$	4	$\Omega - \mu\text{m}^2$
Base contact resistivity	$\rho_{\text{B,cont.}}$	4	$\Omega - \mu\text{m}^2$
Base sheet resistance	$R_{\text{sheet,B}}$	820	$\Omega/\square$
$e^-$ diffusivity in the base	$D_{\text{n,B}}$	40	$\text{cm}^2/\text{s}$
$e^-$ velocity in the collector	$v_{\text{C}}$	$3.2 \times 10^7$	$\text{cm}/\text{s}$
Emitter current density	$J_{\text{E}}$	36	$\text{mA}/\mu\text{m}^2$
B-E diode ideality factor	$\eta_{\text{B}}$	2	

Table 4.2: Parameters assumed in the cut-off frequencies calculation of DHBT63.

Figure 4.11: Peak  $f_{\tau}$  and  $f_{\text{max}}$  vs. base-emitter junction width of the devices with emitter length ( $L_E$ ) of 2.7 and 3.7  $\mu\text{m}$  on DHBT63B.

$f_\tau/f_{\max}$  is the low emitter current density. The optimal bias condition for peak  $f_\tau/f_{\max}$  of a DHBT is when  $r_e$  and  $C_{CB}$  are both near their minima, which usually lies within the vicinity of the onset of Kirk effect. As mentioned previously, the base-emitter junctions of DHBT63B could not sustain the current density limited by the Kirk effect, i.e. the diode failed before reaching  $J_{C,KirK}$ . Therefore, no Kirk effect nor the peaking of  $f_\tau/f_{\max}$  has been observed. Another cause of low  $f_{\max}$  is high base specific contact resistivity, which increases the RC delay in the base-collector mesa.

In this section, the RF measurement results of two devices on DHBT63B are selected and reported as examples for the probed devices. In order to understand measured RF performance, the base access resistances and the base-collector capacitances extracted from small-signal equivalent circuit model of each probed devices are analyzed.

The first device has  $W_{E,\text{design}}=150$  nm,  $W_{BM,\text{design}}=750$  nm, and  $L_{E,\text{design}}=3$   $\mu\text{m}$ . According to the TEM analysis, the area of the base-emitter junction ( $A_{je}$ ) is  $\sim 0.22 \times 2.7$   $\mu\text{m}$ , and the average width of the base contact on both sides of the emitter ( $W_{B,\text{Cont.}}$ ) is  $\sim 187.5$  nm. Fig. 4.12a shows the unilateral Mason's gain (U) and current gain ( $H_{21}$ ) vs. frequency at  $J_E=29$  mA/ $\mu\text{m}^2$ ,  $I_B=900$   $\mu\text{A}$ , and  $V_{CE}=1.5$  V. Under this bias condition, the device exhibits  $f_\tau/f_{\max} \approx 509/702$  GHz according to the single-pole fit (dashed lines). Fig. 4.12b is the Smith chart showing the de-embedded two-port S-parameters of this device from 0.1 to 67 GHz. Using ADS, a small-signal equivalent circuit model based on the hybrid- $\pi$  model is simulated and fit to the experimental data. The dashed lines in fig. 4.12b are the ADS simulation results. The small-signal equivalent circuit model used in



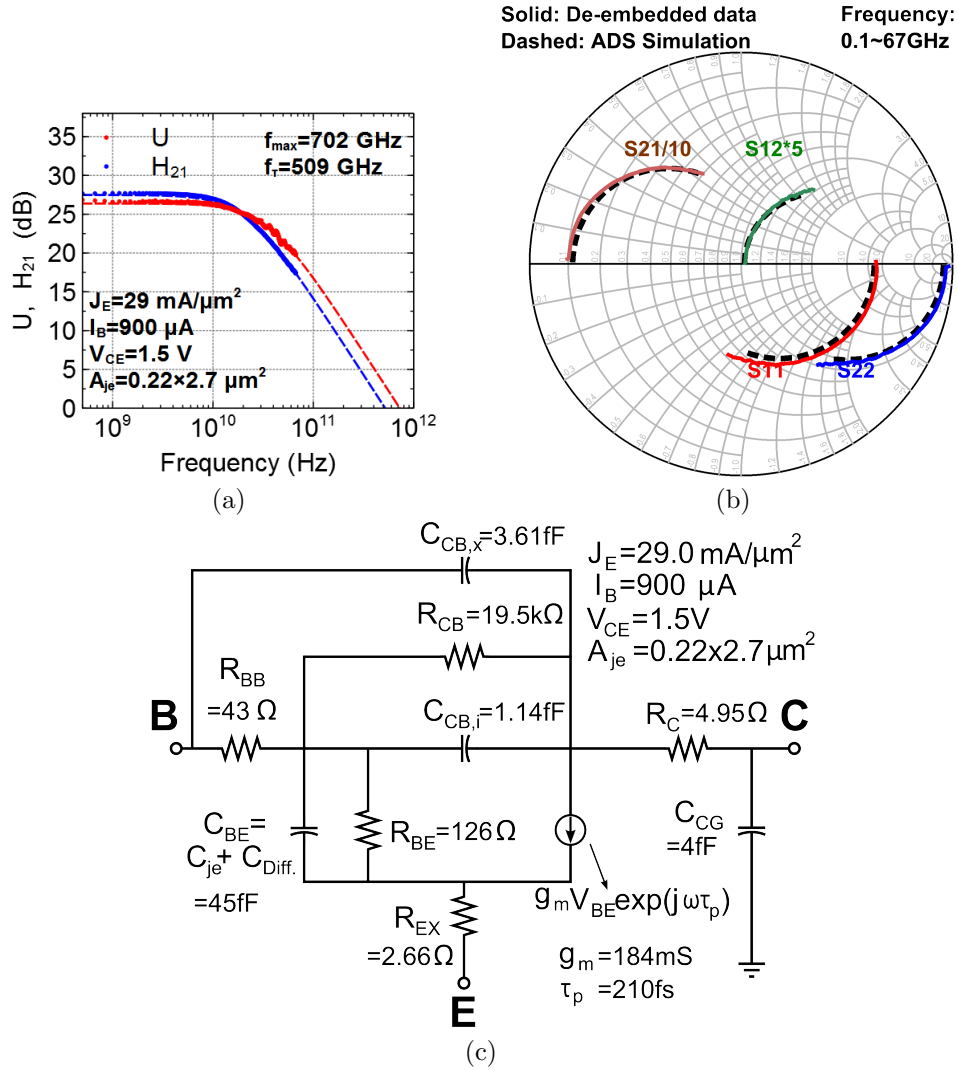


Figure 4.12: RF measurement results of a device DHBT63B with  $W_{E,\text{design}} = 150$  nm,  $W_{BM,\text{design}} = 750$  nm, and  $L_{E,\text{design}} = 3$   $\mu\text{m}$ : (a) unilateral Mason's gain and  $H_{21}$  vs. frequency, (b) Two-port S-parameters vs. frequency, and (c) small-signal equivalent circuit. In both (a) and (b), the solid lines represent the experimental data, and the dashed lines are the ADS simulation results.

ADS simulation is shown in fig. 4.12c.

As mentioned in chapter 2, when  $J_E < J_{C,\text{Kirk}}$ ,  $C_{CB}$  decreases as the current density increases due to velocity modulation [Ritter99TED]. When  $J_E > J_{C,\text{Kirk}}$ ,

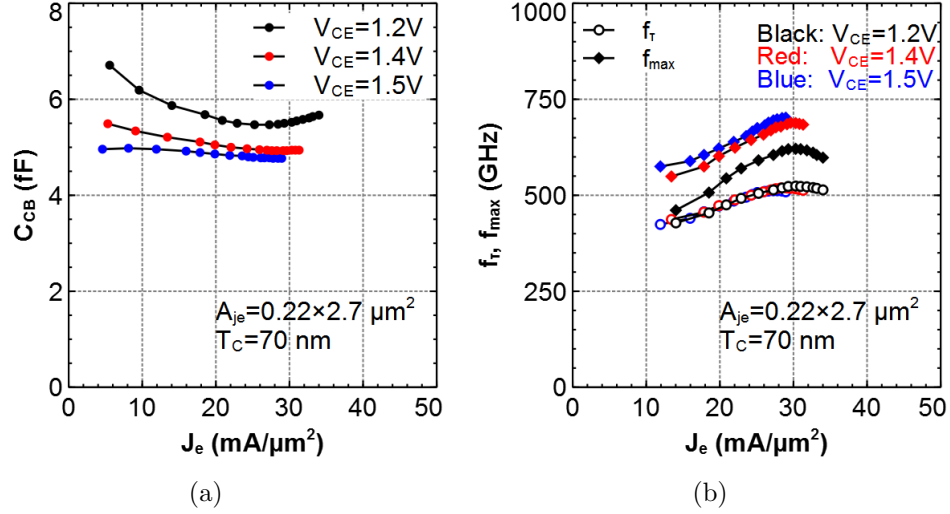


Figure 4.13: Current dependency of  $C_{CB}$  and cut-off frequencies extracted from the device on DHBT63B with  $W_{E,\text{design}} = 150 \text{ nm}$ ,  $W_{BM,\text{design}} = 750 \text{ nm}$ , and  $L_{E,\text{design}} = 3 \mu\text{m}$  at  $V_{CE} = 1.2, 1.4, \text{ and } 1.5 \text{ V}$ . (a)  $C_{CB}$  vs.  $J_E$ . (b)  $f_\tau$  and  $f_{max}$  vs.  $J_E$

$C_{CB}$  increases as the current density increases because of the base push-out (Kirk effect). For a given  $V_{CB}$  or  $V_{CE}$ ,  $C_{CB}$  reaches minimum when  $J_E \approx J_{C,\text{Kirk}}$ . Fig. 4.13a shows the extracted  $C_{CB}$  vs.  $J_E$  from the device with  $W_{E,\text{design}} = 150 \text{ nm}$ ,  $W_{BM,\text{design}} = 750 \text{ nm}$ , and  $L_{E,\text{design}} = 3 \mu\text{m}$  at various  $V_{CE}$ . For  $V_{CE} = 1.2 \text{ V}$ , the minimum of  $C_{CB}$  was observed at  $J_E = 27.3 \text{ mA}/\mu\text{m}^2$ , which is  $\sim 18.7\%$  higher than the calculated Kirk effect limited current density ( $23 \text{ mA}/\mu\text{m}^2$ ). The higher  $J_{C,\text{Kirk}}$  was expected because the areas associated with  $J_E$  and  $J_C$  are  $A_{je}$  and  $A_{jc}$ , and  $A_{je} < A_{jc}$  (current spreading effect). When  $V_{CE}$  was increased to  $1.5 \text{ V}$ , no  $C_{CB}$  minimum was observed because the base-emitter junction failed before reaching  $J_{C,\text{Kirk}}$ .

The cut-off frequencies vs. current density is shown in fig. 4.13b. The current gain cut-off frequency ( $f_\tau$ ) is almost independent of  $V_{CE}$  and peaks at  $J_E \approx 30 \text{ mA}/\mu\text{m}^2$ . The maxima of  $f_{max}$  are associated with the minima of  $C_{CB}$ .

Again, since the base-emitter junction failed before reaching  $J_{C,Kirk}$  at  $V_{CE}=1.5$  V, no maximum has been observed from  $f_{max}$  at this  $V_{CE}$ .

The RF measurement results of a device with  $W_{E,design}=100$  nm,  $W_{BM,design}=500$  nm, and  $L_{E,design}=3$   $\mu$ m is shown in fig. 4.14. From TEM analysis, the area of the base-emitter junction ( $A_{je}$ ) is  $\sim 0.17 \times 2.7$   $\mu$ m, and the average width of the base contact on both sides of the emitter ( $W_{B,Cont.}$ ) is  $\sim 87.5$  nm. Fig. 4.14a shows the unilateral Mason's gain (U) and current gain ( $H_{21}$ ) vs. frequency at  $J_E=28.5$  mA/ $\mu$ m<sup>2</sup>,  $I_B=900$   $\mu$ A, and  $V_{CE}=1.56$  V. Under this bias condition, the device achieves peak  $f_T/f_{max} \approx 490/670$  GHz according to the single-pole fit (dashed lines). The Smith chart showing the de-embedded two-port S-parameters of this device from 0.1 to 67 GHz is plotted in fig. 4.14b. The dashed lines in fig. 4.14b are the S-parameters simulated by ADS using the small-signal hybrid- $\pi$  equivalent circuit model shown in fig. 4.14c.

Fig. 4.15a is the extracted  $C_{CB}$  vs.  $J_E$  from the device with  $W_{E,design}=100$  nm,  $W_{BM,design}=500$  nm, and  $L_{E,design}=3$   $\mu$ m at various  $V_{CB}$ . For  $V_{CB}=0.2$  V, the minimum of  $C_{CB}$  was observed at  $J_E=29.2$  mA/ $\mu$ m<sup>2</sup>, which is  $\sim 27\%$  higher than the calculated value at 0.2 V (23 mA/ $\mu$ m<sup>2</sup>). Similar to the device reported previously with a wider emitter, when  $V_{CB}$  was increased to 0.6 V, no  $C_{CB}$  minimum was observed because the base-emitter junction failed prior to reaching  $J_{C,Kirk}$ .

The cut-off frequencies vs. current density is shown in fig. 4.15b. Similarly,  $f_T$  is independent of  $V_{CB}$  and peaks at  $J_E \approx 30.5$  mA/ $\mu$ m<sup>2</sup>. The maxima of  $f_{max}$  were observed for  $V_{CB}=0.2$  and 0.4 V. However, no maximum has been observed at  $V_{CB}=0.6$  V because of the  $J_E$  which the B-E junction could sustain is lower than the Kirk effect limited current density.

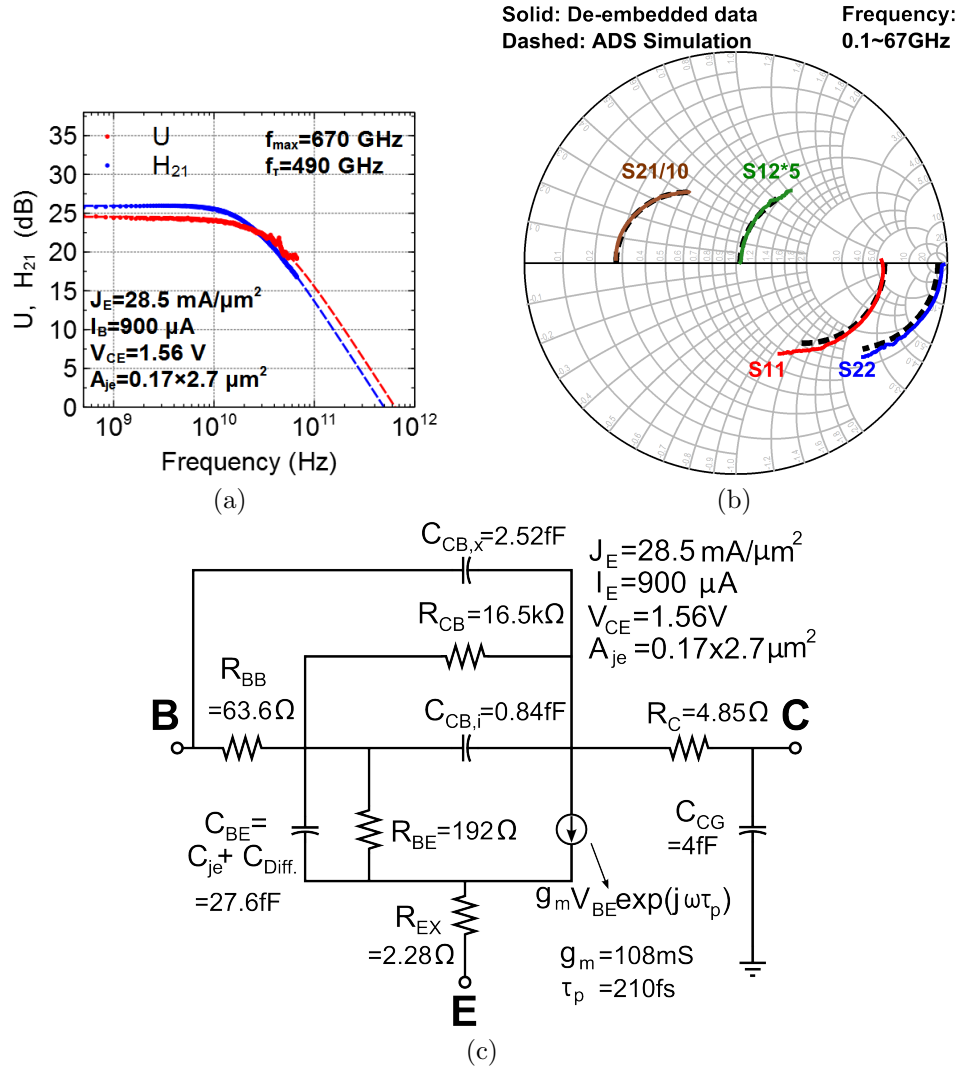


Figure 4.14: RF measurement results of a device on DHBT63B with  $W_{E,design} = 100$  nm,  $W_{BM,design} = 500$  nm, and  $L_{E,design} = 3$   $\mu$ m: (a) unilateral Mason's gain and  $H_{21}$  vs. frequency, (b) Two-port S-parameters vs. frequency, and (c) small-signal equivalent circuit. In both (a) and (b), the solid lines represent the experimental data, and the dashed lines are the ADS simulation results.

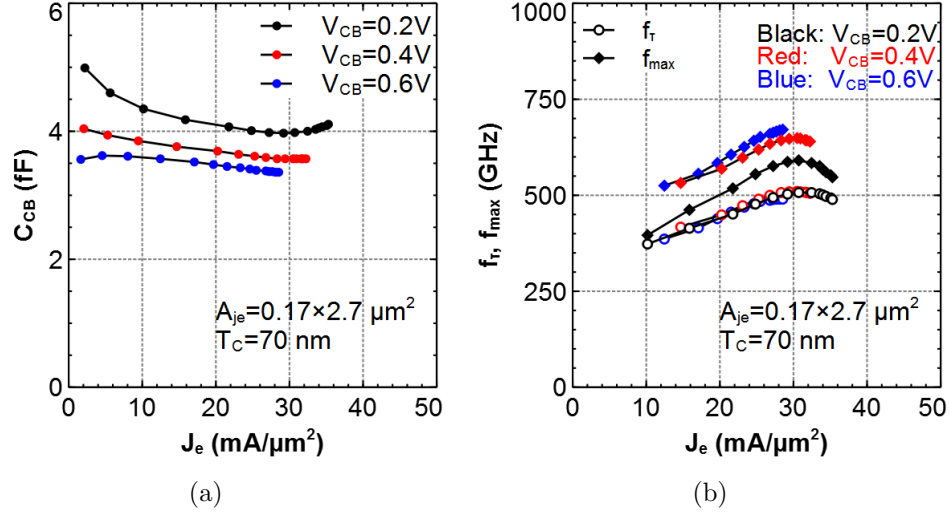


Figure 4.15: Current dependency of  $C_{CB}$  and cut-off frequencies extracted from the device on DHBT63B with  $W_{E,\text{design}}=100 \text{ nm}$ ,  $W_{BM,\text{design}}=500 \text{ nm}$ , and  $L_{E,\text{design}}=3 \mu\text{m}$  at  $V_{CB}=0.2, 0.4, \text{ and } 0.6 \text{ V}$ . (a)  $C_{CB}$  vs.  $J_E$ . (b)  $f_T$  and  $f_{max}$  vs.  $J_E$

By fitting the small-signal equivalent circuit models to the experimental data using ADS simulation, the parasitic resistances and capacitances of every probed device were extracted from the results biased at  $V_{CB}=0.5\sim 0.6 \text{ V}$  and  $J_E=25\sim 30 \text{ mA}/\mu\text{m}^2$ . Two dominating parasitics of  $f_{max}$ ,  $C_{CB}$  and the base access resistance ( $R_{BB}$ ), have been analyzed in order to understand the causes of low cut-off frequencies (highest measured  $f_{max} \approx 700 \text{ GHz}$ ).

The static (parallel-plate) component of  $C_{CB}$  can be written in the following expression:

$$\begin{aligned}
 C_{CB} &= \frac{\epsilon_0 \epsilon_r A_C}{T_{C,\text{eff}}} = \frac{\epsilon_0 \epsilon_r L_E}{T_{C,\text{eff}}} (W_{BM,\text{design}} - 2W_{\text{undercut}} + \frac{A_{BP}}{L_E}) \\
 &= \frac{\epsilon_0 \epsilon_r L_E W_{BM,\text{design}}}{T_{C,\text{eff}}} + C_{CB,\text{residual}} \\
 &= C_{CB,\text{WB}} \times W_{BM,\text{design}} + C_{CB,\text{residual}} ,
 \end{aligned} \tag{4.2}$$

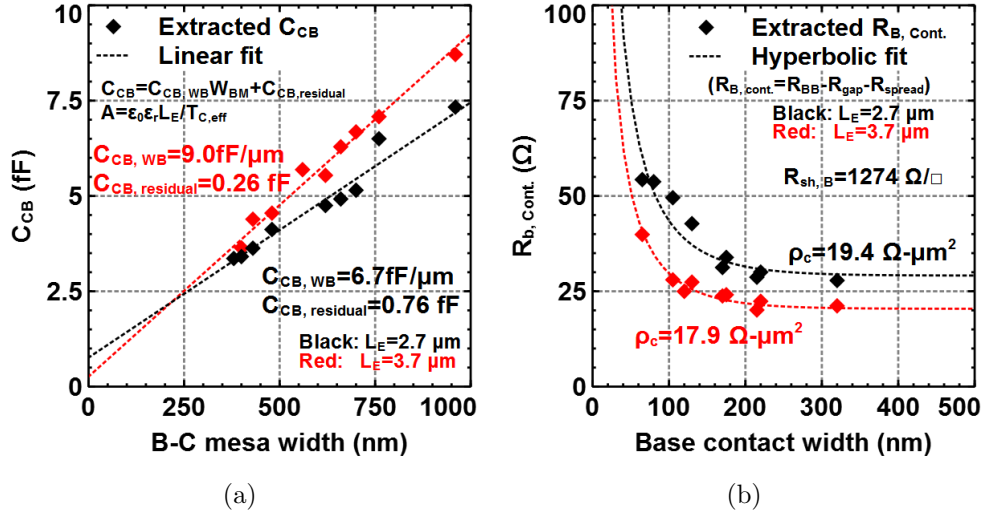


Figure 4.16: Dimension dependence of (a)  $C_{CB}$  (vs.  $W_{BM,design}$ ) and (b)  $R_{B,cont.}$  (vs.  $W_{B,cont.}$ ) from device with  $L_E = 2.7$  and  $3.7 \mu\text{m}$  biased at  $V_{CB} = 0.5 \sim 0.6 \text{ V}$  and  $J_E = 25 \sim 30 \text{ mA}/\mu\text{m}^2$ .

where  $\epsilon_0$  and  $\epsilon_r$  are the vacuum permittivity and the relative permittivity. For InP collector,  $\epsilon_r \approx 13$ .  $A_C$  and  $T_{C,eff}$  are the area and the depletion region width of the base-collector junction, respectively.  $A_{BP}$  is the excessive portion of  $A_C$  beneath the base post. The slope,  $C_{CB,WB}$ , is the capacitance per unit width of the B-C mesa. The intercept,  $C_{CB,residual}$ , is the effect due to both the B-C mesa undercut and excessive base post area, which are independent to  $W_{BM,design}$ .

The extracted  $C_{CB}$  vs. the designed base mesa width ( $W_{BM,design}$ ) is plotted in Fig. 4.16a. The slopes of the curves,  $C_{CB,WB}$ , for devices with  $L_E = 2.7$  and  $3.7 \mu\text{m}$  are  $6.7$  and  $9 \text{ fF}/\mu\text{m}$ , respectively. The trend of  $C_{CB,WB}$  vs.  $L_E$  indicates that  $T_{C,eff} \approx 50 \text{ nm}$ , which is less than the overall collector thickness ( $70 \text{ nm}$ ). The intercepts of the curves,  $C_{CB,residual}$ , for devices with  $L_E = 2.7$  and  $3.7 \mu\text{m}$  are  $0.76$  and  $0.26 \text{ fF}$ , respectively.

Eq. 4.2 can be transformed into:

$$A_{BP} = \left( \frac{C_{CB,residual}}{C_{CB,WB}} + 2W_{undercut} \right) L_E. \quad (4.3)$$

If  $C_{CB,WB}$ ,  $C_{CB,residual}$ ,  $W_{undercut}$ , and  $L_E$  known, the excessive area beneath the base post ( $A_{BP}$ ) can be obtained. From TEM analysis,  $W_{undercut}=62.5$  nm. Thus,  $A_{BP}$  is approximately 0.64 and  $0.57 \mu\text{m}^2$  for devices with  $L_E=2.7$  and  $3.7 \mu\text{m}$ , respectively.

From eq. 2.14, the base access resistance can be written as:

$$\begin{aligned} R_{BB} &\approx R_{BE,spread} + R_{gap} + R_{B,cont.} \\ &= \frac{R_{sh,em}W_E}{12L_E} + \frac{R_{sh,gap}W_{gap}}{2L_E} + \frac{\sqrt{R_{sh,B,cont.}\rho_{B,cont.}}}{2L_E} \coth\left(\frac{W_{B,cont.}}{L_T}\right), \end{aligned} \quad (4.4)$$

where  $R_{sh,em}$ ,  $R_{sh,gap}$ , and  $R_{sh,B}$  are the sheet resistance beneath the emitter, in the spacing between the base contact and the emitter (the extrinsic base), and beneath the base contact, respectively.  $\rho_{B,cont.}$  is the specific contact resistivity of the base contact.  $L_T = \sqrt{\rho_{B,cont.}/R_{sh,B,cont.}}$  is the transfer length.

The base contact resistance term ( $R_{B,cont.}$ ) is analyzed in order to estimate  $\rho_{B,cont.}$  of the experimental devices. To extract  $R_{B,cont.}$ , eq. 4.4 can be transformed into:

$$\begin{aligned} R_{B,cont.} &= R_{BB} - R_{BE,spread} - R_{gap} \\ \frac{\sqrt{R_{sh,B,cont.}\rho_{B,cont.}}}{2L_E} \coth\left(\frac{W_{B,cont.}}{L_T}\right) &= R_{BB} - \frac{R_{sh,em}W_E}{12L_E} - \frac{R_{sh,gap}W_{gap}}{2L_E}, \end{aligned} \quad (4.5)$$

From TEM analysis, the actual dimensions ( $W_E$ ,  $L_E$ ,  $W_{gap}$ , and  $W_{B,cont.}$ ) of the devices are known.  $R_{sh,em}$  and  $R_{sh,gap}$  are obtained from the pinched and the unpinched base TLM structure (fig. 4.7). The contribution of  $R_{BE,spread}$  and

$R_{\text{gap}}$  were calculated and then subtracted from  $R_{\text{BB}}$  to extract  $R_{\text{B,cont.}}$ . Also from the TEM analysis, the base metal penetrated 5~6 nm below the B-E junction. With 6 nm penetration depth and  $\sim 2$  nm depletion width under the base contact,  $R_{\text{sh,B}} \approx 1274 \Omega/\square$ . A plot of  $R_{\text{B,cont.}}$  vs.  $W_{\text{B,cont.}}$  is shown in fig. 4.16b. By fitting the hyperbolic expression of  $R_{\text{B,cont.}}$ ,  $\rho_{\text{B,cont.}}$  can be extrapolated. The result from device with  $L_{\text{E}}=2.7$  and  $3.7 \mu\text{m}$  indicates  $\rho_{\text{B,cont.}}=19.4$  and  $17.9 \Omega - \mu\text{m}^2$ , respectively. Compare to  $\rho_{\text{B,cont.}}$  obtained from base TLMs,  $\rho_{\text{B,cont.}}$  extracted from two-port S-parameters are almost two times higher.

Such high  $\rho_{\text{B,cont.}}$  causes high  $R_{\text{BB}}$  and longer RC delay in the B-C mesa, reducing  $f_{\text{max}}$ . High  $\rho_{\text{B,cont.}}$  also increase the  $L_{\text{T}}$ , which means  $R_{\text{B,cont.}}$  increases more rapidly when  $W_{\text{B,cont.}}$  decreases. Therefore, the  $f_{\text{max}}$  of the devices with narrow emitter and B-C mesa are further reduced. The poor base specific contact resistivity explains the measured low  $f_{\text{max}}$ .

## 4.3 DHBT58H

### 4.3.1 Device structure and process feature

The design of DHBT58 utilizes a 30 nm thick InP emitter doped at  $5 \times 10^{19} \text{cm}^{-3}$  for the top 15 nm and  $2 \times 10^{18} \text{cm}^{-3}$  for the bottom 15 nm. The p-type base is composed of 20 nm of InGaAs with a doping-grade from  $12 \times 10^{19} \text{cm}^{-3}$  at the emitter side to  $8 \times 10^{19} \text{cm}^{-3}$  at the collector side. The design employs a 100 nm thick collector structure (setback, superlattice, InP collector) with doping concentration of  $5 \times 10^{16} \text{cm}^{-3}$ . The detailed epitaxial structure is listed in table. 4.3. The band diagram of the device under  $V_{\text{BE}}=1.2 \text{V}$  and  $V_{\text{CB}}=0.6 \text{V}$  is shown



in fig. 4.17. The solid lines are the conduction band and the valance band if the space charge associated with the collector current in the collector region is neglected, whereas the dashed lines are the bands considering the space charge in the collector at  $J_C \approx 25 \text{ mA}/\mu\text{m}^2$ .

The base-emitter junction width of the devices on DHBT63B is 70 nm wider

Layer	Semiconductor	Thickness (Å)	Doping ( $\text{cm}^{-3}$ )
Emitter cap	$\text{In}_{0.53}\text{Ga}_{0.47}\text{As}$	100	$8 \times 10^{19}:\text{Si}$
Emitter	InP	150	$5 \times 10^{19}:\text{Si}$
Emitter	InP	150	$2 \times 10^{18}:\text{Si}$
Base	$\text{In}_{0.53}\text{Ga}_{0.47}\text{As}$	200	$12 - 8 \times 10^{19}:\text{C}$
Setback	$\text{In}_{0.53}\text{Ga}_{0.47}\text{As}$	135	$5 \times 10^{16}:\text{Si}$
B-C grade	-	165	$5 \times 10^{16}:\text{Si}$
$\delta$ -doping	InP	30	$3.6 \times 10^{18}:\text{Si}$
Collector	InP	670	$5 \times 10^{16}:\text{Si}$
Sub-collector	InP	75	$2 \times 10^{19}:\text{Si}$
Sub-collector	$\text{In}_{0.53}\text{Ga}_{0.47}\text{As}$	50	$4 \times 10^{19}:\text{Si}$
Sub-collector	InP	3000	$1 \times 10^{19}:\text{Si}$
Etch stop	$\text{In}_{0.53}\text{Ga}_{0.47}\text{As}$	35	undoped
Substrate	InP	-	undoped

Table 4.3: Epitaxial structure of DHBT58.

than the design value. As a result, the base contact width is 35 nm narrower than the design value. To compensate this effect, in the fabrication of DHBT58H, the emitter width including the  $\text{SiN}_x$  sidewall thickness (20 nm) is measured by SEM prior to the InP emitter wet etch. An extra 40 nm due to the  $\text{SiN}_x$  sidewall is added to the assumed emitter junction width ( $W_{E,\text{assumed}}$ ). In response to the extra  $W_{E,\text{design}}$ , the B-C mesa width ( $W_{\text{BM},\text{design}}$ ) was increased to  $W_{\text{BM},\text{mod.}}$  to maintain the ratio between the emitter and base contact, i.e.

$$W_{\text{BM},\text{mod.}} = W_{E,\text{assumed}} \frac{W_{\text{BM},\text{design}}}{W_{E,\text{design}}} . \quad (4.6)$$

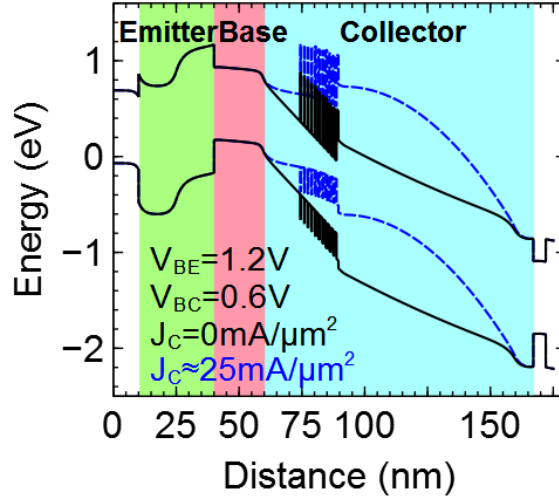


Figure 4.17: Computed band diagram of DHBT58 under  $V_{BE}=1.2\text{ V}$  and  $V_{CB}=0.6\text{ V}$ . The solid lines are the conduction and valance bands when  $J_C=0\text{ mA}/\mu\text{m}^2$ . The dashed line represent the conduction and valance bands considering the space charge region in the collector at  $J_C \approx 25\text{ mA}/\mu\text{m}^2$ .

For device with  $W_{E,\text{design}}=100\text{ nm}$  and  $W_{BM,\text{design}}=450\text{ nm}$ , the B-C mesa width after modulation  $W_{BM,\text{mod.}}$  is 630 nm.

The base metalization of DHBT58H was also a lift-off process using UV-6 as the resist. Nonetheless, the resist damage problem due to electron bombardment in UCSB's E-Beam 4 have been solved by removing the Ni source from the chamber before the evaporation. Therefore, the base metalization was done entirely in E-Beam 4. In addition, the process flow for the composite third sidewall was incorporated into the fabrication of DHBT58H. The lift-off base contact of DHBT58H is composed of 6/12/17/65/10 nm of Pt/Ti/Pd/Au/Ti. The extra Ti layer on top of Au layer serves as an adhesion layer between Au and the dielectric of the third sidewall. After the base contact lift-off, the extrinsic base is encapsulated by ALD  $\text{Al}_2\text{O}_3$  and PECVD  $\text{SiN}_x$ .

### 4.3.2 TEM analysis

Fig. 4.18a is the TEM cross-section normal to the emitter stripe of the device with  $W_{E,\text{design}}=100$  nm,  $W_{BM,\text{design}}=450$  nm defined by e-beam lithography. The composite refractory metal stack above the Mo emitter contact consists of  $\sim 150$  nm of W and  $\sim 350$  nm of TiW. With higher TiW to W thickness ratio and recalibrated dry etch recipe, a more vertical the sidewall profile was achieved. The width of the composite stack at its bottom is 10 nm wider than  $W_{E,\text{design}}$ . The base-emitter junction width is approximately the same as stack width, i.e.  $W_{E,\text{actual}}=110$  nm for  $W_{E,\text{design}}=100$  nm. This means that  $W_{E,\text{assumed}}$  from SEM before InP emitter wet etch was incorrect, and the modulation for the B-C mesa width is unnecessary. Thus, the B-C mesa is too wide, causing unnecessary increase in  $C_{CB}$ . According to TEM,  $W_{\text{gap}} \approx 10$  nm, and the undercut to the base-collector mesa ( $W_{\text{undercut}}$ ) is  $\sim 50$  nm on both sides of the mesa. The average width of the base contact on each side of the emitter for the device with  $W_{E,\text{design}}=100$  nm and  $W_{BM,\text{design}}=450$  nm is then:

$$\begin{aligned} W_{\text{BCont.}} &= (W_{BM,\text{mod.}} - W_{E,\text{actual}} - 2 \times (W_{\text{gap}} + W_{\text{undercut}}))/2 \\ &= (630 - 110 - 2 \times (10 + 50))/2 = 200 \text{ nm.} \end{aligned}$$

Fig. 4.18b is the TEM cross-section of the same device as Fig. 4.18a under higher magnification power zoomed in at the vicinity of the emitter and the base contact. As shown in the TEM cross-section, 1 nm of InGaAs was removed from the surface of the base semiconductor due to the diluted HCl etch prior to the base metalization. The base metal penetrates the InGaAs base for 4 nm because of the reaction between Pt and As atoms [6]. Hence, the base contact is located at  $\sim 5$  nm below the base-emitter junction. The cross-section parallel to the emit-

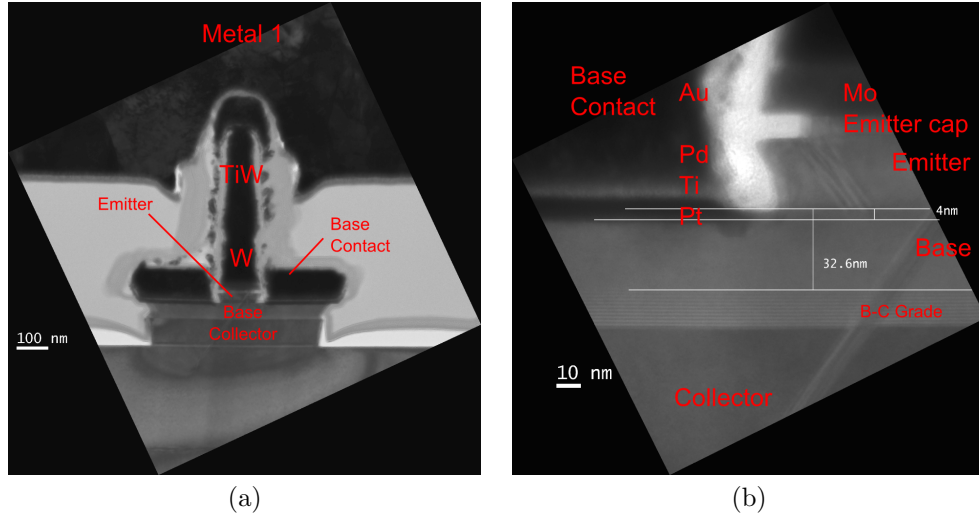


Figure 4.18: TEM cross-section normal to the emitter stripe of a device on DHBT58H with  $W_{E,\text{design}}=100$  nm,  $W_{BM,\text{design}}=450$  nm. (a) An overview of the device. (b) zoomed in at the vicinity of the base contact and emitter.

ter stripe of DHBT58H has not been imaged by TEM. The undercut to the InP emitter along the stripe is assumed to be the same as in DHBT63B, i.e. 150 nm at both tips.

### 4.3.3 TLM results

The pinched base TLM results of DHBT58H is shown in fig. 4.19a. The values of the base sheet resistance obtained from the pinched TLM is  $785 \Omega/\square$ , which is slightly higher than the value measured by IQE ( $717 \Omega/\square$ ) with the InGaAs surface terminated by the InP emitter layer. The specific base contact resistivity extrapolated from the pinched TLM results is  $1.5 \Omega - \mu\text{m}^2$ , which is lower than the value required ( $4 \Omega - \mu\text{m}^2$ ) to achieve 1 THz  $f_{\text{max}}$  at  $W_E=100$  nm. A complete analysis on the  $\rho_{B,\text{cont.}}$  will be addressed in the later section along

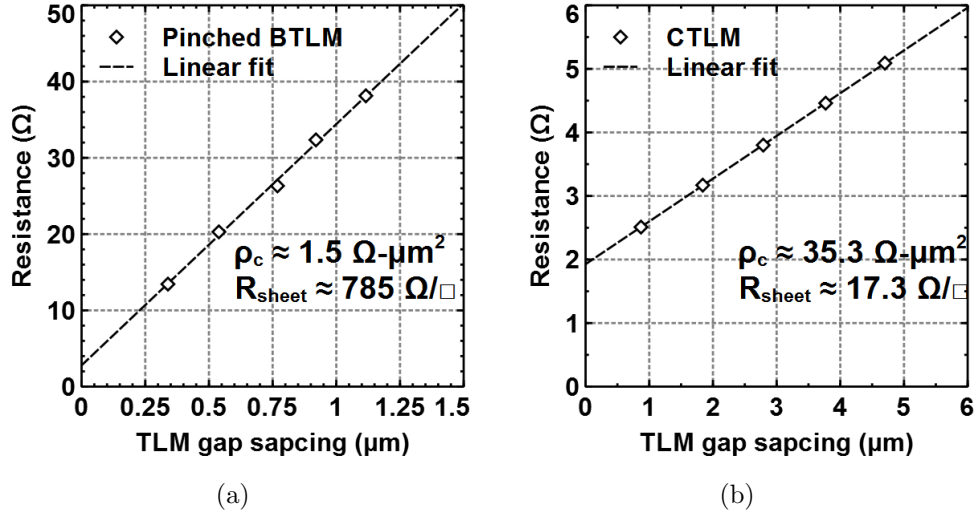


Figure 4.19: (a) Pinched base TLM and (b) Collector TLM data of DHBT58H. The width of TLM structure and the distances between metal pads (gap spacing) were measured with SEM.

with the  $R_{\text{BB}}$  extracted from the RF measurements. 4.19b is the collector TLM result of DHBT63B. The collector sheet resistance and specific contact resistivity are  $35.3 \Omega/\square$  and  $17.3 \Omega - \mu\text{m}^2$ , respectively.

#### 4.3.4 Transistor DC characteristics

The maximum emitter current density limited by the Kirk effect ( $J_{\text{C,Kirk}}$ ) at  $v_{\text{CB}}=0.7 \text{ V}$  for the epitaxial design of DHBT58 is approximately  $20 \text{ mA}/\mu\text{m}^2$ . The actual limit could be more than 20% higher when considering the current spreading effect in the collector region. Unlike DHBT63B, the B-E junction can sustain the Kirk effect limited current density. However, to protect the B-E junction from failure before the subsequent RF measurement, current and power compliance was set for the emitter terminal during the DC measurements. The sweeping range for  $V_{\text{BE}}$  was limited from 0 to 1 V in the measurement for diode I-V characteristics

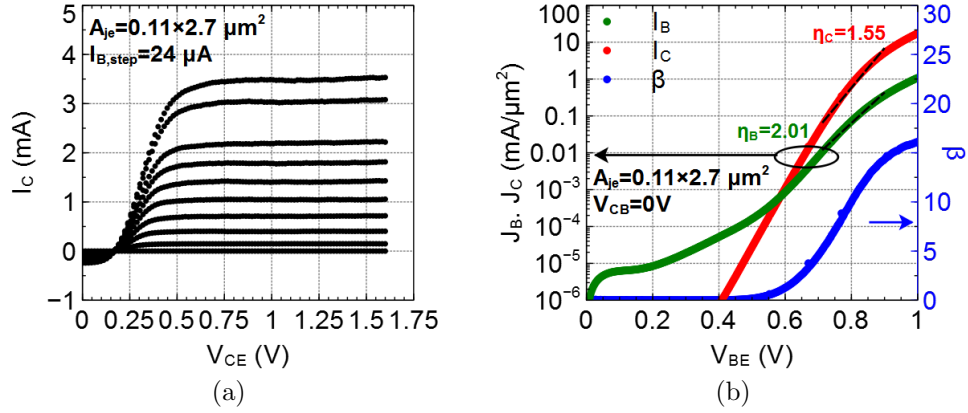


Figure 4.20: DC characteristics of the device with  $W_{E,\text{design}}=100$  nm,  $W_{\text{BM},\text{design}}=600$  nm, and  $L_{E,\text{design}}=3$   $\mu\text{m}$ . (a) Common emitter output characteristics. The increment of the base current ( $I_{B,\text{step}}$ ) is  $24$   $\mu\text{A}$ . (b) I-V characteristics of B-E and B-C diodes (Gummel plot).

(Gummel plots).

Fig. 4.20a is the common emitter output characteristic of a device with  $W_{E,\text{design}}=100$  nm,  $W_{\text{BM},\text{design}}=600$  nm, and  $L_{E,\text{design}}=3$   $\mu\text{m}$ , i.e.  $W_{E,\text{actual}}=110$  nm,  $W_{\text{B},\text{cont.}}=305$  nm, and  $L_{E,\text{actual}}=2.7$   $\mu\text{m}$ . The base current varies from 0 to  $240$   $\mu\text{A}$  with a step of  $24$   $\mu\text{A}$ . The Gummel plot of the same device at  $V_{\text{CB}}=0$  V is shown in fig. 4.20b. At  $V_{\text{BE}}=1$  V, the emitter current density and the DC current gain ( $\beta$ ) are approximately  $18$   $\text{mA}/\mu\text{m}^2$  and  $16.1$ , respectively. The B-E and B-C diode ideality factors,  $\eta_{\text{B}}$  and  $\eta_{\text{C}}$ , extrapolated from the data within  $V_{\text{BE}}=0.7$  to  $0.9$  V are  $2.01$  and  $1.55$ , respectively.

With the better control on the sidewall profile of the emitter metal stack, working devices with  $W_{E,\text{actual}}=85$  nm has been achieved on DHBT58H. This extend the range of the device dimensions in the analysis of both DC and RF data. The dependence of DC- $\beta$  on device dimensions of DHBT58H has been analyzed. The DC- $\beta$  of the devices are sampled at  $V_{\text{CB}}=0$  V and  $J_{\text{E}}=20\sim 25$   $\text{mA}/\mu\text{m}^2$ , which

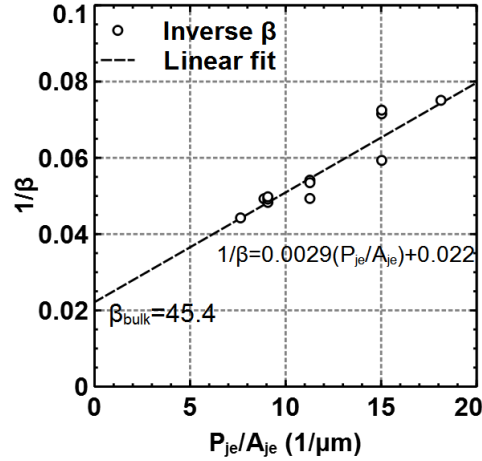


Figure 4.21: Inverse DC- $\beta$  vs. base-emitter junction periphery to area ratio ( $P_{je}/A_{je}$ ) of the devices on DHBT58H.

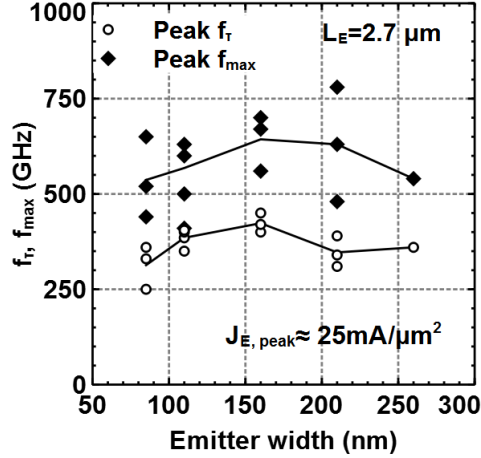
is close to  $J_{C,Kirk}$  and  $J_E$  for peak  $f_\tau$  and  $f_{max}$ . Inverse DC- $\beta$  vs.  $P_{je}/A_{je}$  of the devices on DHBT58H is plotted in fig. 4.21. According to the extrapolation, the DC- $\beta$  ( $\beta_{Bulk}$ ) of a device with a very wide emitter, i.e.  $P_{je}/A_{je} \rightarrow 0$ , is  $\sim 45.4$ , and the sheet current density of the base edge current ( $K_{B,edge}$ ) is  $\sim 70$  mA/ $\mu\text{m}$ . At  $W_E=85$  nm, DC- $\beta \approx 13.3$ , which implies that approximately 44% of  $I_B$  could be attributed to the edge current.

### 4.3.5 RF performance

The calculated  $f_\tau$  and  $f_{max}$  for a device on DHBT58 with the assumed parameters listed in table. 4.4 are approximately 530 and 1030 GHz, respectively. Nonetheless, the highest  $f_\tau/f_{max}$  measured on DHBT58H is approximately 390/780 GHz, measured from a device with  $W_{E,actual}=210$  nm,  $W_{B,Cont.}=255$  nm,  $L_{E,actual}=2.7$   $\mu\text{m}$ . Fig. 4.22 is a summary of the peak cut-off frequencies measured on DHBT58H. The peak current gain cut-off frequency varies from 250 to

Parameters		Value	Unit
Emitter width	$W_E$	200	nm
Emitter length	$L_E$	3	$\mu\text{m}$
B-E spacing	$W_{\text{gap}}$	10	nm
Base contact width (single side)	$W_{\text{B,Cont.}}$	200	nm
Excessive base post area	$A_{\text{BP}}$	0.8	$\mu\text{m}^2$
Emitter contact resistivity	$\rho_{\text{E,cont.}}$	4	$\Omega - \mu\text{m}^2$
Base contact resistivity	$\rho_{\text{B,cont.}}$	4	$\Omega - \mu\text{m}^2$
Base sheet resistance	$R_{\text{sheet,B}}$	750	$\Omega/\square$
$e^-$ diffusivity in the base	$D_{\text{n,B}}$	40	$\text{cm}^2/\text{s}$
$e^-$ velocity in the collector	$v_C$	$3.2 \times 10^7$	$\text{cm}/\text{s}$
Emitter current density	$J_E$	17	$\text{mA}/\mu\text{m}^2$
B-E diode ideality factor	$\eta_B$	2	

Table 4.4: Parameters assumed in the cut-off frequencies calculation of DHBT63.

Figure 4.22: Peak  $f_\tau$  and  $f_{\text{max}}$  vs. base-emitter junction width of the devices with emitter length,  $L_E=2.7 \mu\text{m}$  on DHBT58H.

450 GHz, and the peak power gain cut-off frequency lies within 410 and 780 GHz.

The measured low  $f_\tau$  could be explained by the high B-E diode ideality factors ( $\sim 2.5$  for most devices), which result in lower transconductance ( $g_m$ ) and high emitter resistance ( $r_E$ ) [7]. Hence, the charging delays associated with  $r_E$  increases, reducing  $f_\tau$ . The discrepancies between the calculated and measured



$f_{\max}$  is likely due to high  $R_{\text{BB}}C_{\text{CB}}$  delay. Although the base TLMs of DHBT58H indicates low base specific contact resistivity ( $\rho_{B,\text{cont.}}$ ), the  $\rho_{B,\text{cont.}}$  of the device could still be high according to the analysis on the  $R_{\text{BB}}$  of DHBT63B. As a result,  $R_{\text{BB}}$  could be higher than expected, reducing  $f_{\max}$ . Moreover, the actual emitter widths were overestimated during the fabrication. Therefore, the modulation for B-C mesa widths based on the incorrect estimation are too wide, resulting in more  $C_{\text{CB}}$ , and hence  $f_{\max}$  drops.

Similar to DHBT63B, the RF measurement results of two devices on DHBT58H are selected and reported in this section as examples for the probed devices. To understand the measured RF performance, the base access resistances and the base-collector capacitances extracted from small-signal equivalent circuit model of each probed devices are analyzed.

The first device has  $W_{\text{E,design}}=200$  nm,  $W_{\text{BM,design}}=700$  nm, and  $L_{\text{E,design}}=3$   $\mu\text{m}$ . From the TEM analysis, the area of the base-emitter junction ( $A_{\text{je}}$ ) is  $\sim 0.21 \times 2.7$   $\mu\text{m}$ , and the average width of the base contact on both sides of the emitter ( $W_{\text{B,Cont.}}$ ) is  $\sim 255$  nm. Fig. 4.23a is the unilateral Mason's gain (U) and current gain ( $H_{21}$ ) vs. frequency at  $J_{\text{E}}=23.3$  mA/ $\mu\text{m}^2$ ,  $I_{\text{B}}=650$   $\mu\text{A}$ , and  $V_{\text{CE}}=1.7$  V. The device demonstrates  $f_{\tau}/f_{\max} \approx 390/780$  GHz according to the single-pole fit (dashed lines). Fig. 4.23b is the Smith chart showing the de-embedded two-port S-parameters of this device from 0.1 to 67 GHz. Using ADS, a small-signal equivalent circuit based on the hybrid- $\pi$  model is simulated and fit to the experimental data. The dashed lines in fig. 4.23b are the ADS simulation results. The small-signal equivalent circuit model used in ADS simulation is shown in fig. 4.23c.

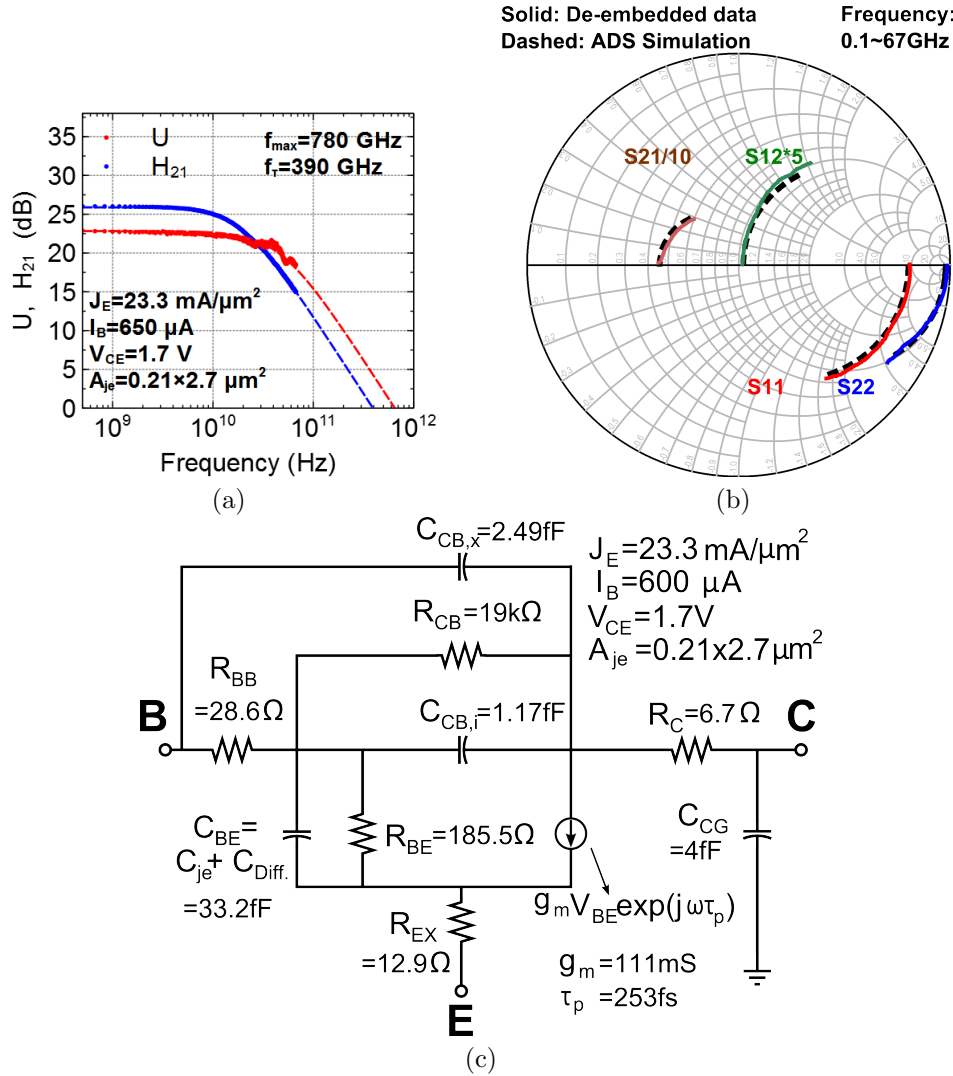


Figure 4.23: RF measurement results of a device on DHBT58H with  $W_{E,design} = 200 \text{ nm}$ ,  $W_{BM,design} = 700 \text{ nm}$ , and  $L_{E,design} = 3 \mu\text{m}$ : (a) unilateral Mason's gain and  $H_{21}$  vs. frequency, (b) Two-port S-parameters vs. frequency, and (c) small-signal equivalent circuit. In (a) and (b), the solid lines represent the experimental data, and the dashed lines are the ADS simulation results.

Fig. 4.24a shows the extracted  $C_{CB}$  vs.  $J_E$  from the device with  $W_{E,design} = 200 \text{ nm}$ ,  $W_{BM,design} = 700 \text{ nm}$ , and  $L_{E,design} = 3 \mu\text{m}$  at  $V_{CE} = 1.2, 1.4,$  and  $1.7 \text{ V}$ . For  $V_{CE} = 1.7 \text{ V}$ ,  $V_{CB} \approx 0.5 \text{ V}$ , and the minimum of  $C_{CB}$  was observed at  $J_E = 15.4 \text{ mA}/\mu\text{m}^2$ ,

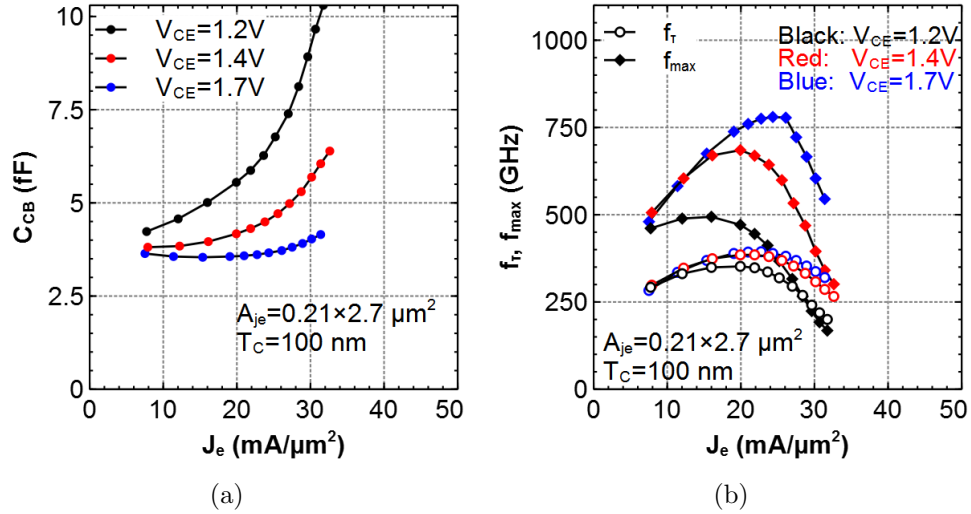


Figure 4.24: Current dependency of  $C_{CB}$  and cut-off frequencies extracted from the device on DHBT58H with  $W_{E,\text{design}}=200 \text{ nm}$ ,  $W_{BM,\text{design}}=700 \text{ nm}$ , and  $L_{E,\text{design}}=3 \mu\text{m}$  at  $V_{CE}=1.2, 1.4,$  and  $1.7 \text{ V}$ . (a)  $C_{CB}$  vs.  $J_E$ . (b)  $f_\tau$  and  $f_{max}$  vs.  $J_E$

which is close to calculated Kirk effect limited current density ( $17 \text{ mA}/\mu\text{m}^2$ ).

The cut-off frequencies vs. current density is shown in fig. 4.24b. At  $V_{CE}=1.7 \text{ V}$ ,  $f_\tau$  peaks at  $J_E \approx 23 \text{ mA}/\mu\text{m}^2$ . When  $V_{CE}$  increases, the current density limit ( $J_{C,\text{Kirk}}$ ) becomes higher. Higher emitter current reduces  $r_e$ , and hence the emitter charging time decreases. Therefore, the peak  $f_\tau$  and its corresponding  $J_E$  both increase as  $V_{CE}$  becomes higher. At  $V_{CE}=1.7 \text{ V}$ , the maximum of  $f_{max}$  were also found at  $J_E \approx 23 \text{ mA}/\mu\text{m}^2$  since  $C_{CB}$  rises slowly with  $J_E$  at the vicinity of the Kirk effect limit current density.

The RF performance of a device with  $W_{E,\text{design}}=100 \text{ nm}$ ,  $W_{BM,\text{design}}=600 \text{ nm}$ , and  $L_{E,\text{design}}=3 \mu\text{m}$  is shown in fig. 4.25. From TEM analysis, the area of the base-emitter junction ( $A_{je}$ ) is  $\sim 0.11 \times 2.7 \mu\text{m}$ , and the average width of the base contact on both sides of the emitter ( $W_{B,\text{Cont.}}$ ) is  $\sim 305 \text{ nm}$ . Fig. 4.25a shows the unilateral Mason's gain ( $U$ ) and current gain ( $H_{21}$ ) vs. frequency at  $J_E=33.2 \text{ mA}/\mu\text{m}^2$ ,

$I_B=600 \mu\text{A}$ , and  $V_{CE}=1.7 \text{ V}$ . The device exhibits peak  $f_\tau/f_{\max} \approx 405/630 \text{ GHz}$  according to the single-pole fit (dashed lines). The Smith chart of the de-embedded two-port S-parameters of this device from 0.1 to 67 GHz is plotted in fig. 4.25b. The dashed lines in fig. 4.25b represent the S-parameters simulated by ADS using the small-signal hybrid- $\pi$  equivalent circuit model shown in fig. 4.25c.

The extracted  $C_{CB}$  vs.  $J_E$  from the device with  $W_{E,\text{design}}=100 \text{ nm}$ ,  $W_{BM,\text{design}}=600 \text{ nm}$ , and  $L_{E,\text{design}}=3 \mu\text{m}$  at various  $V_{CB}$  is plotted in fig. 4.26a. At  $V_{CE}=1.7 \text{ V}$  ( $V_{CB} \approx 0.5 \text{ V}$ ),  $C_{CB}$  reaches minimum at  $J_E=30.1 \text{ mA}/\mu\text{m}^2$ , which is 76% higher than the calculated value ( $17 \text{ mA}/\mu\text{m}^2$ ). The high emitter current density could be explained by the current spreading effect in the collector region. Because the width of the B-C mesa (740 nm) is far greater the width of the B-E junction (110 nm),  $A_{jc} \gg A_{je}$ , and more  $J_E$  is required for  $J_C = J_{C,\text{Kirk}}$ .

The cut-off frequencies vs. current density is shown in fig. 4.26b. The peak  $f_\tau$  and its corresponding  $J_E$  both increase slightly as  $V_{CE}$  becomes higher. At  $V_{CE}=1.7 \text{ V}$ , since  $C_{CB}$  nearly remains constant between 20 and 35  $\text{mA}/\mu\text{m}^2$ ,  $f_{\max}$  is dominated by  $f_\tau$ . The current density for peak  $f_\tau$  (405 GHz) and peak  $f_{\max}$  (630 GHz) coincide at 31.5  $\text{mA}/\mu\text{m}^2$ .

The small-signal equivalent circuit models of the probed devices were computed and fitted to the RF measurement results biased at  $V_{CE}=1.7 \text{ V}$  and  $J_E=25\sim 30 \text{ mA}/\mu\text{m}^2$ , the bias points for the peak RF performance.  $C_{CB}$  and  $R_{BB}$  have been analyzed in order to understand the causes of low cut-off frequencies.

$C_{CB}$  vs. the designed base mesa width ( $W_{BM,\text{design}}$ ) of devices with  $L_E=2.7 \mu\text{m}$  is plotted in Fig. 4.27a. The slopes of the curves,  $C_{CB,WB}$ , is 4.1  $\text{fF}/\mu\text{m}$ , which indicates that  $T_{C,\text{eff}} \approx 76 \text{ nm}$  instead of the design collector thickness (100 nm). The

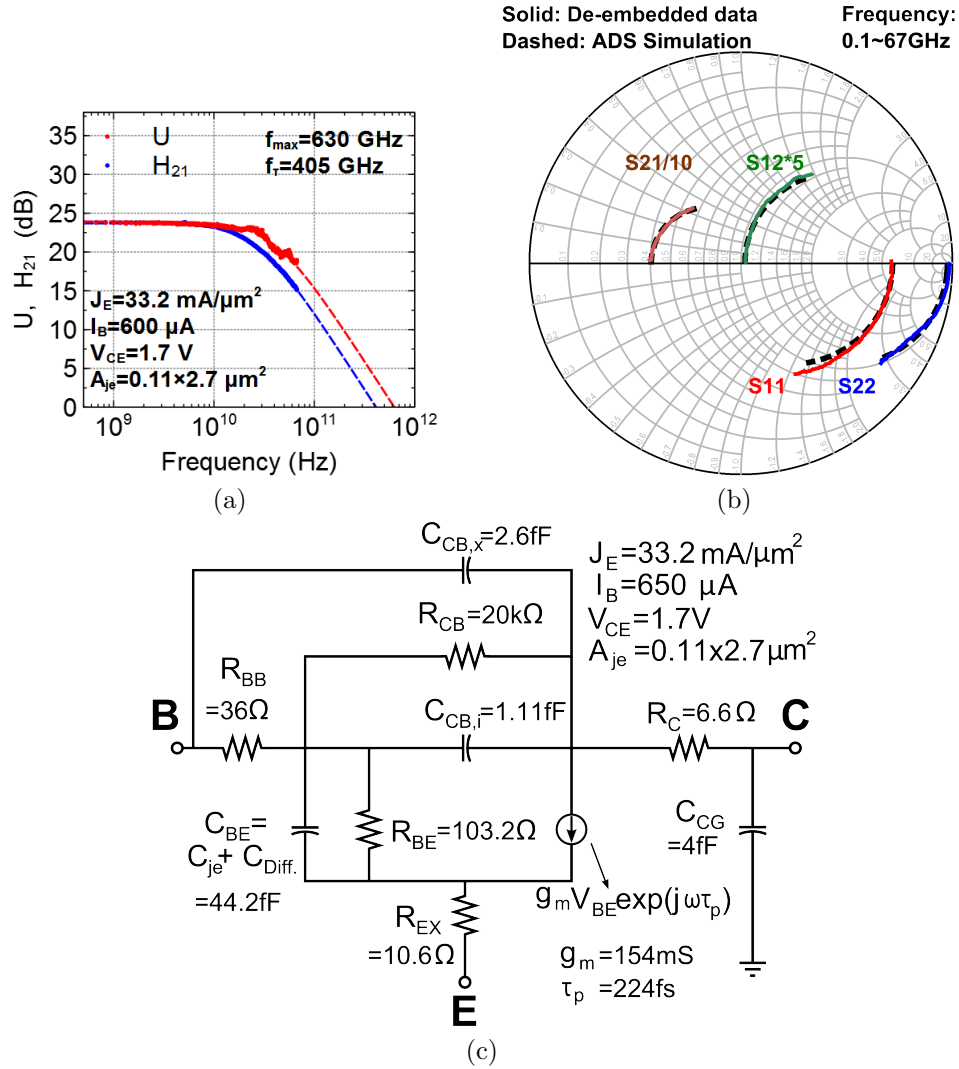


Figure 4.25: RF measurement results of a device on DHBT58H with  $W_{E,design} = 100$  nm,  $W_{BM,design} = 600$  nm, and  $L_{E,design} = 3$   $\mu\text{m}$ : (a) unilateral Mason's gain and  $H_{21}$  vs. frequency, (b) Two-port S-parameters vs. frequency, and (c) small-signal equivalent circuit. In both (a) and (b), the solid lines represent the experimental data, and the dashed lines are the ADS simulation results.

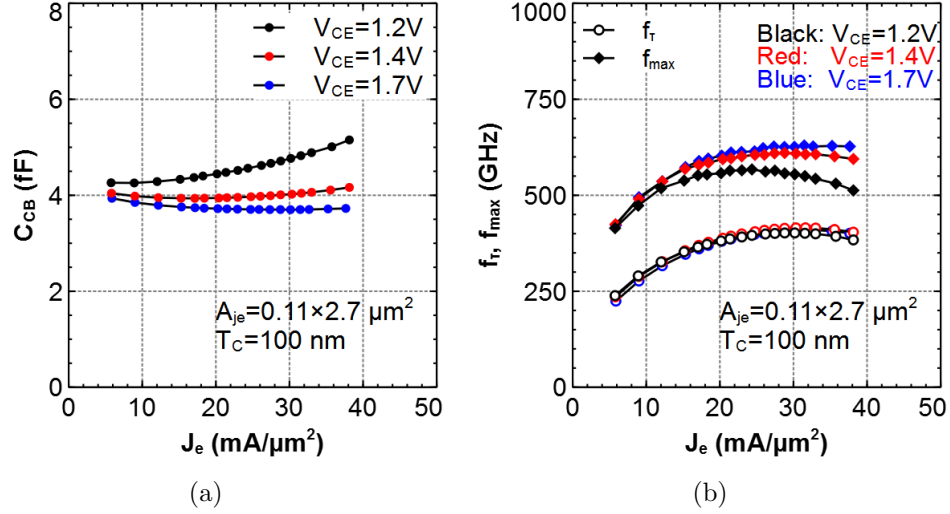


Figure 4.26: Current dependency of  $C_{CB}$  and cut-off frequencies extracted from the device on DHBT58H with  $W_{E,\text{design}} = 100 \text{ nm}$ ,  $W_{\text{BM},\text{design}} = 600 \text{ nm}$ , and  $L_{E,\text{design}} = 3 \mu\text{m}$  at  $V_{CE} = 1.2, 1.4, \text{ and } 1.7 \text{ V}$ . (a)  $C_{CB}$  vs.  $J_E$ . (b)  $f_T$  and  $f_{max}$  vs.  $J_E$

intercepts of the curves,  $C_{CB,\text{residual}}$  is  $0.69 \text{ fF}$ . From eq. 4.3, the excessive area beneath the base post ( $A_{BP}$ ) is approximately  $0.72 \mu\text{m}^2$  for devices with  $L_E = 2.7 \mu\text{m}$  and  $W_{\text{undercut}} = 50 \text{ nm}$ .

To estimate  $R_{B,\text{cont.}}$ , the contribution of  $R_{\text{BE},\text{spread}}$  and  $R_{\text{gap}}$  were calculated and then subtracted from  $R_{\text{BB}}$  extracted using the small-signal equivalent circuit model. The estimated  $R_{B,\text{cont.}}$  vs.  $W_{B,\text{cont.}}$  is plotted in fig. 4.27b. From TEM analysis, the base metal penetrated  $\sim 5 \text{ nm}$  below the B-E junction. Based on the sheet resistance from the pinched base TLM (fig. 4.19a),  $R_{\text{sh},B} \approx 903 \Omega/\square$  for metal penetration depth of  $4 \text{ nm}$ . By fitting  $R_{B,\text{cont.}}$  using this  $R_{\text{sh},B}$  value,  $\rho_{B,\text{cont.}}$  of the devices can be obtained. For device with  $L_E = 2.7 \mu\text{m}$ ,  $\rho_{B,\text{cont.}} = 16.4 \Omega - \mu\text{m}^2$ , which is higher than  $\rho_{B,\text{cont.}}$  obtained from base TLMs.

The power gain cut-off frequency ( $f_{\text{max}}$ ) is governed by the RC delay of the B-C mesa. For a given  $L_E$ ,  $C_{CB}$  reduces as the B-C mesa becomes narrower,

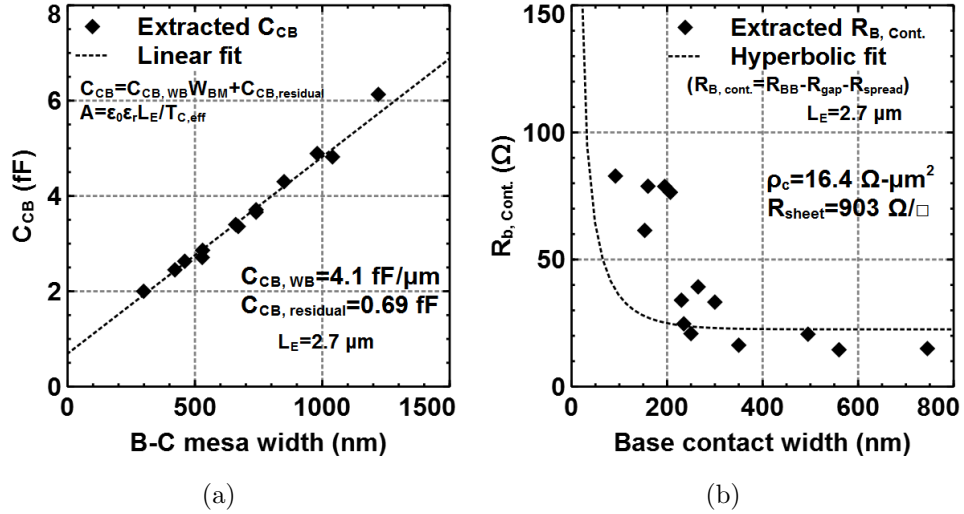


Figure 4.27: Dimension dependence of (a)  $C_{CB}$  (vs.  $W_{BM, design}$ ) and (b)  $R_{B, cont.}$  (vs.  $W_{B, cont.}$ ) from device on DHBT58H with  $L_E = 2.7 \mu\text{m}$  biased at  $V_{CE} = 1.7 \text{ V}$  and  $J_E = 25 \sim 30 \text{ mA}/\mu\text{m}^2$ .

whereas  $R_{BB}$  decreases when the mesa width increases. Thus, the width of the base contact  $W_{B, cont.}$  must be optimized according to the emitter width in order to achieve the highest possible  $f_{max}$ . Ideally, the optimal emitter/base contact width ratio is close to 1 if the parameters of devices follow the DHBT scaling rule in table. 2.1. However, since  $W_{E, actual}$  was overestimated during fabrication,  $W_{BM}$  is too wide, causing high  $C_{CB}$  and low  $f_{max}$ . This also explains why the highest  $f_{max}$  is measured from a device with wide emitter and narrow B-C mesa, where  $W_{E, actual} = 210 \text{ nm}$  and  $W_{B, Cont.} = 255 \text{ nm}$ .

## 4.4 Summary

The DC and RF characteristics of DHBT63B and DHBT58H have been reported. At  $W = 150 \text{ nm}$ , the DC- $\beta$  measured from DHBT63B and DHBT58H

are 16 and 18, respectively. On both samples, the current gain is limited by base current due to bulk recombination ( $I_{B,\text{bulk}}$ ) and edge conduction ( $I_{B,\text{edge}}$ ) [8, 9]. Detail analysis of the DC- $\beta$  and TCAD simulation will be addressed in the next chapter. For the RF performance,  $f_{\text{max}}$  measured from both sample are lower than 800 GHz. As discussed previously,  $f_{\text{max}}$  on DHBT63B and DHBT58H is limited by larger  $R_{\text{BB}}C_{\text{CB}}$  delay in the B-C mesa. Despite the cut-off frequencies is lower than the reported value of  $\sim 0.5/1.0$  THz [10, 11], the analysis on RF results provided some useful insight on reducing  $(RC)_{\text{eff}}$  in DHBTs, in which  $R_{\text{B,cont}}$  in a scaled device could deviate from the estimation from TLMs. Reducing the base specific contact resistivity will be the main limitation on the improvement of  $f_{\tau}/f_{\text{max}}$  in the future scaling generations DHBTs.



## References

- [1] S. A. Wartenberg, *RF Measurements of Die and Packages*. Artech House, 2002.
- [2] Technical Brief, “A Guide to Better Vector Network Analyzer Calibration for Probe-Tip Measurement,” tech. rep., Cascade Microtech.
- [3] Q. Li and K. Melde, “The Impact of On-Wafer Calibration Method on the Measured Results of Coplanar Waveguide Circuits,” *IEEE Trans. Adv. Packag.*, vol. 33, pp. 285–292, Feb. 2010.
- [4] Z. Griffith, *Ultra High Speed InGaAs / InP DHBT Devices and Circuits*. Ph.D. Thesis, University of California, Santa Barbara, Santa Barbara, Ca, U.S.A., 2005.
- [5] H. Hasegawa, “Fermi Level Pinning and Schottky Barrier Height Control at Metal-Semiconductor Interfaces of InP and Related Materials,” *Jpn. J. Appl. Phys.*, vol. 38, p. 10981102, Feb. 1999.
- [6] E. F. Chor, W. K. Chong, and C. H. Heng, “Alternative (Pd,Ti,Au) contacts to (Pt,Ti,Au) contacts for In<sub>0.53</sub>Ga<sub>0.47</sub>As,” *J. Appl. Phys.*, vol. 84, pp. 2977–2979, Sep. 1998.
- [7] V. Jain and M. J. W. Rodwell, “Transconductance Degradation in Near-THz InP Double-Heterojunction Bipolar Transistor,” *IEEE Electron Device Lett.*, vol. 32, pp. 1068–1070, Aug. 2011.
- [8] H. W. Chiang, J. C. Rode, P. Choudhary, and M. J. W. Rodwell, “Lateral Carrier Diffusion and Current Gain in THz InGaAs/InP DHBTs,” *J. Appl. Phys.*, vol. 115, p. 034513, Jan. 2014.
- [9] H. W. Chiang, J. C. Rode, P. Choudhary, and M. J. W. Rodwell, “Interfacial transport and current gain in InGaAs/InP DHBTs for THz applications,” in *72nd IEEE Device Research Conference*, Jun. 2014.
- [10] V. Jain, J. C. Rode, H. W. Chiang, A. Baraskar, E. Lobisser, B. J. Thibeault, M. J. W. Rodwell, M. Urteaga, D. Loubychev, A. Snyder, Y. Wu, J. M. Fastenau, and W. Liu, “1.0 THz  $f_{\max}$  InP DHBTs in a refractory emitter and self-aligned base process for reduced base access resistance,” in *69th IEEE Device Research Conference*, Jun. 2011.

## REFERENCES

---

- [11] M. Urteaga, R. Pierson, P. Rowell, V. Jain, E. Lobissor, and M. J. W. Rodwell, "130 nm InP DHBTs with  $f_{\tau} > 0.52$  THz and  $f_{\max} > 1.1$  THz," in *69th IEEE Device Research Conference*, Jun. 2011.

## Chapter 5

### DC Current Gain of DHBTs: TCAD Simulation

As mentioned in chapter 2, the DC current gain ( $\beta$ ) decreases as the DHBTs are scaled for higher cutoff frequencies. In order to increase DC- $\beta$  in the future scaling generations of DHBTs, the carrier transport in the base of a DHBT must first be understood. Using a commercially available TCAD simulator (Synopsys<sup>®</sup> Sentaurus), 2-D transport in the base region was simulated based on a drift-diffusion model. From the gradient of the carrier density, the magnitudes of current to each terminal of the DHBT were computed. DC- $\beta$  was calculated from  $I_B$  and  $I_C$  obtained at  $V_{CB}=0V$  and  $J_C \approx 25 \text{ mA}/\mu\text{m}^2$ , which is close to the current density for peak  $f_\tau$  and  $f_{\max}$  for DHBTs with the 70 or 100 nm collector designs [1, 2].

Discussed in chapter 2 and 4, we have shown that the inverse DC- $\beta$  can be written as

$$\begin{aligned} \frac{1}{\beta} &= \frac{1}{\beta_{\text{bulk}}} + \frac{K_{B,\text{edge}}.P_{\text{je}}}{J_C A_{\text{je}}} \\ &\approx \frac{1}{\beta_{\text{bulk}}} + \frac{K_{B,\text{edge}}}{2J_C W_E}, \end{aligned} \quad (5.1)$$

where  $J_C$  here is the collector current density at the base side of the collector. Because most of the current spreading occurs in the bulk collector region,  $J_C$  is associated with  $A_{\text{je}}$ . The approximation holds when  $L_E \gg W_E$ . The current gain due to bulk recombination,  $\beta_{\text{bulk}}$ , is obtained from the reciprocal of the intercept. The total sheet edge current density,  $K_{B,\text{edge}}$ , can be obtained from the product of  $J_C$  and the slope.

By comparing the DC- $\beta$  obtained from TCAD simulation and experimental devices, the model has been verified and the magnitudes of various base current components were assessed. The model shows that the DC- $\beta$  in scaled DHBTs is

governed by the base current due to Auger recombination and the lateral electron diffusion via the surface depletion region [3, 4].

In order to improve DC- $\beta$  in the scaled devices, several new designs of B-E junction were constructed in Sentaurus. Based on the 2-D transport model, the DC- $\beta$  in the designs were estimated. The simulation results indicate that DC- $\beta$  could be enhanced to 50~100 if the process flow for the new designs can be integrated into the DHBT fabrication.

## 5.1 Simulation Setup

The structure of THz DHBT has been described in the previous chapters. To simulate the 2-D transport in the base of DHBTs, the coupled continuity, drift-diffusion, and Poisson's equations need to be self-consistently solved for the full DHBT structure by Sentaurus. Because of the complicated collector designs of the DHBTs, numerical solution to the coupled equations is computationally demanding. However, the intention of the simulation is to determine the transport in the base and estimate DC- $\beta$  at  $J_C$  close to the bias condition for peak  $f_\tau$  and  $f_{\max}$ . At  $J_C < J_{C,\text{Kirk}}$ , i.e. before the base push-out occurs, the boundary condition of the coupled equations at the B-C junction depends only on the field in the setback region. The B-C grade and the InP collector designs have no effect on DC- $\beta$  at such  $J_C$ . Thus, the DC- $\beta$  of a DHBT and a single heterojunction bipolar transistor (SHBT), identical to the DHBT except without the complicated B-C grade and InP collector structures, are the same. Therefore, SHBTs

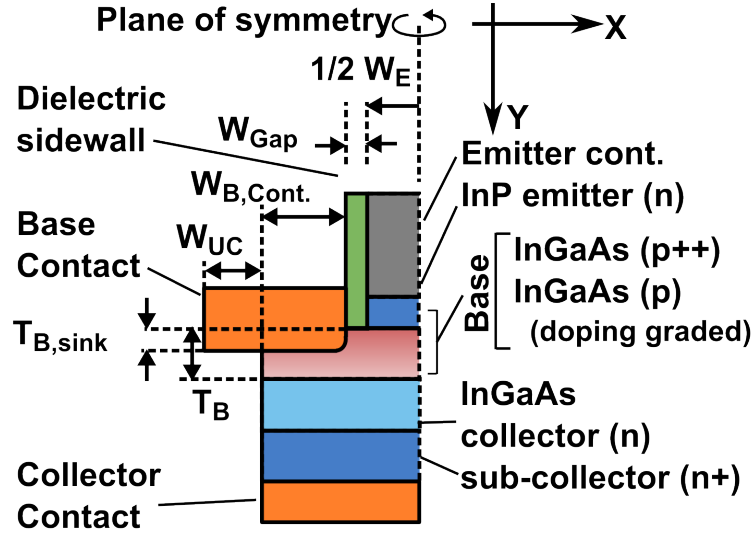


Figure 5.1: The cross-section of the SHBT structure simulated by Sentaurus.

structures were simulated by Sentaurus in order to construct a simplified and valid model for DC- $\beta$ . Fig. 5.1 depicts the SHBT structure simulated by Sentaurus. The dimensions defined for the SHBTs are identical to that for the DHBTs in chapter 2. According to TEM analysis,  $T_{b,sink}$  was assumed to be 5 nm for the simulation. For each design in epitaxy or geometry, devices with different  $W_E$  and  $W_{gap}$  have been simulated.  $W_E=75, 100, 125, 150, 175, 200, 225,$  and  $250$  nm, whereas  $W_{gap}=10, 15, 20, 25,$  and  $30$  nm. In addition to the  $2 \times 2$ -array of  $W_E$  and  $W_{gap}$ , for every emitter width, SHBTs devices with the base metal widths ( $W_{B,cont.} + W_{UC}$ ) of  $1.2, 1.4,$  and  $1.6 \times W_E$  were simulated. As a result, a total of 120 variants of SHBTs were simulated for every design.

In order to construct a valid model for the carrier transport in the base region using Sentaurus, correct physical models for band structure, mobility, recombination coefficient, etc., must be incorporated. The parameters in these critical models are either obtained from literature, or estimated based on reported values.

The physical models used in this work will be described in the following sections.

### 5.1.1 Carrier Mobility and Velocity Saturation

As the doping concentration increases, the carrier mobility decreases due to the increased impurity scattering [5]. The doping-dependent carrier mobility is usually extrapolated in the using empirical expression based on the Caughey-Thomas model [6]

$$\mu(N) = \frac{\mu_{\max} - \mu_{\min}}{1 + (N/N_{\text{ref},\mu})^\alpha} + \mu_{\min} , \quad (5.2)$$

where  $N$  is the doping concentration and  $\alpha$  is a fudging factor for the empirical formula.  $N_{\text{ref},\mu}$  is a reference (low) doping concentration. Eq. 5.2, implies that  $\mu_{\min}$  and  $\mu_{\max}$  are the minimum and maximum mobilities at high and low doping concentrations, respectively. At very high doping concentration, where  $N \gg N_{\text{ref},\mu}$ ,  $\mu(N)$  reduces to  $\mu_{\min}$ . In our simulation,  $N_{\text{ref},\mu}$  was set to the conduction-band effective density of states,  $N_C$ . The simulations assumed  $\mu_{\min}$  and  $\mu_{\max}$  of 1600 and 11600 cm<sup>2</sup>/V – s for electrons in p-InGaAs. For holes in p-InGaAs, the values were assumed to be 75 and 331 cm<sup>2</sup>/V – s. The factor  $\alpha$  for electrons and holes are 0.76 and 1.37, respectively [7, 8].

Velocity saturation occurs when the carriers are under either high electric fields or large diffusion gradients. In the composition- or doping-graded InGaAs base, the mobility of the injected electrons drops rapidly as the velocity saturation takes place [9]. The mobility under high field was modelled according to  $v_{\text{drift}} =$

$\mu_{\text{highfield}} F$ , where [10]

$$\mu_{\text{highfield}} = \frac{\mu_{\text{lowfield}}}{\left(1 + \left(\frac{\mu_{\text{lowfield}} F}{v_{\text{th}}}\right)^\gamma\right)^{1/\gamma}}, \quad (5.3)$$

where  $F = q^{-1} \nabla E_{\text{fn}}$  is the driving force exerted upon the electrons due to the gradient in  $E_{\text{fn}}$ , the electron quasi-Fermi level. The electron threshold velocity,  $v_{\text{th}}$  was assumed to be  $\sim 3 \times 10^7$  cm/s, and  $\gamma$  was set to 10 to ensure a rapid transition from low-field to high-field mobility, as is observed in the InGaAs material system [9].

### 5.1.2 Band Structure

It is imperative to have the correct conduction-band profile in order to simulate the electron transport in DHBTs. The current gain due to bulk recombination is determined by the electron lifetime and the base transit time, i.e.  $\beta_{\text{bulk}} = \tau_{\text{n,total}} / \tau_{\text{B}}$ , where  $\tau_{\text{n,total}}$  and  $\tau_{\text{B}}$  have been given in chapter 2 as [11]

$$\tau_{\text{B}} = \frac{T_{\text{B}}^2}{D_{\text{n}}} \frac{kT}{\Delta E_{\text{C}}} \left[1 - \frac{kT}{\Delta E_{\text{C}}} (1 - \exp(-\frac{\Delta E_{\text{C}}}{kT}))\right] + \frac{T_{\text{B}}}{v_{\text{exit}}} \frac{kT}{\Delta E_{\text{C}}} (1 - \exp(\frac{\Delta E_{\text{C}}}{kT})), \quad (5.4)$$

and

$$\tau_{\text{n,total}} = \left(\frac{1}{\tau_{\text{Auger}}} + \frac{1}{\tau_{\text{SRH}}} + \frac{1}{\tau_{\text{rad.}}}\right)^{-1}. \quad (5.5)$$

Hence,  $\beta_{\text{bulk}}$  is affected by  $\Delta E_{\text{C}}$ , the difference in the conduction-band energy between the top and the bottom the base. The value of  $\Delta E_{\text{C}}$  is determined by the band gap energy ( $E_{\text{g}}$ ), the magnitude of the band gap narrowing (BGN) effect [12],



as well as the effective density of states ( $N_C$  and  $N_V$ ) of InGaAs. Most of the parameters can be found in an on-line database [13] or a semiconductor simulation handbook [14]. However, these values are usually obtained from a lattice matched or relaxed (low mechanical strain) semiconductors, which is not the case for the heavily doped p-InGaAs base. At high carbon doping concentration, the lattice constant of InGaAs changes due to the discrepancy in the atomic radii between As and C. In addition, the C source is  $\text{CBr}_4$ , and Br preferentially etch In during the MBE growth, changing the In/Ga ratio. As a result, the lattice contracts as doping concentration increases [15], causing strain in InGaAs. To minimize the lattice mismatch between InP and InGaAs, during the base growth of UCSB DHBT wafers, In/Ga ratio was adjusted in order to grow lattice-matched InGaAs doped at the median of the doping concentrations, e.g.  $7 \times 10^{19} \text{ cm}^{-3}$  for the doping grade from 9 to  $5 \times 10^{19} \text{ cm}^{-3}$ . Even with this adjustment, the varying doping concentration still results in some extend of lattice mismatch so the InGaAs base of DHBTs is strained.

Therefore, the actual In/Ga ratio and strain in the InGaAs base is unknown, and determining the exact value of the band structure parameters would be difficult. This render the evaluation of  $\Delta E_C$  very challenging. Instead of choosing the right parameters for the correct  $\Delta E_C$ , different  $\Delta E_C$  are generated by tuning the parameters. The simulated  $\beta_{\text{bulk}}$  and  $\tau_B$  are then compared with the experimental result in order to determine the plausible conduction band profile. The  $E_g$  of InP and InGaAs were assumed to be 1.42 and 0.72 eV, respectively. For InP,  $N_{C,\text{InP}}$  and  $N_{V,\text{InP}}$  were set to be  $5.66 \times 10^{17}$  and  $2.03 \times 10^{19} \text{ cm}^{-3}$ , respectively. For InGaAs,  $N_{C,\text{InGaAs}}$  and  $N_{V,\text{InGaAs}}$  were assumed to be  $2.54 \times 10^{17}$  and  $7.51 \times 10^{18} \text{ cm}^{-3}$ . The

resulting  $\Delta E_C$  varies according to the base design, which will be discussed in the next section.

The built-in voltage ( $V_{bi}$ ) of the B-E diode depends on the conduction band energy offset,  $\Delta E_{C,offset}$ ,  $G_{g,InGaAs}$ , and  $E_{fp}$ , the hole quasi Fermi level. Inaccurate parameters result in wrong  $V_{bi}$ , shifting the I-V curve in the Gummel plot horizontally. Similar to the estimation of  $\Delta E_C$ , the uncertainty in the In/Ga ratio and lattice strain causes difficulty in determining the correct  $V_{bi}$ , and hence error in computing  $\beta$  as a function of  $V_{BE}$ . Therefore,  $\beta$  is evaluated as a function of  $J_C$ . The simulation and the experimental results are compared at the same  $J_C$ .

Experimentally,  $\Delta E_{C,offset} = 0.3 \sim 0.4 \Delta E_{g,offset}$  for InGaAs/InP heterojunction [16]. In our simulation,  $\Delta E_{C,offset}$  is set to  $\sim 0.28$  eV. Sentaurus assumes a continuous vacuum level and computes the offset from the difference in electron affinities between InGaAs and InP,  $\chi_{InGaAs} - \chi_{InP}$ . The values reported in the literatures are  $\chi_{InGaAs} \approx 4.5$  eV and  $\chi_{InP} \approx 4.4$  eV [13]. To attain  $\Delta E_{C,offset} 0.28$  eV, a pseudo  $\chi_{InGaAs}$  of 4.68 eV was used.

### 5.1.3 Carrier Recombination

Three recombination mechanisms in bulk InGaAs base were incorporated into the simulation for  $\beta$ : Auger, Shockley-Read-Hall (SRH), and radiative recombination. The total electron lifetime are obtained from eq. 5.5. Of the three mechanisms, Auger recombination is the governing process. Thus, accurate Auger coefficients,  $C_n$  and  $C_p$  is crucial to the simulation. From eq. 2.18, the Auger re-

combination rate can be written as

$$R_{\text{Auger}} = C_{\text{Auger},n}n^2p + C_{\text{Auger},p}np^2 . \quad (5.6)$$

As discussed in chapter 2,  $C_{\text{Auger},n}$  is associated with the CCCH process and  $C_{\text{Auger},p}$  is related to the CHHL and the CHHS proces [17, 18]. Most value reported in the literature are the combination of  $C_{\text{Auger},n}$  and  $C_{\text{Auger},p}$  since they were measured under ambipolar injection (such as laser diodes), where  $n = p$ . The reported  $C_{\text{Auger},n} + C_{\text{Auger},p}$  scatters from  $3.6$  to  $9 \times 10^{-29}$   $\text{cm}^6/\text{s}$  [14, 19, 20]. In the heavily doped DHBT base, only the electron are injected, i.e.  $p \gg n$ , and CHHS/CHHL processes dominates. Therefore, knowing the value for  $C_{\text{Auger},p}$  is necessary. However, there are only few reports revealing the separated value so an adequate value of  $C_{\text{Auger},p}$  for the simulation is unknown. Similar to the solution to the problem in determining  $\Delta E_C$ ,  $C_{\text{Auger},p}$  were first assumed to be an arbitrary value and then tuned to fit  $\tau_{\text{Auger}}$  and  $\beta_{\text{bulk}}$ . The  $C_{\text{Auger},p}$  value of  $3.8 \times 10^{-29}$   $\text{cm}^6/\text{s}$  was reported by [14] and used as a starting point for the simulations. Certain value of  $C_{\text{Auger},n}$  was also required by the simulation. Nevertheless, since the effect of the CCCH process can be neglected, we assumed  $C_{\text{Auger},n} = C_{\text{Auger},p}$ .

As described in chapter 2, the radiative recombination rate has a coefficient,  $C_{\text{rad}}$ . The simulation assumed  $C_{\text{rad}} = 9.6 \times 10^{-11}$   $\text{cm}^3/\text{s}$  in InGaAs [21]. As mentioned in chapter 2, the doping-dependent lifetime due to the SRH recombination is (eq. 2.21)

$$\tau_{\text{SRH}}(N_A + N_D) = \frac{\tau_{\text{ref}}}{1 + \left(\frac{N_A + N_D}{N_{\text{ref},\tau}}\right)^\kappa}, \quad (5.7)$$

where the reference doping concentration,  $N_{\text{ref},\tau}$  is  $1 \times 10^{19} \text{ cm}^{-3}$  for both holes and electrons. The simulation assumed the electron lifetime,  $\tau_{\text{ref},n} = 50/\text{ps}$ , and the hole lifetime,  $\tau_{\text{ref},p} = 400/\text{ps}$ . The factor  $\kappa$  was 0.73 for electrons and 1.2 for holes [7].

### 5.1.4 Surface Conduction and Recombination

At the p-InGaAs/dielectric interface on the extrinsic base region, the surface Fermi level is pinned by the trap states, inducing a surface depletion region. The electrons injected from the emitter could be trapped in the depletion region and leads to surface conduction or recombination. To emulate the surface depletion region, trap states were added to the interface between p-InGaAs and dielectric. The energy distribution of the state is assumed to be a Gaussian function centered at  $E_0 = 0.5 \text{ eV}$  above the valence band edge [22], and with the standard deviation,  $E_S$ , of  $0.1 \text{ eV}$ . The density of the trap states,  $D_{\text{it}}$ , is usually obtained from C-V measurements at various frequencies. However, because the extrinsic base has witnessed most of the DHBT process flow starting from base metalization, the surface quality of p-InGaAs is unknown. The actual value of  $D_{\text{it}}$  on the extrinsic base would differ from the values obtained from the C-V measurements. Therefore, DC- $\beta$  simulated at different values of  $D_{\text{it}}$  were computed. By fitting the simulation results to the experimental data, the correct  $D_{\text{it}}$  can be determined.

The surface recombination velocity,  $v_{\text{surf.rec.}}$ , also depends on the InGaAs surface quality. For an InGaAs surface terminated by native oxide, values of  $10^3 \sim 10^4 \text{ cm/s}$  have been reported [23]. However, similar to  $D_{\text{it}}$ , it is difficult to

assess the accurate value of  $v_{\text{surf.rec.}}$  on the extrinsic base surface. However, it has later been discovered from the simulation vs. experimental results (section 5.2) that even at high  $v_{\text{surf.rec.}}$  ( $10^4$  cm/s), the surface recombination current is negligible when comparing with lateral diffusion current. Thus,  $v_{\text{surf.rec.}}$  were assumed to be 5000 cm/s.

The parameters for InGaAs assumed in the simulation and their references are listed in table. 5.1.

Parameter	Carrier Type		unit
	Electrons	Holes	
Carrier Mobility			
$\mu_{\text{min}}$ [7,8]	1600	75	$\text{cm}^2/\text{V} - \text{s}$
$\mu_{\text{max}}$ [7,8]	11600	331	$\text{cm}^2/\text{V} - \text{s}$
$N_{\text{ref},\mu}$ [7,8]	$2.1 \times 10^{17}$	$7.7 \times 10^{18}$	$\text{cm}^{-3}$
$\alpha$ [7,8]	0.76	1.37	
$\gamma$	10	10	
SRH Recombination			
$\tau_{\text{ref}}$ [7]	50	400	ps
$N_{\text{ref},\tau}$ [7]	$1 \times 10^{19}$	$1 \times 10^{19}$	$\text{cm}^{-3}$
$\kappa$ [7]	0.73	1.2	
Auger Recombination			
$C_{\text{Auger}}$ [14,19,20]	$2.5 \sim 4 \times 10^{-29}$	$2.5 \sim 4 \times 10^{-29}$	$\text{cm}^6/\text{s}$
Radiative Recombination			
$C_{\text{rad.}}$ [21]	$9.6 \times 10^{-11}$		$\text{cm}^3/\text{s}$
Surface Recombination Velocity			
$v_{\text{surf.rec.}}$ [23]	$5 \times 10^3$		cm/s

Table 5.1: In<sub>0.53</sub>Ga<sub>0.47</sub>As parameter values used in simulation and corresponding references. The coefficients for Auger recombination are usually reported as a combined value.

## 5.2 Simulation and Experimental Results

As described in the previous section, the parameters regarding the band structure, Auger recombination coefficient, and the density of the interface trap states were unknown when constructing the trnspot model in the DHBT base. In order to determine these parameters, DC- $\beta$  was computed from several sets of simulation results assuming different parameter values. The calculated DC- $\beta$  were then compared with the DC- $\beta$  measured from the experimental device with the same B-E junction design. The experimental results from two DHBT samples with different base designs, DHBT63B and DHBT58H, were used to establish the model. The inverse DC- $\beta$  vs. B-E junction periphery to area ratio ( $P_{je}/A_{je}$ ) measured from two samples are shown in fig. 5.2.

### 5.2.1 Bulk Recombination and Lateral Diffusion Current

First, we would like to assess  $\Delta E_C$ , and  $C_{Auger,p}$ . The values of  $\Delta E_C$  and  $C_{Auger,p}$  affect  $\tau_B$  and  $\tau_{n,total}$ , respectively. The ratio of  $\tau_{n,total}$  to  $\tau_B$  is the current gain due to the bulk recombination,  $\beta_{bulk}$ , which is the reciprocal of the y-axis intercepts in fig. 5.2. By fitting the computed  $\beta_{bulk}$  to the experimental  $\beta_{bulk}$ , is adequate  $\Delta E_C$  and  $C_{Auger,p}$  are determined. In order to focus on  $\Delta E_C$  and  $C_{Auger,p}$  only, the surface recombination and conduction were ignored, i.e. no surface depletion region and  $v_{surf.rec.}$  cm/s. This is done by removing the dielectric sidewall from the simulated structures.

The result from DHBT58H was analyzed first, which has the design of 20 nm

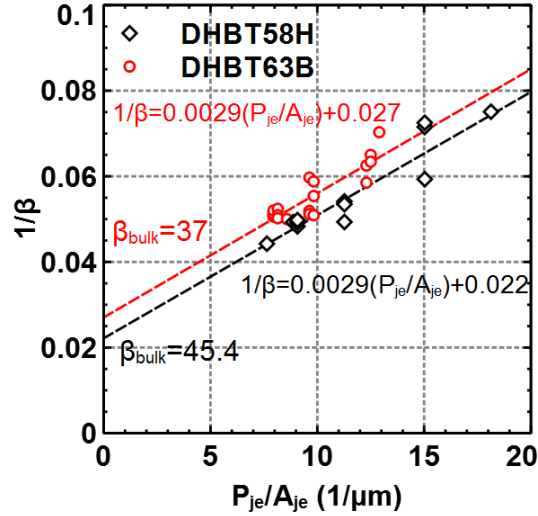


Figure 5.2: Inverse DC current gain ( $1/\beta$ ) vs. HBT emitter periphery to area ratio ( $P_{je}/A_{je}$ ) of DHBT58H and DHBT63B at  $J_E \approx 25\text{mA}/\mu\text{m}^2$ . DHBT58H employs a 20 nm base with doping concentration of  $12\text{-}8 \times 10^{19}\text{ cm}^{-3}$  varying from the emitter side to the collector side. DHBT63B has a 25 nm base with lower doping concentration varying from  $9\text{ to }5 \times 10^{19}\text{ cm}^{-3}$ . For both samples  $W_{\text{gap}} \approx 10\text{ nm}$  according to TEM analysis.

base doping-graded from  $1.2 \times 10^{20}\text{ cm}^{-3}$  at the emitter side to  $8 \times 10^{19}\text{ cm}^{-3}$  at the collector side. Three magnitude of  $\Delta E_C$ : 0, 26, and 54 meV were assumed. The value 54 meV was obtained from the conduction-band profile of the base ignoring the BGN effect, whereas the values of 0 and 26 meV were simulated under extreme and moderate BGN effects, respectively. With the three conduction-band profiles of the base, DC- $\beta$  were computed assuming the literature value,  $C_{\text{Auger,p}} = 3.8 \times 10^{-29}\text{ cm}^6/\text{s}$  [14].

However, the  $\beta_{\text{bulk}}$  estimated from all three simulation sets were lower than the experimental value of 45.4, indicating that either  $\tau_B$  was overestimated or  $\tau_{n,\text{total}}$  is underestimated. Since a shorter  $\tau_B$  would require a higher  $\Delta E_C$ , which is unlikely to be generated from the designed doping-grade, we deduced that actual

$\tau_{n,total}$  should be higher. In order to increase  $\tau_{n,total}$ , the assumed  $C_{Auger,p}$  needed to be reduced. The subsequent attempts assumed the same band profiles and  $C_{Auger,p} = 2.5 \times 10^{-29} \text{ cm}^6/\text{s}$ . The computation results are plotted in fig. 5.3 [3]. The  $\beta_{bulk}$  simulated at  $\Delta E_C=0, 26,$  and  $54 \text{ meV}$  are 27.3, 36, and 43, respectively. The results from  $C_{Auger,p} = 2.5 \times 10^{-29} \text{ cm}^6/\text{s}$  and  $\Delta E_C=54 \text{ meV}$  agrees with the experimental value of 45.4. It should be noted that with a even lower  $C_{Auger,p}$ , the  $\beta_{bulk}$  simulated with lower  $\Delta E_C$  (considering the BGN effect) would also fit the experimental  $\beta_{bulk}$ . However, simulations assuming such  $C_{Auger,p}$  which greatly deviates from the reported value could be invalid. Hence, we refrained from further decreasing  $C_{Auger,p}$ , and assumed  $C_{Auger,p} = 2.5 \times 10^{-29} \text{ cm}^6/\text{s}$  and no BGN effect.

As shown in fig. 5.3c, only the intercept, i.e.  $\beta_{bulk}$ , matches the experimental result. The slope of the computed and experimental  $1/\beta$  are not consistent because the lateral carrier diffusion ( $I_{B,diff.}$ ) was the only edge current component considered in the simulations and the effect of surface recombination ( $I_{B,surf.rec.}$ ) and conduction ( $I_{B,surf.rec.}$ ) was neglected. In other words, the slope of the computed current gain is solely due to  $I_{B,diff.}$ . According to fig. 5.3c, the slopes of the simulation results corresponding to  $W_{gap}=10$  and  $30 \text{ nm}$  indicate  $K_{B,edge}=23.6$  and  $4.7 \mu\text{A}/\mu\text{m}$ , respectively. In the simulations,  $K_{B,edge}$  is essentially  $K_{B,diff.}$ , which means the lateral diffusion current via the bulk base current increases 5 times when  $W_{gap}$  is scaled from 30 to 10 nm.

The experimental  $K_{B,edge}$  of DHBT58H is  $\sim 72 \mu\text{A}/\mu\text{m}$  at  $J_C \approx J_E = 25 \text{ mA}/\mu\text{m}^2$ . From TEM analysis,  $W_{gap} \approx 10 \text{ nm}$  in experimental devices. Therefore, assuming the simulation result with  $W_{gap}=10 \text{ nm}$  is a valid model for the transport in the



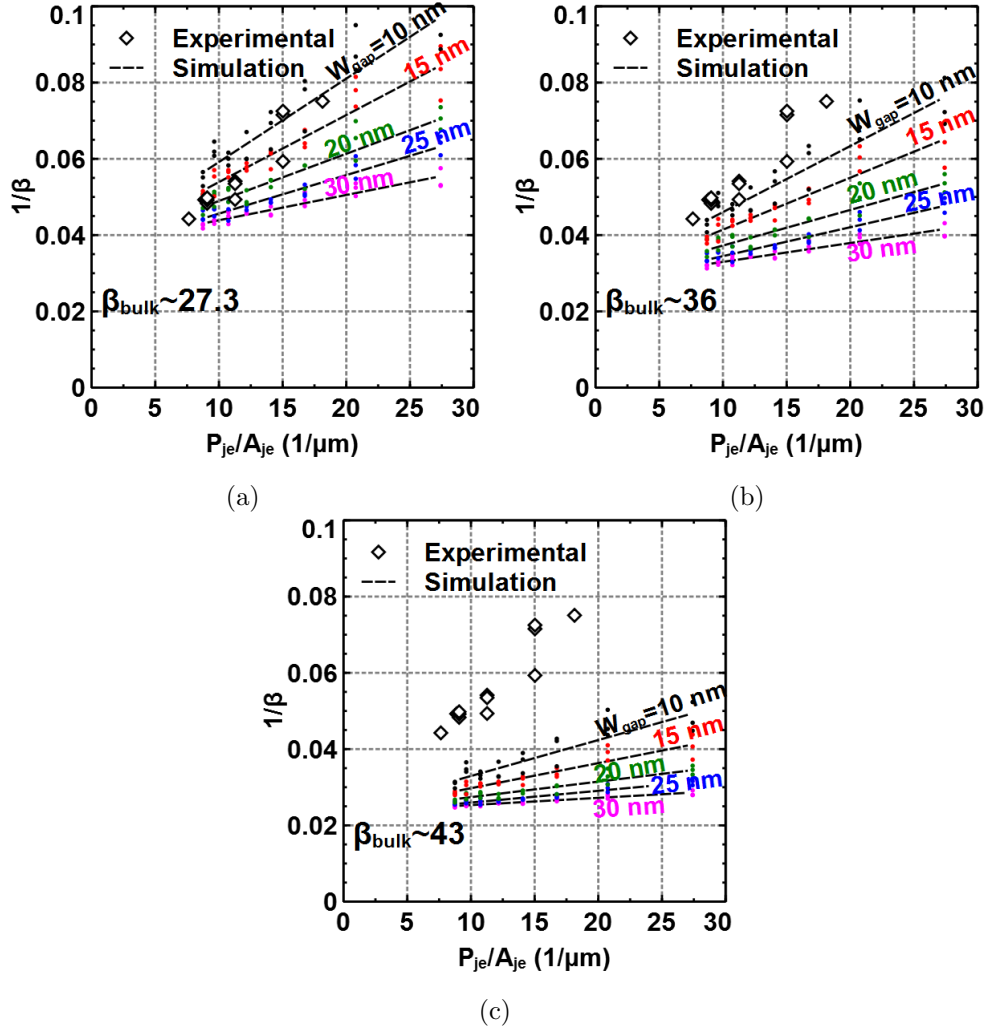


Figure 5.3: Experimental and computed inverse DC current gain ( $1/\beta$ ) vs. HBT emitter periphery to area ratio ( $P_{je}/A_{je}$ ) of DHBT58H at  $J_E \approx 25\text{mA}/\mu\text{m}^2$ . The simulation assumed  $\Delta E_C$  of (a) 0 (b) 26, and (c) 54 meV.

bulk base region,  $K_{B,diff}$  is approximately 33% of the total edge current in DHBTs. For an experimental device with  $W_E=100$  nm,  $DC-\beta \approx 13$ . For such device, the simulated  $\beta_{bulk}$  and  $K_{B,diff}$  implies that  $I_{B,bulk}$  and  $I_{B,diff}$  account for 30 and 24% (two sides of B-E junction considered) of the total base current, respectively.

## 5.2.2 Surface Recombination and Conduction Current

With adequate values of  $\Delta E_C$  and  $C_{Auger,p}$  known, we would like to estimate  $v_{surf.rec.}$  and  $D_{it}$  on the extrinsic base surface. The value of  $D_{it}$  affects the magnitude of surface depletion and  $v_{surf.rec.}$ , and hence governs both  $I_{B,surf.rec.}$  and  $I_{B,surf.cond.}$ . To simulate transport with the presence of a surface depletion region, the dielectric sidewall was added back into the simulation structure, and donor-like trap states were introduced at the InGaAs/dielectric interface. The energy distribution of the states were assumed to be a Gaussian as described in section 5.1.4. The trap states density can be written as a function of energy,

$$D(E) = D_{it} \exp\left(-\frac{(E - E_0)^2}{2E_s^2}\right), \quad (5.8)$$

where  $E$  is the energy with respect to the valence band, i.e.  $E = 0$  at the valence-band edge.  $E_0$  and  $E_s$  were assumed to be 0.5 and 0.1 eV, respectively. In other words,  $D(E)$  is a Gaussian function with a peak value of  $D_{it}$  at 0.5 eV above the valence band edge [22] with a standard deviation of 0.1 eV.  $E_s$  was chosen arbitrarily to be 0.1 eV to ensure most of the trap states are within  $\pm 0.1$  eV from  $E_0$ . Since the value of  $D_{it}$  is unknown, arbitrary numbers had to be assumed at first,

and then the computed current gains were compared with the experimental values. To focus on  $D_{it}$  only,  $v_{surf.rec.}$  was assumed to be 5000 cm/s and independent of  $D_{it}$ . We later discovered that  $I_{B,surf.rec.}$  is smaller than  $I_{B,surf.cond.}$  by few orders. Thus, assessing the correct value of  $v_{surf.rec.}$  is not as critical as that of  $D_{it}$ . We will address this shortly in the remainder of this section.

Once again the structure of DHBT58H was used in the simulations. The simulations assumed  $\Delta E_C=54$  meV and  $C_{Auger,p} = 2.5 \times 10^{-29}$  cm<sup>6</sup>/s according to result reported in the previous section. DC- $\beta$  were computed assuming different  $D_{it}$  of  $5 \times 10^{12}$ ,  $10^{13}$ , and  $5 \times 10^{13}$  cm<sup>-2</sup>eV<sup>-1</sup>. The simulation result shown in fig. 5.3c was used as a control neglecting both  $D_{it}$  and  $v_{surf.rec.}$ . Each simulation result was then compared with the DC- $\beta$  obtained experimentally to determine the correct  $D_{it}$ . The results are depicted in fig. 5.4 [4]. From  $J_C$  ( $\sim 25$  mA/ $\mu$ m<sup>2</sup>) and the slope of  $1/\beta$  vs.  $P_{je}/A_{je}$  at  $W_{gap}=10$  nm,  $K_{B,edge}=39, 42,$  and  $59$   $rm\mu A/\mu m$  when assuming  $D_{it}=5 \times 10^{12}, 10^{13},$  and  $5 \times 10^{13}$  cm<sup>-2</sup>eV<sup>-1</sup>, respectively. Among these three sets of simulations, the one assuming  $D_{it}=5 \times 10^{13}$  cm<sup>-2</sup>eV<sup>-1</sup> showed the result closest to the experimental data.

Simulations assuming a higher  $D_{it}$  would give a  $K_{B,edge}$  that matches the experimental value,  $72 \mu A/\mu m$ . Although the  $D_{it}$  at the Al<sub>2</sub>O<sub>3</sub>/InGaAs interface in the extrinsic base of DHBT58H is expected to be high because no surface treatment was performed before ALD, the  $D_{it}$  of  $5 \times 10^{13}$  cm<sup>-2</sup>eV<sup>-1</sup> is already more than an order higher than the value reported for the Al<sub>2</sub>O<sub>3</sub>/InGaAs interface with surface treatment prior to ALD [24, 25]. Therefore, assuming higher values of  $D_{it}$  could be invalid and misleading.

Moreover, the emulation of the surface depletion region might not be entirely

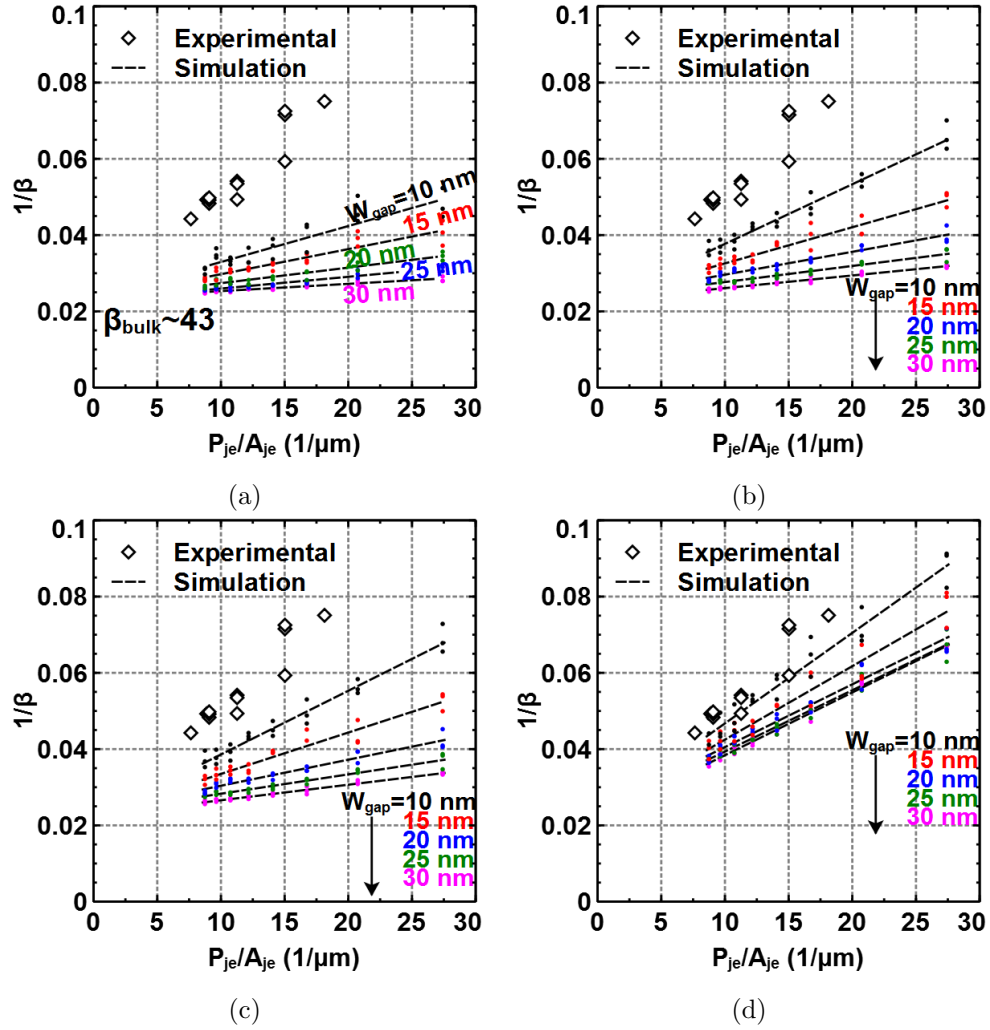


Figure 5.4: Experimental and computed inverse DC current gain ( $1/\beta$ ) vs.  $P_{je}/A_{je}$  of DHBT58H at  $J_E \approx 25\text{mA}/\mu\text{m}^2$ . In (a), the simulation assumed zero  $D_{it}$  and  $v_{surf.rec.}$ . In the rest of the figures, The simulation assumed  $v_{surf.rec.}=5000\text{cm/s}$  and  $D_{it}$  of (b)  $5 \times 10^{12}$ , (c)  $1 \times 10^{13}$ , and (d)  $5 \times 10^{13}\text{cm}^{-2}\text{eV}^{-1}$ .

accurate since it used a classical model to describe the trapped electrons. In the classic model, the trapped electrons has a continuous energy distribution, and cannot escape from the depletion region once trapped. In a more accurate Quantum Mechanic model, the electrons are trapped in discrete bound states in the triangular quantum well (QW) near the interface induced by the surface Fermi level pinning. The electrons could either travel laterally in the QW like in the classic model, or tunnel through the QW barrier and return to the bulk base region again. Thus, the electron population in the triangular QW and a finite trapping time should be incorporated into the simulation. Simulations involving the aforementioned Quantum Mechanic model requires a demanding computational effort. Nonetheless, the goal of this work is to construct a simple model/tool to estimate DC- $\beta$  in DHBTs, and then use the model as a quick-test platform to help designing B-E junction for improved  $\beta$ . Because of this intention, the Quantum Mechanic model is not considered in this work. Hence, a perfect match between the simulated vs. experimental surface recombination and conduction current should not be expected

The current components due to surface recombination and conduction,  $K_{B,\text{surf.rec.}}$  and  $K_{B,\text{surf.cond.}}$ , can be estimated from the difference between  $K_{B,\text{edge}}$  obtain from simulations with and without the surface depletion region. The simulation result with  $W_{\text{gap}}=10$  nm and  $D_{\text{it}}=5\times 10^{13}$  cm<sup>-2</sup>eV<sup>-1</sup> indicates  $K_{B,\text{surf.rec.}} + K_{B,\text{surf.cond.}}$  is  $35.4 \mu\text{A}/\mu\text{m}$ , which accounts for  $\sim 50\%$  of the total  $K_{B,\text{edge}}$  of  $72 \mu\text{A}/\mu\text{m}$  measured from DHBT58H.  $K_{B,\text{edge}}$  of  $59 \mu\text{A}/\mu\text{m}$  also implies that the total edge current contributes  $\sim 61\%$  (two sides of B-E junction considered) of the total base current in an experimental device with  $W_{\text{E}}=100$  nm and  $W_{\text{gap}}=10$  nm.

Next, we would like to determine the magnitudes of  $K_{B,\text{surf.rec.}}$  and  $K_{B,\text{surf.cond.}}$  separately. From chapter 2, the surface recombination rate can be written as

$$R_{\text{surf.SRH}} = n_s(x)v_{\text{surf.rec.}} , \quad (5.9)$$

where  $n_s(x)$  is the density of the electrons trapped at the vicinity of the InGaAs/dielectric interface. Fig. 5.5 is the electron density near the InGaAs/dielectric interface as a function of the depth into the base.  $n_s(x)$  was defined as the average electron density within an arbitrary distance,  $T_s$ . By integrating  $n_s(x)v_{\text{surf.rec.}}$  over the extrinsic base, the edge sheet current density due to surface recombination could be calculated, i.e.

$$K_{B,\text{surf.rec.}} = \int_{W_E}^{W_E+W_{\text{gap}}} n_s(x)v_{\text{surf.rec.}} dx . \quad (5.10)$$

Assuming  $v_{\text{surf.rec.}}=5000$  cm/s, the estimated  $K_{B,\text{surf.rec.}}$  is less than  $1 \mu\text{A}/\mu\text{m}$  for device with  $W_{\text{gap}}=10$  to 30 nm. The magnitude approximately doubles if  $v_{\text{surf.rec.}}=5000$  cm/s is assumed. This implies that  $K_{B,\text{surf.rec.}}$  is negligible with respect to  $K_{B,\text{surf.cond.}}$  so almost the entirety of edge current originates from lateral diffusion via bulk ( $I_{B,\text{diff.}}$ ) and surface depletion region  $I_{B,\text{surf.cond.}}$ .

### 5.2.3 Model Verification

The transport model has been constructed for DHBT. In order to verify the model, the experimental result of DHBT63B, which has a 25 nm base doping-graded from  $9$  to  $5 \times 10^{19} \text{ cm}^{-3}$ . Unlike DHBT58H, DHBT63B does not have com-

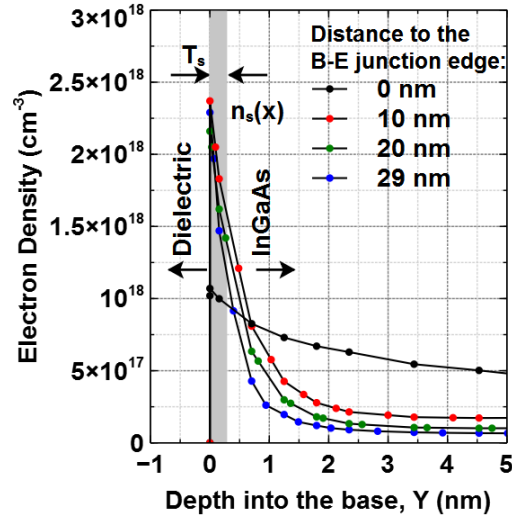


Figure 5.5: The computed electron density near the dielectric/InGaAs interface vs. the depth into the base, at different distance to the edge of the B-E junction. The simulation is based on the base design of DHBT58H with  $W_{\text{gap}}=30$  nm and assumed  $D_{\text{it}}=5 \times 10^{13} \text{ cm}^{-2} \text{ eV}^{-1}$ .

posite  $\text{Al}_2\text{O}_3/\text{SiN}_x$  sidewall. The simulation for DHBT63B retained the assumption used in the simulations for DHBT58H: the BGN effect has been neglected,  $C_{\text{Auger,p}}=2.5 \times 10^{-29} \text{ cm}^6/\text{s}$ ,  $D_{\text{it}}=5 \times 10^{13} \text{ cm}^{-2} \text{ eV}^{-1}$ , and  $v_{\text{surf.rec.}}=5000 \text{ cm/s}$ . The computed  $\beta$  gave a matching  $K_{\text{B,edge}}$ , but the calculated  $\beta_{\text{bulk}}$  is higher than the experimental value of 37, indicating that the electron lifetime was too long. Therefore,  $C_{\text{Auger,p}}$  was increased back to the literature value of  $4 \times 10^{-29} \text{ cm}^6/\text{s}$ . Fig. 5.6 is the experimental and simulated  $1/\beta$  vs.  $P_{\text{je}}/A_{\text{je}}$ , showing a consistent simulation and experimental results for  $W_{\text{gap}}=10$  nm. Nonetheless, the reason for the discrepancy between  $C_{\text{Auger,p}}$  of DHBT58H and DHBT63B remains unknown. It is possible that the simulation ignored other recombination mechanisms occurring in the base.

Whether with or without the  $\text{Al}_2\text{O}_3/\text{SiN}_x$  sidewall, the simulation results of

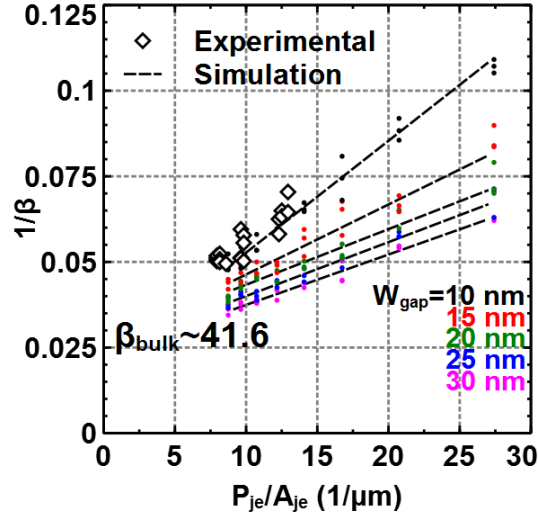


Figure 5.6: Experimental and computed inverse DC current gain ( $1/\beta$ ) vs.  $P_{je}/A_{je}$  of DHBT63B design at  $J_E \approx 25\text{mA}/\mu\text{m}^2$ . The simulation assumed  $v_{\text{surf.rec.}}=5000\text{ cm/s}$ ,  $D_{\text{it}}=5\times 10^{13}\text{ cm}^{-2}\text{eV}^{-1}$ ,  $C_{\text{Auger,p}} = 4\times 10^{-29}\text{ cm}^6/\text{s}$ , and ignored the BGN effect.

DHBT58H and DHBT63B both indicate high  $D_{\text{it}}$  on the p-InGaAs surface. This implies that  $\text{Al}_2\text{O}_3$  on the extrinsic base of DHBT58H has not adequately passivated/terminated the InGaAs surface, causing similar amount of surface trap states. In order to suppress the surface conduction current,  $D_{\text{it}}$  must be lowered. Low  $D_{\text{it}}$  at the interface between ALD dielectric and InGaAs has been achieved for III-V MOSFET application [24, 25]. This often involves a surface treatment techniques prior to ALD and/or an annealing after ALD. However, the hydrogen-trimethylaluminium (TMA) cycles reported in [25] is incompatible with DHBT process since the hydrogen plasma will react with the carbon dopants, reducing the doping concentration in p-InGaAs. On the other hand, the nitrogen-TMA cycles in [24] has the potential to be incorporated into the DHBT process flow and reduces  $D_{\text{it}}$ . Because the edge current will be more dominant as  $W_E$  scales,



attaining low  $D_{it}$  on the InGaAs surface will be more critical to improving DC- $\beta$  in the future scaling generations of DHBTs.

### 5.3 Novel Base-Emitter Junction Designs

With the adequate surface pretreatments and ALD passivation,  $D_{it}$  could be reduced, decreasing  $I_{B,surf.rec.}$  and  $I_{B,surf.cond.}$ . However, the base current components via the bulk region,  $I_{B,diff.}$  and  $I_{B,bulk}$ , do not depend on the surface properties, and hence remain unaffected. As shown in fig. 5.4a, even in the absence of surface Fermi level pinning and surface recombination, the DC- $\beta$  eventually drops to 20 at  $W_E=75$  nm. Therefore, in addition to lowering  $D_{it}$ , modifications to the B-E junction should be made if decent DC- $\beta$  is expected in the future scaling generations of DHBTs.

In this section, three potential designs for improving DC- $\beta$  will be proposed and investigated. Before fabricating DHBTs with the new features in these designs, these new designs should be carefully evaluated. Using the TCAD model constructed and verified previously, DC- $\beta$  of devices with the designed structures or geometries was computed. The simulation results from the three designs were compared. Their correspond improvement in  $\beta$  and the challenge in integrating these designs will be discussed at the end of this section.

### 5.3.1 Epitaxy Design: Graded Base with a Pulse-doped Layer

The simulation result of DHBT58H indicates that  $\sim 24\%$  of the total base current is contributed by the current due to lateral electron diffusion via the bulk base region,  $I_{B,diff.}$ , at  $W_E=100$  nm. Because  $I_{B,diff.}$  remain approximately the same as  $W_E$  scales for a given  $W_{gap}$ , the contribution of the lateral diffusion to the base current will increase in the future scaling generations of DHBTs. Thus, it is crucial to prevent the electrons from reaching the base contact as they diffuse laterally. By an insertion of a layer of heavily doped (pulse-doped) p-InGaAs between the base and emitter semiconductors, a retarding field which blocks the electron from diffusing backward is induced by the abrupt change in the doping concentration. Fig. 5.7 compares the conduction-band profiles vs. depth into the base at the extrinsic base of a conventional graded base design against base designs of a pulse-doped layer followed by graded region. As can be seen, a  $\sim 0.5$  eV barrier is generated in both designs employing the pulse-doped layer, preventing the electron from traversing towards the base contact. Moreover, since the specific contact resistivity reduces exponentially as the doping concentration increases [26], the base contact resistance decreases when utilizing the heavily doped layer as the contact layer, improving  $f_{max}$  simultaneously.

Two base designs with different doping-graded region are proposed. Both designs employs a 5 nm InGaAs doped at  $1.2 \times 10^{20} \text{ cm}^{-3}$  as the pulse-doped layer. Beneath the pulse-doped layer, layer structure A has a 15 nm InGaAs graded from  $7$  to  $4 \times 10^{19} \text{ cm}^{-3}$ , whereas layer structure B has a 10 nm InGaAs graded from  $5$  to  $3 \times 10^{19} \text{ cm}^{-3}$ . Fig. 5.8a is the cross-section of the simulated SHBTs. The DC- $\beta$

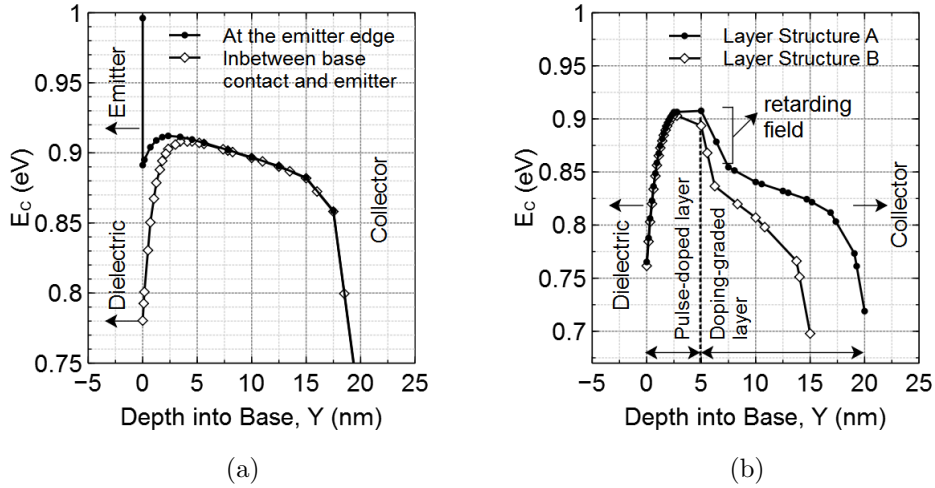


Figure 5.7: The conduction-band energy vs. the depth into the base at the extrinsic base of (a) a 20 nm base doping-graded from  $12$  to  $8 \times 10^{19} \text{ cm}^{-3}$ , and (b) designs with a 5 nm pulse-doped ( $1.2 \times 10^{20} \text{ cm}^{-3}$ ) layer followed by a doping-graded base. Layer structure A has a 15 nm InGaAs graded from  $7$  to  $4 \times 10^{19} \text{ cm}^{-3}$ . Layer structure B has a 10 nm InGaAs graded from  $5$  to  $3 \times 10^{19} \text{ cm}^{-3}$ .

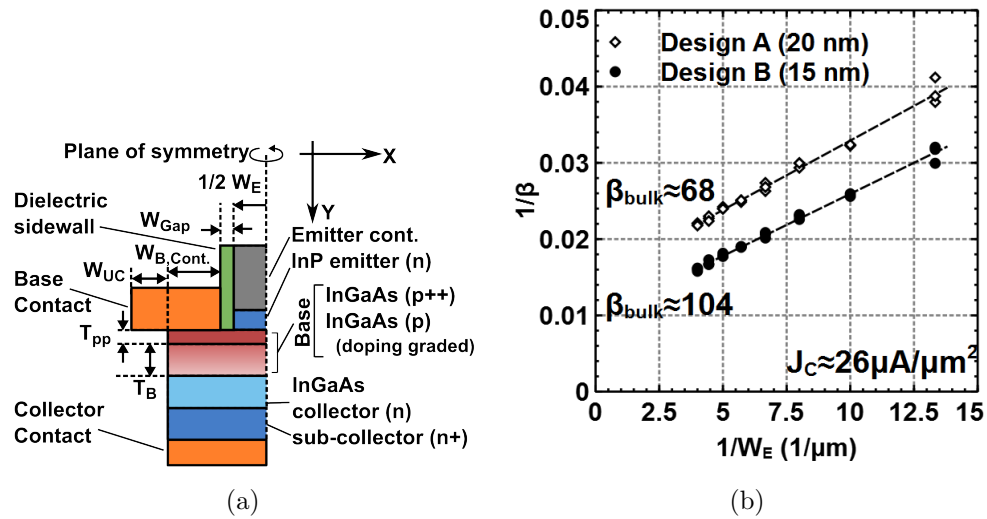


Figure 5.8: (a) The Schematic of the simulated SHBTs with a pulse-doped layer. (b) Computed  $1/\beta$  vs.  $P_{je}/A_{je}$  of the designs at  $J_E \approx 26 \text{ mA}/\mu\text{m}^2$ . The simulation retained the parameters ( $v_{\text{surf.rec.}}$ ,  $D_{\text{it}}$ ,  $C_{\text{Auger,p}}$ , etc.) of DHBT58H and assumed  $W_{\text{gap}}=10 \text{ nm}$ .

of the devices with  $W_{\text{gap}}=10\text{ nm}$  was computed at  $J_E \approx 26\text{ mA}/\mu\text{m}^2$  assuming the same parameters for DHBT58H. The simulation results are shown in fig. 5.8b. For a device with  $W_E=100\text{ nm}$  and layer structure A,  $\beta=31$  and  $K_{\text{B,edge.}}=23.6\text{ }\mu\text{A}/\mu\text{m}$ , which contributes  $\sim 28\%$  of the total base current. For the same device with layer structure B,  $\beta=39$  and  $K_{\text{B,edge.}}=21.2\text{ }\mu\text{A}/\mu\text{m}$ , indicating that approximately 32% of the total base current is due to the edge current. The edge current components due to  $I_{\text{B,surf.rec.}}$  and  $I_{\text{B,surf.cond.}}$  in both design are assumed to be similar to that in DHBT58H because they all share the same extrinsic base surface (doped at  $1.2 \times 10^{20}\text{ cm}^{-3}$ ). Therefore, the reduction in the edge current (61 to 28%) is mainly attributed to the suppression of  $I_{\text{B,diff.}}$ , indicating that the retarding field induced by the pulse-doped layer is effective. Because there are more electrons traversing towards the collector, the bulk current gain,  $\beta_{\text{bulk}}$ , has also been improved.

### 5.3.2 Supplement Process Flow: Trench in Extrinsic Base

Although the retarding field shown in fig. 5.7b has been proven effective in blocking the lateral diffusion current. The injected electrons in the pulse-doped layer (the top 5 nm) are not affected by this barrier, and may continue to diffuse laterally and eventually reach the base contact undeterred. In order to further suppress the later diffusion, the pulse-doped layer in the extrinsic base can be removed, forming a trench, and hence the retarding field is effective to all electrons in the bulk base region since they must first traverse into the graded region. The cross-section of the structure is shown in fig. 5.9a. This structure can be

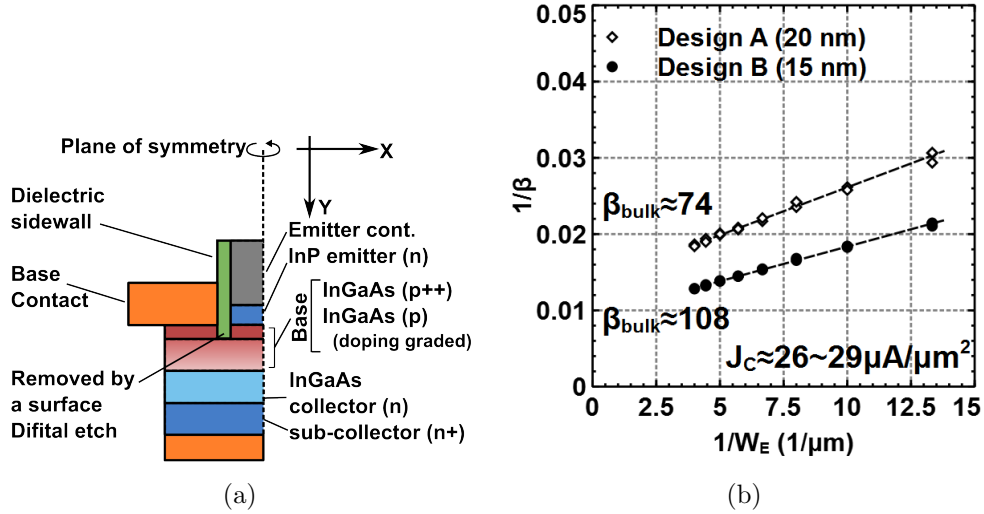


Figure 5.9: (a) The Schematic of the simulated SHBTs with the pulse-doped layer removed from the extrinsic base region. (b) Computed  $1/\beta$  vs.  $P_{je}/A_{je}$  of the designs at  $J_E \approx 26 \sim 29 \mu\text{A}/\mu\text{m}^2$ . The simulation retained the parameters ( $v_{\text{surf.rec.}}$ ,  $D_{\text{it}}$ ,  $C_{\text{Auger,p}}$ , etc.) of DHBT58H and assumed  $W_{\text{gap}}=10 \text{ nm}$ .

achieved by partially removing the pulse-doped layer using a self-limiting digital etch process [27] after the base metalization.

The layer structures A and B are again studied to evaluate this approach. The computed  $\beta$  of devices with  $W_{\text{gap}}=10 \text{ nm}$  is shown in fig. 5.9b.  $K_{\text{B,edge}}$  of layer structures A and B are  $18.2$  and  $11.8 \mu\text{A}/\mu\text{m}$ , respectively. For a device with  $W_E=100 \text{ nm}$ , this means approximately 25% of the total base current is from the edge for both layer structures, and therefore indicates that the lateral diffusion has been further suppressed. Since the structure of the base beneath the B-E junction (active base region) remains the same as that in the pulse-doped design,  $\beta_{\text{bulk}}$  only increases slightly due to the suppression of  $I_{\text{B,diff}}$ .

The cyclic process flow for digital etch usually involves semiconductor oxidation followed by wet etch. For InGaAs, the oxidation is done by UV-ozone exposure, and the oxide can be removed by diluted BHF or HCl. The simplic-

ity of the digital etch process makes it fairly compatible with the current DHBT process flow. However, with the heavily doped region removed from the extrinsic base, the disadvantage of this approach is the increased sheet resistance and  $R_{\text{gap}}$ , which reduces  $f_{\text{max}}$ . Also, a heavily doped region still remains in the active base region, which leads to higher Auger recombination rate, limiting  $\beta$ .

### 5.3.3 New Process Flow: Recessed B-E Junction and Emitter Regrowth

From the simulation results of DHBT58H and DHBT63B, approximately 30% of the base current is due to  $I_{\text{B,bulk}}$ , which is dominated by the Auger recombination. Although  $I_{\text{B,bulk}}$  scales with the emitter width, it will remain a limiting factor on DC- $\beta$  because the lifetime of the Auger recombination decreases quadratically as the doping concentration increase if the DHBT scaling laws discussed in chapter 2 is to be abided by. The need for high doping concentration results from the need to reduce the specific contact resistivity. For this purpose, only the semiconductor under the base contact has to be highly doped. Although this high doping concentration in the extrinsic base and the active base region does decrease the sheet resistance, the resistance terms associated with the sheet resistance ( $R_{\text{BE,spread}}$  and  $R_{\text{gap}}$ ) eventually become less critical to  $R_{\text{BB}}$  as  $W_{\text{E}}$  and  $W_{\text{gap}}$  scale.

In order to de-couple the doping requirements for high  $\beta$  and for high  $f_{\text{max}}$  in the base, a new geometry for a recessed B-E junction is designed. Fig. 5.10a is the cross-section of the the design. As shown in the schematic, only the region

beneath the base contact is heavily doped. With this geometry, the doping concentration in the graded region does not need to be high, and hence the Auger recombination rate decreases. To fabricate this structure, a new process flow for the B-E junction involving semiconductor regrowth must be designed. One approach is to regrow the region for base contact. Such technique has already been developed for the GaAs/AlGaAs DHBT technology [28]. It requires conformal film growth with  $> 10^{20} \text{ cm}^{-3}$  p-type doping concentration in order to minimize retain the self-aligned feature of InP DHBTs for reduction in  $R_{\text{gap}}$ , and to have low specific contact resistivity for reduction in  $R_{\text{B,cont.}}$ . However, it is challenging to achieve this in either molecular beam epitaxy (MBE) or metal organic chemical vapor deposition (MOCVD) systems [29]. Another approach involves the emitter regrowth, which requires conformal film growth and n-type doping concentration at  $> 10^{19} \text{ cm}^{-3}$ . Unlike the base regrowth, such growth has been achieved by MOCVD at a larger device dimension [30,31].

A process flow has been developed for the regrown junction. Starting from a DHBT sample with the pulse-doped layer except without the emitter structure, the B-E junction is first defined, after which the base contact is formed in the field except in the B-E junction. After encapsulating the metal contact by ALD dielectric, the B-E junction is defined again for MOCVD regrowth. The pulse-doped layer in the junction is removed by a digital etch process before the emitter semiconductor is grown onto the junction area.

Based on the layer structures A and B, the devices with the recessed B-E junction were constructed in Sentaurus. The DC- $\beta$  of the devices with  $W_{\text{gap}}=10 \text{ nm}$  was computed at  $J \approx 25 \text{ mA}/\mu\text{m}^2$ , and the simulation results are shown in fig.

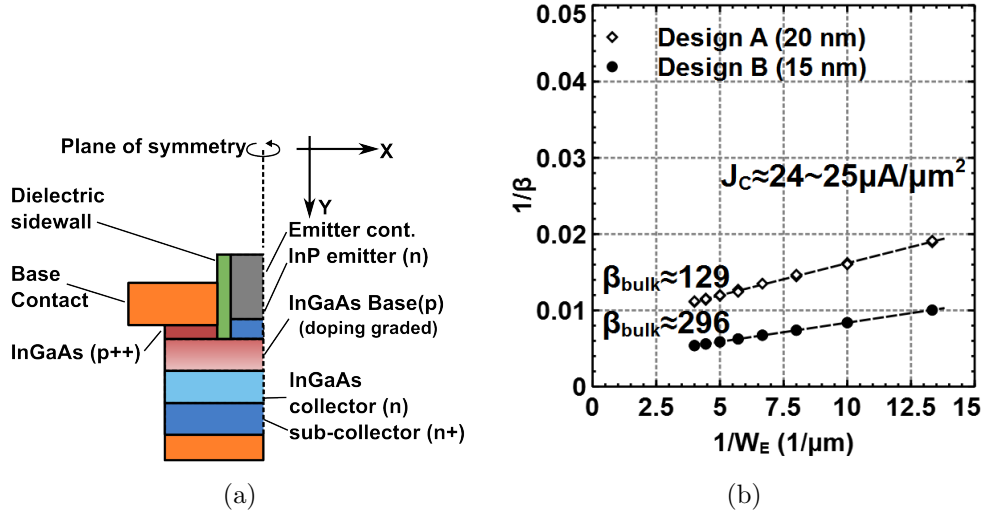


Figure 5.10: (a) The Schematic of the simulated SHBTs with the recessed B-E junction. (b) Computed  $1/\beta$  vs.  $P_{j_e}/A_{j_e}$  of the designs at  $J_E \approx 24 \sim 25 \text{ mA}/\mu\text{m}^2$ . The simulation retained the parameters ( $v_{\text{surf.rec.}}$ ,  $D_{\text{it}}$ ,  $C_{\text{Auger,p}}$ , etc.) of DHBT58H and assumed  $W_{\text{gap}}=10 \text{ nm}$ .

5.10b. Because the active base region is thin and less-heavily doped, simulations indicated a significant improve in  $\beta_{\text{bulk}}$ .  $K_{\text{B,edge}}$  for layer structure A and B are reduced to  $10.6$  and  $6.3 \mu\text{A}/\mu\text{m}$ , respectively.

Among the three designs, the pulse-doped layer and digital etch process are relatively easy to be integrated into the DHBT fabrication, and both have demonstrated suppression in  $I_{\text{B,diff}}$ . However, their improvement in  $\beta$  is still limited by Auger recombination because of high doping concentration in the active base region. The recessed B-E junction geometry, though difficult to incorporate due to its process flow involving emitter regrowth, has the potential to significantly increase DC- $\beta$ . Moreover, it is the only design which exhibit a  $\beta$  greater than 50 at  $w_E=75 \text{ nm}$ . If the regrowth process can be successfully incorporated into the DHBT fabrication with adequately low defect states, the DC-current gain in the future scaling generations of DHBTs will be substantially improved [32].



## References

- [1] V. Jain, J. C. Rode, H. W. Chiang, A. Baraskar, E. Lobisser, B. J. Thibeault, M. J. W. Rodwell, M. Urteaga, D. Loubychev, A. Snyder, Y. Wu, J. M. Fasteau, and W. Liu, "1.0 THz  $f_{\max}$  InP DHBTs in a refractory emitter and self-aligned base process for reduced base access resistance," in *69th IEEE Device Research Conference*, Jun. 2011.
- [2] M. Urteaga, R. Pierson, P. Rowell, V. Jain, E. Lobissor, and M. J. W. Rodwell, "130 nm InP DHBTs with  $f_{\tau} > 0.52$  THz and  $f_{\max} > 1.1$  THz," in *69th IEEE Device Research Conference*, Jun. 2011.
- [3] H. W. Chiang, J. C. Rode, P. Choudhary, and M. J. W. Rodwell, "Lateral Carrier Diffusion and Current Gain in THz InGaAs/InP DHBTs," *J. Appl. Phys.*, vol. 115, p. 034513, Jan. 2014.
- [4] H. W. Chiang, J. C. Rode, P. Choudhary, and M. J. W. Rodwell, "Interfacial transport and current gain in InGaAs/InP DHBTs for THz applications," in *72nd IEEE Device Research Conference*, Jun. 2014.
- [5] Y. Betser and D. Ritter, "High electron mobility in heavily doped bases of InP/GaInAs HBTs," in *7th International Conference on Indium Phosphide and Related Materials*, pp. 452–455, May 1995.
- [6] D. M. Caughey and R. E. Thomas, "Carrier mobilities in silicon empirically related to doping and field," *Proc. IEEE*, vol. 55, pp. 2192–2193, Dec. 1967.
- [7] S. Datta, K. P. Roenker, M. M. Cahaya, and W. E. Stanchina, "Implications of hole vs electron transport properties for high speed Pnp heterojunction bipolar transistors," *Solid-state Electron.*, vol. 43, pp. 73–79, Jan. 1999.
- [8] M. Dahlström, *Ultra High Speed InP Heterojunction Bipolar Transistors*. Ph.D. Thesis, Royal Institute of Technology, Stockholm, Sweden, 2003.
- [9] M. A. Haase, V. M. Robbins, N. Tabatabaie, and G. E. Stillman, "Subthreshold electron velocityfield characteristics of GaAs and  $\text{In}_{0.53}\text{Ga}_{0.47}\text{As}$ ," *J. Appl. Phys.*, vol. 57, pp. 2295–2298, Mar. 1985.

## REFERENCES

---

- [10] C. Canali, G. Majni, R. Minder, and G. Ottaviani, "Electron and hole drift velocity measurements in silicon and their empirical relation to electric field and temperature," *IEEE Trans. Electron Devices*, vol. 22, pp. 1045–1047, Nov. 1975.
- [11] H. Kroemer, "Two integral relations pertaining to the electron transport through a bipolar transistor with a nonuniform energy gap in the base region," *Solid-state Electron.*, vol. 28, pp. 1101–1103, Nov. 1985.
- [12] S. C. Jain, J. M. McGregor, and D. J. Roulston, "Band-gap narrowing in novel III-V semiconductors," *J. Appl. Phys.*, vol. 68, p. 3747, Oct. 1990.
- [13] "New Semiconductor Materials. Characteristics and Properties," <http://www.ioffe.ru/SVA/NSM/>.
- [14] V. Palankovski and Q. Rüdiger, *Analysis and Simulation of Heterostructure Devices*. Computational Microelectronics, Wien, New York, Springer, 2004.
- [15] W. Z. Cai, D. I. Lubyshev, and D. L. Miller, "Heavily carbon-doped  $\text{In}_{0.53}\text{Ga}_{0.47}\text{As}$  on InP (001) substrate grown by solid source molecular beam epitaxy," *J. Vac. Sci. Technol. B*, vol. 17, pp. 1190–1194, May 1999.
- [16] C. G. Van de Walle, "Band lineups and deformation potentials in the model-solid theory," *Phys. Rev. B*, vol. 39, pp. 1871–1883, Jan 1989.
- [17] N. K. Dutta and R. J. Nelson, "The case for Auger recombination in  $\text{In}_{1-x}\text{Ga}_x\text{As}_y\text{P}_{1-y}$ ," *J. Appl. Phys.*, vol. 53, pp. 74–92, Jan. 1982.
- [18] L. A. Coldren and S. W. Corzine, *Diode Lasers and Photonic Integrated Circuits*. Wiley Series in Microwave and Optical Engineering, 1995.
- [19] C. H. Henry, R. A. Logan, F. R. Merritt, and C. G. Bethea, "Radiative and nonradiative lifetimes in n-type and p-type  $1.6\ \mu\text{m}$  InGaAs," *Electron. Lett.*, vol. 20, pp. 358–359, Apr. 1984.
- [20] S. Hausser, G. Fuchs, A. Hangleiter, K. Streube, and W. T. Tsang, "Auger recombination in bulk and quantum well InGaAs," *Appl. Phys. Lett.*, vol. 56, pp. 913–915, Mar. 1990.
- [21] E. Zielinski, H. Schweizer, K. Streubel, H. Eisele, and G. Weimann, "Excitonic transitions and exciton damping processes in InGaAs/InP," *J. Appl. Phys.*, vol. 59, pp. 2196–2204, Mar. 1986.

## REFERENCES

---

- [22] H. Hasegawa, “Fermi Level Pinning and Schottky Barrier Height Control at Metal-Semiconductor Interfaces of InP and Related Materials,” *Jpn. J. Appl. Phys.*, vol. 38, p. 10981102, Feb. 1999.
- [23] E. Yablonoitch and T. J. Gmitter, “A contactless minority lifetime probe of heterostructures, surfaces, interfaces and bulk wafers,” *Solid-state Electron.*, vol. 35, pp. 261–267, Mar. 1992.
- [24] V. Chobpattana, J. Son, J. J. M. Law, R. Engel-Herbert, C. Y. Huang, and S. Stemmer, “Nitrogen-passivated dielectric/InGaAs interfaces with sub-nm equivalent oxide thickness and low interface trap densities,” *Appl. Phys. Lett.*, vol. 102, pp. 022907–1–022907–3, Jan. 2013.
- [25] A. D. Carter, W. J. Mitchell, B. J. Thibeault, J. J. M. Law, and M. J. W. Rodwell, “Al<sub>2</sub>O<sub>3</sub> Growth on (100) In<sub>0.53</sub>Ga<sub>0.47</sub>As Initiated by Cyclic Trimethylaluminum and Hydrogen Plasma Exposures,” *Appl. Phys. Express*, vol. 4, p. 091102, Aug. 2011.
- [26] A. Baraskar, A. C. Gossard, and M. J. W. Rodwell, “Lower limits to metal-semiconductor contact resistance: Theoretical models and experimental data,” *J. Appl. Phys.*, vol. 114, p. 154516, Oct. 2013.
- [27] S. Lee, C. Y. Huang, A. C. Carter, D. C. Elias, J. J. M. Law, V. Chobpattana, S. Krämer, B. J. Thibeault, W. Mitchell, S. Stemmer, A. C. Gossard, and R. M. J. W., “Record extrinsic transconductance (2.45 mS/m at  $V_{DS} = 0.5$  V) InAs/In<sub>0.53</sub>Ga<sub>0.47</sub>As channel MOSFETs using MOCVD source-drain regrowth,” in *2013 Symposia on VLSI Technology*, Jun. 2013.
- [28] H. Shimawaki, Y. Amamiya, N. Furuhashi, and K. Honjo, “High- $f_{max}$  AlGaAs/InGaAs and AlGaAs/GaAs HBTs with  $p^+/p$  Regrown Base Contacts,” *IEEE Trans. Electron Devices*, vol. 42, pp. 1734–1744, Oct. 1995.
- [29] Y. Dong, Y. L. Okuno, and U. K. Mishra, “Selective area growth of InP through narrow openings by MOCVD and its application to InP HBT,” in *15th International Conference on Indium Phosphide and Related Materials*, May 2003.
- [30] D. W. Scott, Y. Wei, Y. Dong, A. C. Gossard, and M. J. W. Rodwell, “A 183 GHz  $f_T$  and 165 GHz  $f_{max}$  regrown-emitter DHBT with abrupt InP emitter,” *IEEE Electron Device Lett.*, vol. 25, pp. 360–362, Jun. 2004.

## REFERENCES

---

- [31] C. Kadow, A. C. Gossard, and M. J. W. Rodwell, "Regrown-Emitter InP HBTs," in *2nd North American Conference on Molecular Beam Epitaxy*, Oct. 2004.
- [32] H. W. Chiang, J. C. Rode, P. Choudhary, and M. J. W. Rodwell, "Optimization of DC performance in terahertz InGaAs/InP double-heterojunction bipolar transistors," *J. Appl. Phys.*, submitted.

# Chapter 6

## Conclusion

## 6.1 Achievements

### 6.1.1 Process Improvements

The process flow for the composite emitter metal stack [1,2] has been modified. By adjusting the W:TiW ratio and recalibrating the refractory metal dry etch, the emitter width has been scaled below 100 nm while retaining the vertical sidewall profile necessary for the subsequent self-aligned base contact. This enables not only smaller base-emitter junction area, but also access to the extrinsic base surface after the base metalization. With the access to the extrinsic base surface, more adequate passivation technique could be applied to terminate In-GaAs, reducing the interface trap density.

A process flow for forming composite ALD  $\text{Al}_2\text{O}_3$ / PECVD  $\text{SiN}_x$  sidewall after the base metalization has been developed and integrated into the fabrication of DHBTs. Using a thermal ALD recipe,  $\text{Al}_2\text{O}_3$  can be deposited onto the extrinsic base surface without the presence of plasma; hence avoid the plasma damage. In addition, the composite sidewall encapsulates the extrinsic base, preventing damage to the extrinsic base from the subsequent process flow. Moreover, the sidewall could potentially serve as hard mask which protects the B-E junction and the extrinsic base if a base metal dry etch process is to be included after the base contact. This is beneficial to the bi-layer refractory base metal process flow [3], which is currently being developed for its integration into the DHBT process flow.

The process flow forming interconnects between metal layers in the back end process has been reinvestigated. Using the photo-sensitive resin (Photo-BCB) and thick metal lift-off ( $\sim 3\ \mu\text{m}$ ), the back end process flow has been expedited. This al-

allows the incorporation of more versatile circuit, and, more importantly, microstrip lines as well as on-wafer ML-TRL calibration standards [4] for RF measurements. This would not only enable RF measurements at various RF bandwidths, but also reduces the error/noise in the measurement and device de-embedding, allow a more accurate extrapolation of  $f_\tau$  and  $f_{\max}$ .

### 6.1.2 Device Performance

Table. 6.1 summarized the device results from two DHBT runs reported in this dissertation, DHBT63B and DHBT58H. With the modified emitter metal stack process flow, the base-emitter junction width has been successfully scaled to 85 nm on DHBT58H. As the B-E junction width reduces from 210 to 85 nm, DC- $\beta$  drops from 20 to 10. Although the devices have been scaled, the cutoff frequencies is still limited. Devices on DHBT63B exhibited low  $f_\tau$  because they were unable to sustain sufficient emitter current density. Devices on DHBT58H suffered from high  $C_{CB}$  due to overestimated B-E junction width, resulting in low  $f_{\max}$ . Both samples demonstrates high specific base contact resistivity in the devices. This further limited  $f_{\max}$ . As a result, the highest  $f_\tau f_{\max}$  product was 0.357 THz<sup>2</sup>, obtained from a device on DHBT63B with a 200 nm base-emitter junction.

Although the RF performances of DHBT63B and DHBT58H are not as good as designed, the overall transistor yields on both samples have been greatly improved. Approximately 80 to 90% of the probed device demonstrate a reasonable transistor DC characteristics. The improvement in transistor yield can be partially attributed to the adjustment in the process flow for the emitter metal stack.

Design	$T_B$	$N_A$	$T_C$	$W_E$	$\beta$	$f_\tau$	$f_{\max}$
Unit	nm	$\times 10^{19} \text{ cm}^{-3}$	nm	nm		GHz	GHz
DHBT63B	25	9-5	75	270	18.2	510	600
				220	17.4	509	702
				170	14.6	490	670
DHBT58B	20	12-8	100	210	20.2	390	780
				160	18.4	450	700
				110	16.4	405	630
				85	10.7	330	650

Table 6.1: A summary of device performance of DHBT63B and DHBT58H.

The sufficient yield enabled a more thorough mapping of devices during DC and RF measurements. Moreover, we were also able to observe the trend of DC- $\beta$ , parasitic resistance, and parasitic capacitance vs. the physical dimensions of the transistors, from which more analyses could be done.

### 6.1.3 Simulation Results

To further analyze the measured DC- $\beta$  and understand the reduction of current gain in scaled DHBTs, transport phenomenon in the base was simulated using a TCAD software (Sentaurus) [5, 6]. A model capable of estimating DC- $\beta$  to certain precision for a given DHBT design and geometry has been constructed and verified by comparison against the experimental results. Such model would be a useful tool when designing future scaling generations of DHBTs with adequate current gain.



## 6.2 Future Work

### 6.2.1 Refractory Base Contact

In order to enhance the RF performance ( $f_T$  and  $f_{max}$ ) of DHBTs, the two impending issues must be solved: high specific base contact resistivity and B-E junction failure at high current density. To reduce the specific contact resistivity on a  $\leq 20$  nm base, the penetration or reaction between the metal and InGaAs [7] must be dealt with. Otherwise, the actual metal/InGaAs interface would be deep within the base, where the doping concentration is lower, causing a higher specific contact resistivity. Currently, a bi-layer refractory base contact is under development at UCSB, and the corresponding process flow is listed in appendix A. Several DHBT samples utilizing this process flow has been fabricated. Fig. 6.1 is the TEM cross-section of a DHBT employing such process flow [3]. The improvement in the contact resistivity is now being evaluated.

### 6.2.2 Extrinsic Base Passivation

If the surface preparation technique involving nitrogen-trimethylaluminium cycle prior to ALD in the fabrication of III-V MOSFET [8] can be applied to the DHBT process flow,  $D_{it}$  on the extrinsic base surface can be decreased; hence the surface recombination and surface conduction current reduces, increasing  $\beta$  in scaled DHBTs. However, potential challenges in the implementation are expected. It is unknown if the surface pretreatments developed for the i-InGaAs of the channel of III-V MOSFETs would be applicable to p-InGaAs base of DHBTs.

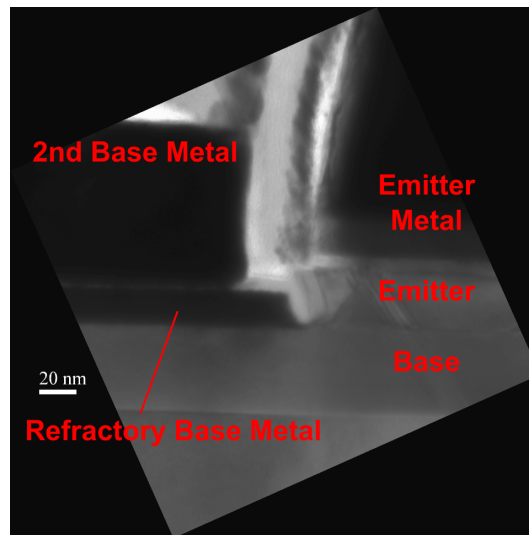


Figure 6.1: The TEM cross-section of a DHBT in bi-layer refractory base contact process flow; device courtesy of J. C. Rode.

In a worse case, thermal annealing might be necessary. The thermal stability of the base contact must be considered.

### 6.2.3 Emitter Width Scaling and Emitter Regrowth

We have demonstrated in chapter 3 a dry-etch process flow for emitter metal stack, in which the undercut to the middle of the refractory metal stack is  $\sim 10$  nm on both sides of the stack. Therefore, narrowest emitter stack this process flow could possible produce is  $\sim 50$  nm. For emitter width below 50 nm, the excessive undercut will cause the failure of the process flow. In order to successfully scale the emitter width below 50 nm, a new process flow is required. A process flow utilizing ALD metal is now being developed at UCSB. Because of the self-limiting nature of the ALD growth, a metal fin can be formed by filling

a narrow trench without void formation within the trench. However, as of this time, the process flow has not been fully integrated into the DHBT fabrication.

As discussed in chapter 5, a recessed base-emitter junction formed by an emitter regrowth process flow has the potential to improve DC- $\beta$  in scaled DHBTs. As of this time, the process development is at its preliminary stage. Several issues including the characterization of the growth, defect state located at the regrown interface, etc. are currently being investigated. In order to evaluate  $\beta$  in the actual devices efficiently, the complicated DHBT process flow should be avoided and a fast-turnaround device structure is to be designed for this purpose.

With the aforementioned possible improvements implemented, a DHBT with the simultaneously decent DC ( $\beta > 50$ ) and RF ( $f_{\max} > 1$  THz) performance will be feasible [9, 10].

## References

- [1] E. Lind, A. M. Crook, Z. Griffith, M. J. W. Rodwell, X.-M. Fang, D. Loubychev, Y. Wu, J. M. Fastenau, and W. Liu, "560 GHz  $f_{\tau}$ ,  $f_{\max}$  InGaAs/InP DHBT in a novel dry-etched emitter process," in *65th IEEE Device Research Conference*, Jun. 2007.
- [2] V. Jain, J. C. Rode, H. W. Chiang, A. Baraskar, E. Lobisser, B. J. Thibeault, M. J. W. Rodwell, M. Urteaga, D. Loubychev, A. Snyder, Y. Wu, J. M. Fastenau, and W. Liu, "1.0 THz  $f_{\max}$  InP DHBTs in a refractory emitter and self-aligned base process for reduced base access resistance," in *69th IEEE Device Research Conference*, Jun. 2011.
- [3] J. C. Rode, H. W. Chiang, P. Choudhary, W. J. Thibeault, B. J. and Mitchell, M. J. W. Rodwell, M. Urteaga, D. Loubychev, A. Snyder, Y. Wu, J. M. Fastenau, and W. K. Liu To be submitted.
- [4] R. B. Marks, "A multiline method of network analyzer calibration," *IEEE Trans. Microw. Theory Techn.*, vol. 39, no. 7, pp. 1205–1215, month = Jun., note = , abstract = , keywords = , source = , 1991.
- [5] H. W. Chiang, J. C. Rode, P. Choudhary, and M. J. W. Rodwell, "Lateral Carrier Diffusion and Current Gain in THz InGaAs/InP DHBTs," *J. Appl. Phys.*, vol. 115, p. 034513, Jan. 2014.
- [6] H. W. Chiang, J. C. Rode, P. Choudhary, and M. J. W. Rodwell, "Interfacial transport and current gain in InGaAs/InP DHBTs for THz applications," in *72nd IEEE Device Research Conference*, Jun. 2014.
- [7] E. F. Chor, W. K. Chong, and C. H. Heng, "Alternative (Pd,Ti,Au) contacts to (Pt,Ti,Au) contacts for In<sub>0.53</sub>Ga<sub>0.47</sub>As," *J. Appl. Phys.*, vol. 84, pp. 2977–2979, Sep. 1998.
- [8] V. Chobpattana, J. Son, J. J. M. Law, R. Engel-Herbert, C. Y. Huang, and S. Stemmer, "Nitrogen-passivated dielectric/InGaAs interfaces with sub-nm equivalent oxide thickness and low interface trap densities," *Appl. Phys. Lett.*, vol. 102, pp. 022907–1–022907–3, Jan. 2013.
- [9] H. W. Chiang, J. C. Rode, P. Choudhary, and M. J. W. Rodwell, "Optimization of DC performance in terahertz InGaAs/InP double-heterojunction bipolar transistors," *J. Appl. Phys.*, submitted.

## REFERENCES

---

- [10] M. J. W. Rodwell, M. Le, and B. Brar, “InP Bipolar ICs: Scaling Roadmaps, Frequency Limits, Manufacturable Technologies,” *Proc. IEEE*, vol. 92, pp. 271–286, Feb. 2008.

# Appendix A

## DHBT Process Flow

Acronym	Manufacturer	Model	Description
ALD	Oxford Instruments	FlexAL	Atomic layer deposition system
Autostepper	GCA	GCA 200	I-line (365 nm) wafer stepper
Blue Oven	Blue M Electric	N/A	High temperature oven
Dektak	Veeco Metrology LLC	Dektak 6M	Surface profilometer
E-Beam 1	Sharon Vacuum Co., Inc.	N/A	Four pocket electron beam evaporator
E-Beam 4	CHA Industries	SEC-600-RAP	Multi-wafer electron beam evaporator
EBL	JEOL	JBX-6300FS	Vector Scan Electron Beam Lithography System
Ellipsometer	J.A. Woollam Co., Inc.	M2000DI	Variable angle spectroscopic ellipsometer
ICP	Panasonic	E626I	Inductively coupled plasma etching system
Nanometrics	Nanometrics	N/A	Optical film thickness measurement
PE-II	Technic Inc.	PE-II	Parallel-plates plasma etching (ashing) system
PECVD	Plasma-Therm	790	Plasma enhanced chemical vapor deposition system
SEM	FEI	Sirion	Thermal field emission scanning electron microscopy
Sputter 4	AJA Int'l Inc.	ATC 2200-V	Seven-target DC/RF magnetron sputtering system
UV-Ozone	UVP Inc.	N/A	Uv-ozone cleaner

Table A.1: List of tools involved in DHBT fabrication.

The InP substrates with DHBT epitaxial structure were acquired from IQE corporation. Epitaxial structure is grown on a 4 inch semi-insulating InP substrate in MBE system at IQE. The physical properties of the layers (e.g. doping concentration, sheet resistance, capacitance, large area current gain, etc.) are characterized by IQE in order to monitor the growth condition and ensure the values are within the design tolerances. One-third of the 4 inch substrate is dedicated for the characterization. After receiving the SHBT substrates from IQE, the fabrication is done in the UCSB nanofabrication facility. In this appendix, the step-by-step process flow of DHBT fabrication is described. The acronyms, models and, manufacturers of tools involved in DHBT fabrication are listed in Table. A.1 according to the alphabetical order.

## A.1 Overview

The MBE substrate from IQE is first cleaved along the direction of major flat ([011]) and minor flat ([01 $\bar{1}$ ]) into piece-parts of  $3 \times 3$  cm<sup>2</sup> in order to be accommodated by the UCSB E-beam lithography system. Five pieces are obtained from each DHBT substrate. Each piece/sample is processed separately. Fig. A.1 shows the process flow of the DHBT fabrication. There are two alternatives for base contact. For lift-off base contact (LO), the contact is first defined by EBL and then metalized. For refractory bi-layer base contact (RB), the refractory metal deposition precedes the lithography of the second metal layers.

## A.2 Emitter Process Flow

### A.2.1 Emitter Contact and Composite Metal Stack

To minimize the stress of the composite metal stack, the recipe in Sputter 4 for low-stress W/TiW stack should be tested and calibrated using dummy 2-inch InP wafers beforehand.

1. E-Beam 1: deposit 20 nm of molybdenum with the chamber empty to outgas the metal source. Wait 30 minutes for the source to cool down before venting the chamber. Load a new crystal monitor into E-Beam 1 after venting.
2. Run 30 minutes UV-Ozone with the chamber empty to clean the reactor.
3. Solvent clean the sample: rinse for 3 minutes each in acetone(ACE), isopropanol(IPA), and de-ionized water (D.I.) with a trickle. Dry the sample with N<sub>2</sub> gun.
4. 10 minutes dehydration bake at 110°C.
5. 15 minutes UV-Ozone treatment for the sample.
6. Etch the sample for 1 minute in 1:10 HCl : H<sub>2</sub>O. 1 minute D.I. rinse with a trickle. Dry the sample with N<sub>2</sub> gun.
7. Immediately load the sample into E-Beam 1. Deposit 20 nm of Mo at chamber pressure  $< 10^{-7}$  Torr and deposition rate  $< 0.5\text{\AA}/\text{s}$ . Wait 30 minutes for the source to cool down before venting the chamber.
8. Sputter 4: 20 minutes W and 20 minutes Ti<sub>0.1</sub>W<sub>0.9</sub> deposition with the chamber empty to outgas the sputtering targets and coat the carrier chuck.



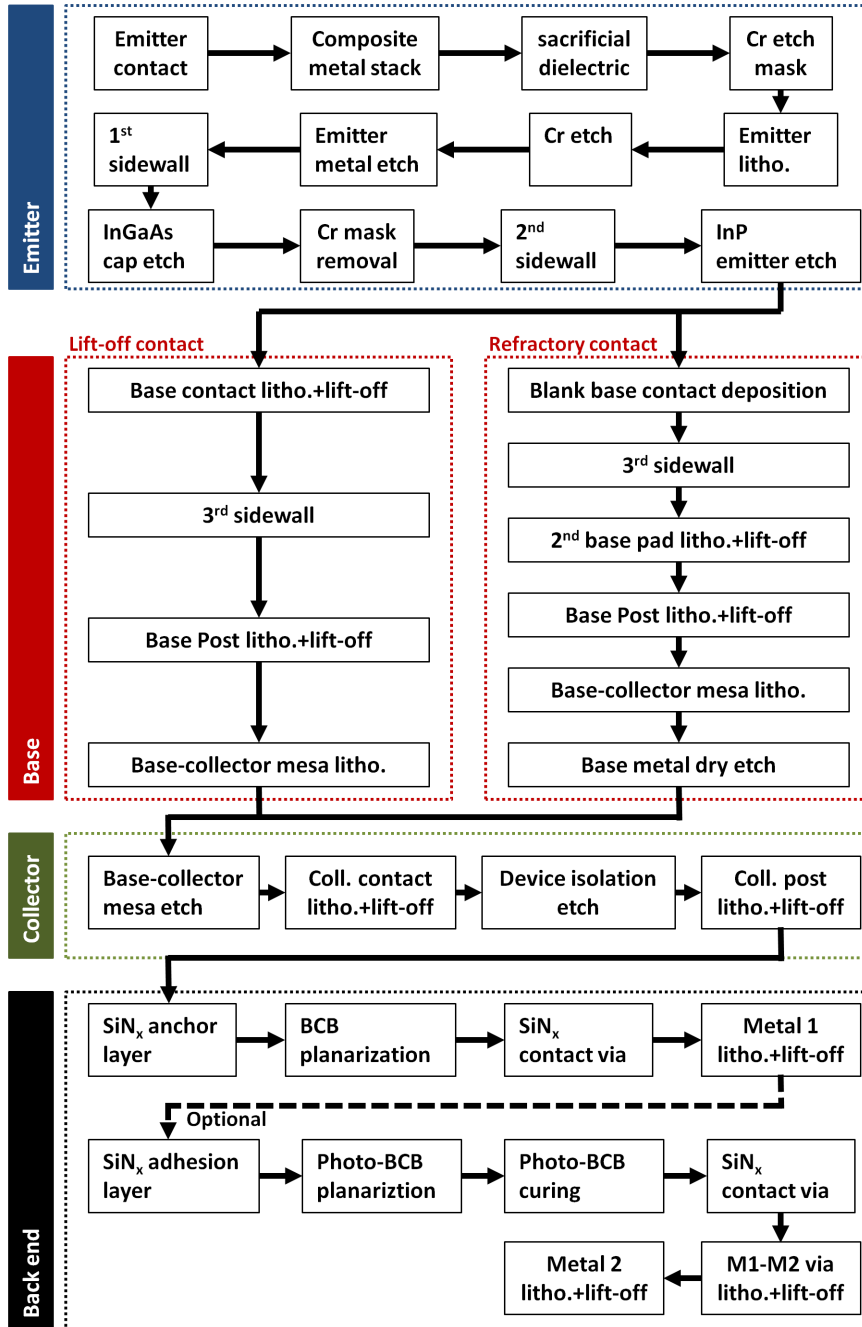


Figure A.1: Flow chart of mesa DHBT fabrication.

9. After venting E-Beam 1, immediately transfer the sample into Sputter 4 to avoid further oxidation of Mo.
10. Sputter 4: deposit 150 nm of W and 350 nm of  $\text{Ti}_{0.1}\text{W}_{0.9}$  on the sample.

### **A.2.2 Sacrificial Dielectric Layer and Chromium Mask Deposition**

1. PECVD: make sure the center chuck is at 250°C.
2. Carefully wipe the PECVD chamber wall with clean room wipe saturated with IPA. Refrain from touching the center chuck for your own safety and the cleanliness of the chamber.
3. PECVD: run the standard 30 minute  $\text{CF}_4/\text{O}_2$  etch + 200 Å  $\text{SiO}_2$  deposition to clean the chamber.
4. Deposit 80 nm of  $\text{SiO}_2$  on the sample using the standard recipe.
5. Deposit 40 nm of  $\text{SiN}_x$  on the sample using the standard recipe.
6. E-Beam 1: deposit 40 nm of Cr on the sample.

### **A.2.3 Emitter Lithography**

1. Solvent clean the sample. 10 minutes dehydration bake at 110°C.
2. PE-II:  $\text{O}_2$  de-scum at 100 W and 300 mTorr for 30 seconds to clean the sample.
3. Apply ma-N 2403 resist on the sample using syringe and 0.2  $\mu\text{m}$  filters. Spin-coat at 4000 rpm for 30 seconds. Bake at 90°C for 90 seconds.
4. EBL: load the sample into the cassette with the major flat direction parallel to the horizontal (x) direction of EBL.
5. EBL: expose the sample with the emitter pattern/job.
6. Develop in AZ300MIF for 35 seconds with slight agitation every 10 seconds. 3 minutes D.I. rinse with a trickle. Dry the sample with  $\text{N}_2$  gun.
7. verify the pattern using an optical microscope.

Note: 2:1 ma-N2405:Thinner is very comparable to maN2403 in terms of thickness and dose.

### A.2.4 Chromium Mask Dry Etch

1. ICP: Make sure the etch chamber temperature is 50°C. Run 10 minutes standard O<sub>2</sub> clean.
2. Etch chemistry and gas flow: Cl<sub>2</sub>/O<sub>2</sub> = 26/4 sccm; chamber pressure: 1 Pa; ICP/forward bias power 400/18 W.
3. Conditioning (chamber empty) run 125 seconds. Etch the sample for 125 seconds.
4. 3 minutes ACE rinse and 3 minutes IPA rinse.
5. Strip ma-N 2403 in 1165 at 80°C for 1 hour. 3 minutes IPA rinse followed by 3 minutes D.I. rinse with a trickle. Dry the sample with N<sub>2</sub> gun.

### A.2.5 Emitter Composite Stack Dry Etch

1. Solvent clean the sample.
2. ICP: Make sure the etch chamber temperature is 50 °C. Run 10 minutes standard O<sub>2</sub> clean.
3. (High power etch) Etch chemistry and gas flow: SF<sub>6</sub>/Ar = 20/5 sccm, chamber pressure: 1 Pa; ICP/forward bias power 600/200 W; etch time: 195 seconds.
4. (Medium power etch) Etch chemistry and gas flow: SF<sub>6</sub>/Ar = 6.7/3.3 sccm, chamber pressure: 1 Pa; ICP/forward bias power 600/50 W.
5. (Low power etch) Etch chemistry and gas flow: SF<sub>6</sub>/Ar = 6.7/3.3 sccm, chamber pressure: 0.5 Pa; ICP/forward bias power 600/18 W; etch time: 70 seconds.
6. Run high power etch with the chamber empty for conditioning.
7. Etch the sample with consecutive high power etch (195 seconds) and low power etch (70 seconds). If the sample appearance is still metallic, run 30 seconds medium power etch.
8. Solvent clean the sample.
9. SEM: check the dry etch profile with SEM. If the bottom (W) flares out, etch the sample with low power etch for another 15 seconds and then solvent clean. Repeat this step until the etch profile is vertical.

10. Measure the stack thickness with Dektak.

### A.2.6 First SiN<sub>x</sub> Sidewall Formation

1. Solvent clean the sample.
2. PECVD: make sure the center chuck is at 250°C.
3. Carefully wipe the PECVD chamber wall with clean room wipe saturated with IPA. Refrain from touching the center chuck for your own safety and the cleanliness of the chamber.
4. PECVD: run the standard 30 minute CF<sub>4</sub>/O<sub>2</sub> etch + 200 Å SiN<sub>x</sub> deposition to clean the chamber.
5. Etch the sample for 10 seconds in 1:10 HCl : H<sub>2</sub>O. 1 minute D.I. rinse with a trickle.
6. Immediately transfer the sample into PECVD and deposit 20 nm of SiN<sub>x</sub>.
7. Deposit 100 nm of SiN<sub>x</sub> on a 2 inch Si wafer. Cleave the Si wafer so it and the sample are approximately of the same size.
8. Measure SiN<sub>x</sub> thickness with Ellipsometer.
9. ICP: Make sure the etch chamber temperature is 50 °C. Run 10 minutes standard O<sub>2</sub> clean.
10. (High power etch) Etch chemistry and gas flow: CF<sub>4</sub>/O<sub>2</sub> = 20/5 sccm; chamber pressure: 1 Pa; ICP/forward bias power 500/100 W.
11. (Low power etch) Etch chemistry and gas flow: CF<sub>4</sub>/O<sub>2</sub> = 20/2 sccm; chamber pressure: 0.3 Pa; ICP/forward bias power 25/18 W.
12. Run high power etch for 5 minutes with the chamber empty for conditioning.
13. Etch the Si piece with low power etch for 4 minutes.
14. Measure SiN<sub>x</sub> thickness again with Ellipsometer and determine the etch rate. Calculate the etch time for 20% overetch (120%) accordingly.
15. Etch the sample with low power etch for the calculated time.
16. Solvent clean the sample.
17. SEM: check the sample for any abnormality.

### A.2.7 InGaAs Emitter Cap Wet Etch

1. Solvent clean the sample.
2. Mix 1:10  $\text{NH}_4\text{OH} : \text{H}_2\text{O}$  solution and stir it with the wafer basket. Mix 1:1:25  $\text{H}_3\text{PO}_4 : \text{H}_2\text{O}_2 : \text{H}_2\text{O}$  solution. Stir at 200 rpm for at least 5 minutes.
3. Etch the sample in  $\text{NH}_4\text{OH} : \text{H}_2\text{O}$  solution for 10 sec. D.I. rinse for 30 seconds with a trickle and dry the sample with  $\text{N}_2$  gun.
4. Etch the sample in  $\text{H}_3\text{PO}_4 : \text{H}_2\text{O}_2 : \text{H}_2\text{O}$  solution for 5 to 7 seconds without stirrer. D.I. rinse for 3 minute with a trickle and dry the sample with  $\text{N}_2$  gun.

### A.2.8 Chromium Mask Removal

1. Solvent clean the sample.
2. (Optional) Dehydration bake for 10 minutes at  $110^\circ\text{C}$ .
3. (Optional) Apply SPR955CM-1.8 photoresist on the sample and spin-coat at 4000 rpm for 30 seconds. Bake at  $90^\circ\text{C}$  for 1 minute.
4. (Optional) Measure the photoresist thickness with Nanometrics using "Positive Resist on Si" recipe and refractive index of 1.6. Thickness should be 1.6 to  $1.7 \mu\text{m}$ .
5. (Optional) PE-II: clean the chamber wall. Run 5 minutes  $\text{O}_2$  de-scum at 300 W and 300 mTorr with chamber empty.
6. (Optional) PE-II: 8 minutes  $\text{O}_2$  de-scum at 200 W and 300 mTorr on the sample.
7. (Optional) Measure the photoresist thickness again. Calculate the etch rate.
8. (Optional) Etch the sample with PE-II until photoresist surface is 50 to 100 nm lower than the TiW/ $\text{SiO}_2$  interface.
9. (Optional) Bake at  $110^\circ\text{C}$  for 1 minute.
10. Mix Tergitol<sup>TM</sup>:buffered-HF (BHF) solution (approximately 1:200). Carefully stir the solution with the wafer basket until foam appears.

11. Etch the sample in the Tergitol<sup>TM</sup>:BHF solution for 65 seconds with slight agitation every 10 seconds. D.I. rinse with a trickle for 3 to 5 minute until the foam disappear. Dry the sample with N<sub>2</sub> gun.
12. (If followed the optional steps) Strip the photoresist in 1165 at 80°C for 1 hour. 3 minutes IPA rinse followed by 3 minutes D.I. rinse with a trickle. Dry the sample with N<sub>2</sub> gun.
13. SEM: observe the sample and determine the removal yield.

### **A.2.9 Second SiN<sub>x</sub> Sidewall Formation**

Repeat the steps for the first SiN<sub>x</sub> sidewall.

### **A.2.10 InP Emitter Wet Etch (LO)**

1. Solvent clean the sample.
2. Mix 1:10 NH<sub>4</sub>OH : H<sub>2</sub>O solution and stir it with the wafer basket. Mix 4:1 H<sub>3</sub>PO<sub>4</sub> : HCl solution. Stir at 200 rpm for at least 5 minutes.
3. Etch the sample in NH<sub>4</sub>OH : H<sub>2</sub>O solution for 10 sec. D.I. rinse for 30 seconds with a trickle and dry the sample with N<sub>2</sub> gun.
4. Etch the sample in H<sub>3</sub>PO<sub>4</sub> : HCl solution for 8 to 10 seconds (depends on emitter thickness) without stirrer. D.I. rinse for 3 minute with a trickle and dry the sample with N<sub>2</sub> gun.

### **A.2.11 Base Contact Lithography and Lift-off(LO)**

The base contact metalization steps must immediately follow the InP emitter etch to minimize specific contact resistivity.

1. Solvent clean the sample. Dehydration bake for 10 minutes at 110°C.
2. Apply UV-6 resist on the sample and spin-coat at 3000 rpm and 400 rpm/s for 60 seconds. Bake at 115°C for 1 minute.
3. EBL: load the sample into the cassette with the major flat direction parallel to the horizontal (x) direction of EBL.
4. EBL: align and expose the sample with the base contact pattern/job.

5. Bake at 115°C for 2 minutes immediately after EBL.
6. Develop in AZ300MIF for 70 to 75 seconds with slight agitation every 15 seconds. 3 minutes D.I. rinse with a trickle. Dry the sample with N<sub>2</sub> gun.
7. E-Beam 4: load private Pd, Ti, Au, Pt sources, and a new crystal monitor.
8. Etch the sample in 1:10 HCl : H<sub>2</sub>O solution for 10 sec. D.I. rinse for 1 minute with a trickle and dry the sample with N<sub>2</sub> gun.
9. After the chamber pressure < 10<sup>-6</sup> Torr, evaporate 25 Å of Pt at deposition rate < 0.2 Å/s, 170 Å of Ti at deposition rate < 0.5 Å/s, 170 Å of Pd at deposition rate < 0.5 Å/s, and 650 Å of Au at deposition rate < 1 Å/s on the sample.
10. Strip UV-6 and lift-off in 1165 at 80°C for 1 hour. 3 minutes IPA rinse followed by 3 minutes D.I. rinse with a trickle. Dry the sample with N<sub>2</sub> gun.
11. SEM: observe the sample and check for any abnormality.

### **A.2.12 Third Sidewall Formation (LO/RB)**

The third sidewall formation steps should immediately follow the base metalization to prevent further contamination on InGaAs surface of the extrinsic base.

1. ALD: set the chamber temperature to 200°C. Run 100 cycles of thermal Al<sub>2</sub>O<sub>3</sub> deposition with the chamber empty.
2. ALD: deposit 150 cycles of thermal Al<sub>2</sub>O<sub>3</sub> on a 2 inch Si wafer. Measure thickness with Ellipsometer and determine the deposition rate.
3. Solvent clean the sample.
4. (Optional) Run 30 minutes UV-Ozone with the chamber empty to clean the reactor. 10 to 15 minutes UV-Ozone treatment for the sample.
5. Etch the sample for 1 minute in 1:10 HCl : H<sub>2</sub>O. 1 minute D.I. rinse with a trickle. Dry the sample with N<sub>2</sub> gun. Immediately transfer the sample into ALD loadlock.
6. Based on the obtained rate, deposit 10 nm of Al<sub>2</sub>O<sub>3</sub> on the sample.
7. Follow the steps of first/second SiN<sub>x</sub> sidewall formation to form 20 to 30 nm thick sidewall.

8. Use the SiN<sub>x</sub> sidewall as hard mask and etch Al<sub>2</sub>O<sub>3</sub> in AZ300MIF for 120% overetch (etch rate  $\approx 20\text{\AA}/\text{s}$ ). 3 minute D.I. rinse with a trickle. Dry the sample with N<sub>2</sub> gun.
9. SEM: observe the sample and check for any abnormality.

Note: AZ300MIF could be substituted by diluted BHF for etching Al<sub>2</sub>O<sub>3</sub>.

### **A.2.13 Base Post Lithography and Lift-off (LO/RB)**

1. Measure the base contact pad thickness with Dektak.
2. Solvent clean the sample. Dehydration bake for 10 minutes at 110°C.
3. Apply LOL resin on the sample and spin-coat at 3000 rpm for 30 seconds. Bake at 180°C for 2 minutes.
4. Apply nLOF5510 photoresist on the sample and spin-coat at 1800 rpm and 350 rpm/s for 40 seconds. Bake at 90°C for 60 seconds.
5. Load the sample into Autostepper in the orientation 180° rotated from that of the EBL.
6. Align and expose the sample for 0.2 to 0.24 second with the base post mask.
7. Bake at 110°C for 60 seconds.
8. Develop the sample in AZ300MIF for 105 seconds without any agitation. 3 minute D.I. rinse with a trickle. Dry the sample with N<sub>2</sub> gun.
9. Verify the pattern and the alignment using an optical microscope with the green filter. Look for the undercut to LOL. Rework if no undercut is observed or the misalignment is too great.
10. PE-II: O<sub>2</sub> de-scum at 100 W and 300 mTorr for 20 seconds.
11. E-Beam 4: replace crystal monitor. Evaporate 200 Å of Ti at deposition rate  $< 0.5\text{\AA}/\text{s}$  and  $x\text{\AA}$  of Au at deposition rate  $= 1 \sim 4\text{\AA}/\text{s}$  on the sample, where  $x$  equals the thickness required for the base post to be at least 50 nm taller than the emitter stack (W/TiW plus base metal on top of it).
12. Strip the photoresist and lift-off in 1165 at 80°C for 1 hour. 3 minutes IPA rinse followed by 3 minutes D.I. rinse with a trickle. Dry the sample with N<sub>2</sub> gun.



13. SEM: observe the sample and check for any abnormality.

Note: LOL resin could be substituted by 1:2 PMGI:T Thinner.

#### **A.2.14 Base-collector Mesa Lithography (LO/RB)**

1. Solvent clean the sample. Dehydration bake for 10 minutes at 110°C.
2. Apply HMDS on the sample and wait 20 seconds. Spin-coat at 3000 rpm for 60 seconds and wait for another 60 seconds.
3. Apply ma-N 2410 resist on the sample using syringe and 0.2  $\mu\text{m}$  filters. Spin-coat at 3000 rpm and 450 rpm/s for 60 seconds. Bake at 90°C for 150 seconds.
4. EBL: load the sample into the cassette with the major flat direction parallel to the horizontal (x) direction of EBL.
5. EBL: align and expose the sample with the base mesa pattern/job.
6. Develop in AZ300MIF for 135 seconds with slight agitation every 10 seconds. 3 minutes D.I. rinse with a trickle. Dry the sample with N<sub>2</sub> gun.
7. PE-II: O<sub>2</sub> de-scum the sample at 100 W and 300 mTorr for 30 seconds.
8. SEM: verify the pattern and the alignment using a dummy DHBT structure.

#### **A.2.15 InP Emitter Wet Etch (RB)**

1. Run 15 minutes UV-Ozone with the chamber empty to clean the reactor.
2. Mix 1:10 HCl : H<sub>2</sub>O solution and stir it with the wafer basket. Mix 4:1 H<sub>3</sub>PO<sub>4</sub> : HCl solution. Stir at 200 rpm for at least 5 minutes.
3. Solvent clean the sample.
4. 10 minutes UV-Ozone treatment for the sample.
5. Etch the sample for 10 seconds in 1:10 HCl : H<sub>2</sub>O. 1 minute D.I. rinse with a trickle. Dry the sample with N<sub>2</sub> gun.
6. Etch the sample in H<sub>3</sub>PO<sub>4</sub> : HCl solution for 5 to 7 seconds (depends on emitter thickness) without stirrer. D.I. rinse for 3 minute with a trickle and dry the sample with N<sub>2</sub> gun.

7. Solvent clean the sample.
8. Etch the sample for 10 seconds in 1:10 HCl : H<sub>2</sub>O. 1 minute D.I. rinse with a trickle. Dry the sample with N<sub>2</sub> gun.

### **A.2.16 First Base Metalization (RB)**

The base contact metalization steps must immediately follow the InP emitter etch to minimize specific contact resistivity.

1. Before InP emitter etch, deposit 20 nm of Pt and 20 nm of ruthenium with E-Beam 1 with the chamber empty to outgas the metal source. Wait 30 minutes for the source to cool down before venting the chamber. Load a new crystal monitor into E-Beam 1 after venting.
2. After InP emitter etch, immediately load the sample into E-Beam 1. After chamber pressure  $< 10^{-7}$  Torr, deposit 20 Å of Pt at deposition rate  $< 0.2\text{Å/s}$ , 200 Å of Ru at deposition rate  $< 0.5\text{Å/s}$ , and 20 Å of Pt at deposition rate  $< 0.5\text{Å/s}$ . Wait 30 minutes for the source to cool down before venting the chamber.

### **A.2.17 Second Base Metal Lithography and Lift-off (RB)**

1. Solvent clean the sample. Dehydration bake for 10 minutes at 110°C.
2. Apply PMGI SF-8 resin on the sample using syringe and 0.2 μm filters. Spin-coat at 4000 rpm and 400 rpm/s for 60 seconds. Bake at 180°C for 3 minutes.
3. Apply 1:1 ZEP520:A resist on the sample using syringe and 0.2 μm filters. Spin-coat at 3000 rpm for 60 seconds. Bake at 180°C for 3 minutes.
4. EBL: load the sample into the cassette with the major flat direction parallel to the horizontal (x) direction of EBL.
5. EBL: align and expose the sample with the base contact pattern/job.
6. ZEP development: 50 seconds amyl acetate and 60 seconds IPA. Dry the sample with N<sub>2</sub> gun.
7. PMGI development: 250 seconds AZ300MIF. D.I. rinse for 3 minute with a trickle and dry the sample with N<sub>2</sub> gun.

8. E-Beam 4: load private Ti, Au sources, and a new crystal monitor.
9. After the chamber pressure  $< 10^{-6}$  Torr, evaporate 200 Å of Ti at deposition rate  $< 0.5\text{Å/s}$ , and 650 Å of Au at deposition rate  $< 1\text{Å/s}$  on the sample.
10. Strip the resist and lift-off in 1165 at 80°C for 1 hour. 3 minutes IPA rinse followed by 3 minutes D.I. rinse with a trickle. Dry the sample with N<sub>2</sub> gun.
11. SEM: observe the sample and check for any abnormality.

### **A.2.18 Refractory Metal Dry Etch (RB)**

1. ICP: Make sure the etch chamber temperature is 50 °C. Run 10 minutes standard O<sub>2</sub> clean.
2. Etch chemistry and gas flow: Cl<sub>2</sub>/O<sub>2</sub> = 5/20 sccm; chamber pressure: 0.67 Pa; ICP/forward bias power 400/100 W.
3. 50 seconds chamber conditioning using the above recipe. Etch the sample for 50 seconds (etch time scales with Ru thickness).
4. Carefully clean the back side of the sample with cleanroom solvent (ACE, IPA, D.I.) and swab. Dry the sample with N<sub>2</sub> gun.
5. Leave the resist on the sample for the subsequent base-collector mesa wet etch.

### **A.2.19 Base-collector Mesa Wet Etch**

InGaAs wet etch for base, setback and InGaAs/InAlAs superlattice grade:

1. Measure the base mesa resist thickness with Dektak.
2. Mix 1:10 NH<sub>4</sub>OH : H<sub>2</sub>O solution and stir it with the wafer basket. Mix 1:1:25 H<sub>3</sub>PO<sub>4</sub> : H<sub>2</sub>O<sub>2</sub> : H<sub>2</sub>O solution. Stir at 200 rpm for at least 5 minutes.
3. Etch the sample in NH<sub>4</sub>OH : H<sub>2</sub>O solution for 10 sec. D.I. rinse for 30 seconds with a trickle and dry the sample with N<sub>2</sub> gun.
4. Etch the sample in H<sub>3</sub>PO<sub>4</sub> : H<sub>2</sub>O<sub>2</sub> : H<sub>2</sub>O solution for 25 to 30 seconds (depends on base/collector designs) without stirrer. D.I. rinse for 3 minute with a trickle and dry the sample with N<sub>2</sub> gun.

5. Measure thickness with Dektak again and make sure that target depth is reached. Otherwise, do additional InGaAs etch before proceeding.

InP wet etch for collector:

6. Mix 4:1  $\text{H}_3\text{PO}_4$  : HCl solution. Stir at 200 rpm for at least 5 minutes.
7. Etch the sample in  $\text{H}_3\text{PO}_4$  : HCl solution for 22 to 32 seconds (time varies with collector designs) without stirrer. D.I. rinse for 3 minute with a trickle and dry the sample with  $\text{N}_2$  gun.
8. Measure thickness with Dektak again and make sure that target depth is reached. Otherwise, do additional InP etch.
9. Strip the resist in 1165 at  $80^\circ\text{C}$  for 1 hour. 3 minutes IPA rinse followed by 3 minutes D.I. rinse with a trickle. Dry the sample with  $\text{N}_2$  gun.
10. SEM: observe the sample and verify the etch.

Note: both InGaAs and InP wet etch time depend on the epitaxial design. The etch time for 25 nm base, 14.5 nm setback, and 12 nm InGaAs/InAlAs grade is 27 seconds. The etch time for 77.5 nm InP collector is 28 seconds.

### **A.2.20 Collector Contact Lithography and Lift-off**

1. Solvent clean the sample. Dehydration bake for 10 minutes at  $110^\circ\text{C}$ .
2. Apply nLOF2020 photoresist on the sample and spin-coat at 3500 rpm for 30 seconds. Bake at  $110^\circ\text{C}$  for 60 seconds.
3. Load the sample into Autostepper in the orientation  $180^\circ$  rotated from that of the EBL.
4. Align and expose the sample for 0.16 second with the collector contact mask.
5. Bake at  $115^\circ\text{C}$  for 60 seconds.
6. Develop the sample in AZ300MIF for 120 seconds with minor agitation every 30 seconds. 3 minute D.I. rinse with a trickle. Dry the sample with  $\text{N}_2$  gun.
7. Verify the pattern and the alignment using an optical microscope with the green filter. Rework if the misalignment is too great.
8. PE-II:  $\text{O}_2$  de-scum at 100 W and 300 mTorr for 20 seconds.

9. Etch the sample for 10 seconds in 1:10 HCl : H<sub>2</sub>O. 1 minute D.I. rinse with a trickle. Dry the sample with N<sub>2</sub> gun. Immediately load the sample into E-Beam 4 afterwards.
10. E-Beam 4: replace crystal monitor. Evaporate 200 Å of Ti at deposition rate < 0.5Å/s, 200 Å of Pd at deposition rate < 0.5Å/s, and 2500 Å of Au at deposition rate = 1 ~ 4Å/s onto the sample.
11. Strip the photoresist and lift-off in 1165 at 80°C for 1 hour. 3 minutes IPA rinse followed by 3 minutes D.I. rinse with a trickle. Dry the sample with N<sub>2</sub> gun.
12. SEM: observe the sample and check for any abnormality.

### A.2.21 Device Isolation Lithography and Wet Etch

Lithography:

1. Solvent clean the sample. Dehydration bake for 10 minutes at 110°C.
2. Apply SPR955CM-0.9 photoresist on the sample and spin-coat at 3000 rpm for 30 seconds. Bake at 95°C for 90 seconds.
3. Load the sample into Autostepper in the orientation 180° rotated from that of the EBL.
4. Align and expose the sample for 0.27 second with the device isolation mask.
5. Bake at 110°C for 90 seconds.
6. Develop the sample in AZ300MIF for 60 seconds with slight agitation every 15 seconds. 3 minute D.I. rinse with a trickle. Dry the sample with N<sub>2</sub> gun.
7. Verify the pattern and the alignment using an optical microscope with the green filter. Rework if the misalignment is too great.
8. PE-II: O<sub>2</sub> de-scum at 100 W and 300 mTorr for 20 seconds.

InGaAs sub-collector wet etch:

9. Measure the photoresist thickness with Dektak.
10. Mix 1:10 NH<sub>4</sub>OH : H<sub>2</sub>O solution and stir it with the wafer basket. Mix 1:1:25 H<sub>3</sub>PO<sub>4</sub> : H<sub>2</sub>O<sub>2</sub> : H<sub>2</sub>O solution. Stir at 200 rpm for at least 5 minutes. Mix 4:1 H<sub>3</sub>PO<sub>4</sub> : HCl solution. Stir at 200 rpm for at least 5 minutes.

11. Etch the sample in  $\text{NH}_4\text{OH} : \text{H}_2\text{O}$  solution for 10 sec. D.I. rinse for 30 seconds with a trickle and dry the sample with  $\text{N}_2$  gun.
12. InGaAs etch-stop etch: etch the sample in  $\text{H}_3\text{PO}_4 : \text{H}_2\text{O}_2 : \text{H}_2\text{O}$  solution for 15 seconds without stirrer. D.I. rinse for 3 minute with a trickle and dry the sample with  $\text{N}_2$  gun.
13. InP sub-collector etch: etch the sample in  $\text{H}_3\text{PO}_4 : \text{HCl}$  solution for 30 seconds without stirrer. D.I. rinse for 3 minute with a trickle and dry the sample with  $\text{N}_2$  gun.
14. Measure thickness with Dektak again and make sure that target depth is reached. Otherwise, do additional InP etch before proceeding.

Semi-insulating InP wet etch:

15. InGaAs etch-stop etch: etch the sample in  $\text{H}_3\text{PO}_4 : \text{H}_2\text{O}_2 : \text{H}_2\text{O}$  solution for 10 seconds without stirrer. D.I. rinse for 3 minute with a trickle and dry the sample with  $\text{N}_2$  gun.
16. Semi-insulating InP etch: etch the sample in  $\text{H}_3\text{PO}_4 : \text{HCl}$  solution for 12 to 15 seconds without stirrer. D.I. rinse for 3 minute with a trickle and dry the sample with  $\text{N}_2$  gun.
17. Measure thickness with Dektak again. Approximately 100 to 200 nm of semi-insulating InP should be removed.
18. Strip the photoresist in 1165 at  $80^\circ\text{C}$  for 1 hour. 3 minutes IPA rinse followed by 3 minutes D.I. rinse with a trickle. Dry the sample with  $\text{N}_2$  gun.
19. SEM: observe the sample and check for any abnormality.

### **A.2.22 Collector Post Lithography and Lift-off**

1. Measure the base contact pad thickness with Dektak.
2. Solvent clean the sample. Dehydration bake for 10 minutes at  $110^\circ\text{C}$ .
3. Apply nLOF2020 photoresist on the sample and spin-coat at 3500 rpm for 30 seconds. Bake at  $110^\circ\text{C}$  for 60 seconds.
4. Load the sample into Autostepper in the orientation  $180^\circ$  rotated from that of the EBL.

5. Align and expose the sample for 0.16 second with the collector post mask.
6. Bake at 115°C for 60 seconds.
7. Develop the sample in AZ300MIF for 120 seconds with minor agitation every 30 seconds. 3 minute D.I. rinse with a trickle. Dry the sample with N<sub>2</sub> gun.
8. Verify the pattern and the alignment using an optical microscope with the green filter. Rework if the misalignment is too great.
9. PE-II: O<sub>2</sub> de-scum at 100 W and 300 mTorr for 20 seconds.
10. Etch the sample for 10 seconds in 1:10 HCl : H<sub>2</sub>O. 1 minute D.I. rinse with a trickle. Dry the sample with N<sub>2</sub> gun. Immediately load the sample into E-Beam 4 afterwards.
11. E-Beam 4: replace crystal monitor. Evaporate 200 Å of Ti at deposition rate < 0.5 Å/s and x Å of Au at deposition rate = 1 ~ 4 Å/s onto the sample, where x equals the thickness required for the collector post to be at least 100 nm taller than the emitter stack (W/Tiw plus base metal on top of it).
12. Strip the photoresist and lift-off in 1165 at 80°C for 1 hour. 3 minutes IPA rinse followed by 3 minutes D.I. rinse with a trickle. Dry the sample with N<sub>2</sub> gun.
13. SEM: observe the sample and check for any abnormality. Measure the gap spacing of the TLM structures.

### **A.2.23 SiN<sub>x</sub> Anchor Layer Deposition**

1. PECVD: make sure the center chuck is at 250°C.
2. Carefully wipe the PECVD chamber wall with clean room wipe saturated with IPA. Refrain from touching the center chuck for your own safety and the cleanliness of the chamber.
3. PECVD: run the standard 30 minute CF<sub>4</sub>/O<sub>2</sub> etch + 200 Å SiN<sub>x</sub> deposition to clean the chamber.
4. Run 30 minutes UV-Ozone with the chamber empty to clean the reactor.
5. Solvent clean the sample.
6. 10 minutes UV-Ozone treatment for the sample.

7. Etch the sample for 10 seconds in 1:10 HCl : H<sub>2</sub>O. 1 minute D.I. rinse with a trickle. Dry the sample with N<sub>2</sub> gun.
8. Immediately transfer the sample into PECVD and deposit 40 nm of SiN<sub>x</sub>.

### A.2.24 BCB Planarization

BCB curing:

1. Turn on the Blue Oven and set the N<sub>2</sub> flow to 100 units.
2. Solvent clean the sample. Dehydration bake for 10 minutes at 110°C.
3. Apply cyclotene 3022-46 (BCB) resin on the sample using syringe and 0.2 μm filters. Wait 30 seconds and spin-coat at 1500 rpm and 150 rpm/s for 30 seconds.
4. Immediately transfer the sample into the Blue Oven. Set the N<sub>2</sub> flow to 60 units.
5. Ramp the temperature to 50°C Cover 5 minutes and hold temperature for another 5 minutes.
6. Ramp the temperature to 100°C Cover 15 minutes and hold temperature for another 15 minutes.
7. Ramp the temperature to 150°C Cover 15 minutes and hold temperature for another 15 minutes.
8. Ramp the temperature to 250°C Cover 1 hour and hold temperature for another 1 hour.
9. Wait approximately 12 hours for the chamber to cool down with the chamber door closed.
10. Measure the BCB thickness with Nanometrics.

BCB ash-back:

11. Solvent clean the sample.
12. ICP: Make sure the ash chamber temperature is 50°C.
13. Ash chemistry and gas flow: CF<sub>4</sub>/O<sub>2</sub> = 50/200 sccm; chamber pressure: 40 Pa; plasma power 1000 W.



14. Conditioning (ash chamber empty) run 15 minutes.
15. Etch the sample for 4 minutes. Solvent clean the sample.
16. Measure the BCB thickness again with Nanometrics.
17. SEM: observe the sample at 2 to 5 kV and check if the emitter stack, base post, and collector posts are all revealed and no BCB residues on them.
18. If the posts are not revealed, do another 15 to 60 seconds BCB ash until they are > 50 nm above the BCB surface.

### **A.2.25 Dielectric Contact Via**

Sputtered SiN<sub>x</sub> deposition:

1. Solvent clean the sample.
2. Sputter 4: run 2700 seconds of room-temperature SiN<sub>x</sub> recipe on a 2 inch wafer. Cleave the Si wafer so it and the sample are of the similar sizes.
3. Measure SiN<sub>x</sub> thickness with Ellipsometer. Calculate the deposition rate.
4. Sputter 60 nm of SiN<sub>x</sub> onto the sample.

Lithography:

5. Solvent clean the sample. Dehydration bake for 10 minutes at 110°C.
6. Apply SPR955CM-0.9 photoresist on the sample and spin-coat at 3000 rpm for 30 seconds. Bake at 95°C for 90 seconds.
7. Load the sample into Autostepper in the orientation 180° rotated from that of the EBL.
8. Align and expose the sample for 0.27 second with the contact via mask.
9. Bake at 110°C for 90 seconds.
10. Develop the sample in AZ300MIF for 60 seconds with slight agitation every 15 seconds. 3 minute D.I. rinse with a trickle. Dry the sample with N<sub>2</sub> gun.
11. Verify the pattern and the alignment using an optical microscope with the green filter. Rework if the misalignment is too great.
12. PE-II: O<sub>2</sub> de-scum at 100 W and 300 mTorr for 20 seconds.

Lithography:

12. ICP: Make sure the etch chamber temperature is 50 °C. Run 10 minutes standard O<sub>2</sub> clean.
13. (High power etch) Etch chemistry and gas flow: CF<sub>4</sub>/O<sub>2</sub> = 20/5 sccm; chamber pressure: 1 Pa; ICP/forward bias power 500/100 W.
14. (Low power etch) Etch chemistry and gas flow: CF<sub>4</sub>/O<sub>2</sub> = 20/2 sccm; chamber pressure: 0.3 Pa; ICP/forward bias power 25/18 W.
15. Run high power etch for 5 minutes with the chamber empty for conditioning.
16. Etch the Si piece from sputtering using low power etch for 6 minutes.
17. Measure SiN<sub>x</sub> thickness again with Ellipsometer and determine the etch rate. Calculate the etch time for 60nm × 120%. The thickness of the SiN<sub>x</sub> anchor layer is neglected because it has been removed by BCB ash.
18. Etch the sample with low power etch for the calculated time.
19. 3 minutes ACE rinse and 3 minutes IPA rinse.
20. Strip photoresist in 1165 at 80°C for 1 hour. 3 minutes IPA rinse followed by 3 minutes D.I. rinse with a trickle. Dry the sample with N<sub>2</sub> gun.
21. PE-II: O<sub>2</sub> de-scum at 100 W and 300 mTorr for 30 seconds.
22. SEM: check the sample for any abnormality.

#### **A.2.26 Metal 1 Lithography and Lift-off**

1. Solvent clean the sample. Dehydration bake for 10 minutes at 110°C.
2. Apply nLOF2020 photoresist on the sample and spin-coat at 3500 rpm for 30 seconds. Bake at 110°C for 60 seconds.
3. Load the sample into Autostepper in the orientation 180° rotated from that of the EBL.
4. Align and expose the sample for 0.16 second with the metal 1 mask.
5. Bake at 115°C for 60 seconds.

6. Develop the sample in AZ300MIF for 120 seconds with minor agitation every 30 seconds. 3 minute D.I. rinse with a trickle. Dry the sample with N<sub>2</sub> gun.
7. Verify the pattern and the alignment using an optical microscope with the green filter. Rework if the misalignment is too great.
8. PE-II: O<sub>2</sub> de-scum at 100 W and 300 mTorr for 20 seconds.
9. E-Beam 4: replace crystal monitor. Evaporate 200 Å of Ti at deposition rate < 0.5Å/s, 10 kÅ of Au at deposition rate = 1 ~ 4Å/s, and 200 Å of Ti at deposition rate < 0.5Å/s onto the sample.
10. Strip the photoresist and lift-off in 1165 at 80°C for 1 hour. 3 minutes IPA rinse followed by 3 minutes D.I. rinse with a trickle. Dry the sample with N<sub>2</sub> gun.
11. SEM: inspect the sample and check for any abnormality.